

Wavelength-selective neutron imaging for materials science

vorgelegt von

Master of Engineering

Ala'a Mohammad Al-Falahat

von der Fakultät III – Prozesswissenschaften
der Technischen Universität Berlin
zur Erlangung des akademischen Grades

Doktor der Ingenieurwissenschaften

-Dr. Ing.-

genehmigte Dissertation

angefertigt am Helmholtz-Zentrum Berlin für Materialien und Energie
Institut für Angewandte Materialforschung

Promotionsausschuss:

Vorsitzender: Prof. Dr. Frank Behrendt

Gutachter : Prof. Dr. John Banhart

Gutachter: Prof. Dr. Wolfgang Treimer

Tag der wissenschaftlichen Aussprache: 03.08.2019

Berlin 2019

Abstract

Neutron imaging, specifically radiography and tomography, is nowadays widely used technique for non-destructive investigations of materials and is commonly utilized for various applications in the field of engineering science and technology. The neutron imaging experiments presented in this work were conducted at the neutron imaging facility CONRAD-2 and at the ESS test beamline instrument V20 at the neutron source BER-II.

A virtual model of the instrument is used to analyse the performance of instrumentation, to optimize the existing instrument components and to compare the results of real experiments with Monte-Carlo ray-tracing simulations.

Experimental data of a double-crystal monochromator that is widely used at steady state neutron sources is investigated and compared to neutron ray tracing simulations. The influence of crystal mosaicity on neutron flux and beam size are reported for the utilized setup and the resulting wavelength gradients along one direction. Moreover, a novel neutron radiographic technique for Bragg-edge imaging experiments utilizing the wavelength gradient was developed.

Furthermore, a technique to enhance the wavelength resolution of a monochromatic neutron beam at the CONRAD-2 instrument is applied based on a deconvolution algorithm using a Fourier self-deconvolution method. This method depends only on the narrowing of the spectrum band and can be performed by selecting the optimal value of the full bandwidth at half-maximum (FWHM) parameter, which corresponds to the resolution of the instrument that acquired the spectrum. In order to investigate the potential advantage of the deconvolution technique Bragg-edge transmission spectra of different steel samples were recorded by the time-of-flight (TOF) technique at the ESS test beamline which provides much better resolution (below 1% $\Delta E/E$) than the double-crystal monochromator (approximately 2.5% $\Delta E/E$). This technique is very useful for microstructural analyses based on Bragg-edge spectroscopy.

In order to quantify Bragg-edge spectra of samples under in-situ heat treatment, the transmission spectrum of a martensitic steel was determined by experiments at different temperatures ranging from 21 °C to 800 °C. The evaluation of the spectra proved that the height of the Bragg edge changes with the Debye-Waller factor. The diffracted intensity decreases with increasing

temperatures. Additionally, an incipient phase change reduces the volume fraction of the martensitic phase.

In neutron imaging experiments, backlight scattering or back illumination into the detection system can significantly affect the quantification of attenuation coefficients and can lead to severe errors and image artifacts. Therefore, correction of neutron backlighting is desirable. In this dissertation, the backlighting effects in neutron imaging experiments at the CONRAD-2 instrument were investigated by varying the illuminated detector area and the magnitude of the attenuation. Finally, a backlighting correction procedure is suggested.

Kurzfassung

Neutronen-Bildgebung, insbesondere Radiographie und Tomographie, ist mittlerweile eine fest etablierte Methode für zerstörungsfreie Materialuntersuchungen mit einem großen Spektrum verschiedenster Anwendungen in ingenieurwissenschaftlichen und technologischen Bereichen. Die in dieser Arbeit gezeigten Messungen wurden am Neutronen-Imaging-Instrument CONRAD-2/V7 sowie an der ESS Testbeamline V20 am Forschungsreaktor BER II durchgeführt.

Ein virtuelles Modell der Beamlines wurde erstellt und genutzt um die Leistungsfähigkeit der Instrumentierung zu analysieren, die vorhandenen Komponenten zu optimieren und reale Messergebnisse mit Monte-Carlo Ray-Tracing Simulationen zu vergleichen.

Experimentelle Daten eines Doppelkristall-Monochromators, der üblicherweise an kontinuierlichen Neutronenquellen eingesetzt wird, wurden untersucht und mit entsprechenden Ray-Tracing Simulationen verglichen. Der Einfluss der Kristallmosaizität auf den Neutronenfluss und auf die Strahlgröße im genutzten Setup wird dargelegt und der resultierende Wellenlängengradient wurde bestimmt. Darüber hinaus wurde eine neuartige Methode entwickelt neutronenradiographisch diesen Wellenlängengradienten auszunutzen, um Bragg-Kanten-Experimente durchzuführen.

Auf der anderen Seite wurde mittels eines Entfaltungsalgorithmus im Fourierraum die Wellenlängenauflösung der Messungen mit monochromatischem Neutronenstrahl am CONRAD-2 Instrument erhöht. Diese Auswertemethode basiert auf einer Fitting-Prozedur, die die spektrale Auflösung des Instruments berücksichtigt. Um die möglichen Vorteile dieser Entfaltungstechnik zu untersuchen, wurden Transmissionsspektren von Bragg-Kanten mittels Flugzeitspektroskopie an der ESS-Testbeamline ($1\% \Delta E/E$) sowie mittels Doppelkristall-Monochromator am CONRAD-2 ($2.5\% \Delta E/E$) aufgenommen und verglichen. Diese Technik ist sehr nützlich für Mikrostrukturanalysen, die auf Bragg-Kanten-Spektroskopie basieren.

Um die Spektren der Bragg-Kanten während einer Temperaturbehandlung quantitativ zu studieren wurden Transmissionsspektren von martensitischem Stahl bei Temperaturen zwischen 21 und 800°C aufgenommen. Die Auswertung der Spektren ergab, dass sich die Höhe der Bragg-Kanten entsprechend dem Debye-Waller Faktor ändert. Die gestreute Intensität nimmt mit steigender

Temperatur ab. Zusätzlich reduziert eine einsetzende Phasenumwandlung den Volumenanteil der martensitischen Phase.

In der Neutronen-Bildgebung beeinflussen Hinterleuchtungseffekte im optischen Detektorsystem mitunter ganz erheblich die ermittelten Transmissionswerte, was zu größeren Messfehlern in den errechneten Schwächungskoeffizienten und zu Bildartefakten führen kann. Daher ist eine Korrektur dieses Hinterleuchtens wünschenswert. In dieser Dissertation wurden diese Effekte mittels Experimenten am CONRAD-2 Instrument durch Variation der abgedunkelten Detektorfläche sowie Variation der Stärke der Abdunkelung untersucht, und ein Korrekturprozedur vorgeschlagen.

Contents

1	Introduction.....	1
1.1	<i>Motivation.....</i>	<i>1</i>
2	Neutron instruments.....	6
2.1	<i>CONRAD-2.....</i>	<i>6</i>
2.1.1	The CONRAD-2 neutron guide.....	6
2.1.2	Double-crystal monochromator.....	7
2.1.3	Detector system.....	8
2.1.4	Data analysis.....	9
2.2	<i>ESS testbeamline V20.....</i>	<i>9</i>
2.2.1	The V20 guide system.....	10
2.2.2	The choppers system.....	10
2.2.3	Measurement position.....	13
2.2.4	Detector system.....	13
2.2.5	Data collection and analysis.....	14
3	McStas – A neutron ray-trace simulation of neutron scattering instrument.....	17
3.1	<i>Overview.....</i>	<i>17</i>
3.2	<i>McStas components used for CONRAD-2 and ESS Testbeamline.....</i>	<i>19</i>
3.2.1	Neutron source.....	19
3.2.2	Neutron guide.....	19
3.2.3	Monochromator.....	20
3.2.4	Disk chopper.....	21
3.2.5	Monitors.....	21
3.2.6	Sample component.....	22
4	Effect of Debye-Waller factor on neutron Bragg-edge imaging.....	23
4.1	<i>Theory.....</i>	<i>23</i>
4.1.1	Debye-Waller factor.....	23
4.1.2	Scattering cross sections.....	25
4.2	<i>Experimental details.....</i>	<i>28</i>
4.3	<i>Results and Discussion.....</i>	<i>29</i>
4.4	<i>Conclusions.....</i>	<i>37</i>
5	Energy-selective neutron imaging by exploiting wavelength gradients of double crystal monochromators – simulations and experiments.....	39
5.1	<i>Results and discussion.....</i>	<i>39</i>
5.1.1	Comparison with experimental results.....	42
5.1.2	Wavelength-gradient translation imaging (WGTI).....	45
5.2	<i>Conclusions.....</i>	<i>47</i>
6	Enhancement of the monochromatic beam resolution at the CONRAD-2 instrument based on a deconvolution algorithm.....	48
6.1	<i>Theory.....</i>	<i>48</i>

6.2	<i>Experimental procedure</i>	50
6.3	<i>Fourier-self deconvolution</i>	52
6.4	<i>Conclusions</i>	57
7	Investigation and correction of detector backlighting effects in transmission imaging experiments	58
7.1	<i>Investigation of detector backlighting effects</i>	58
7.1.1	Technical details	58
7.1.2	Variation of the detector coverage:	58
7.1.3	Variation of the penetrated thickness	63
7.1.3.1	Full detector coverage	63
7.1.3.2	Partial detector coverage	63
7.1.4	Summary of investigation of the Backlighting effect	65
7.2	<i>Correction approach of detector backlighting in radiography</i>	66
7.2.1	Backlighting model	66
7.2.2	Determination of backlight factor	67
7.2.3	Modeling of backlighting intensity	68
7.2.4	Correction of backlighting effects	70
7.2.5	Summary and conclusions of the correction of the backlighting effect	72
8	Summary	73
	List of references	75
	Acknowledgements	87

1 Introduction

1.1 Motivation

Neutron and X-ray imaging are common techniques with a wide area of applications in research and technology. Beyond rather universal applications of X-ray radiography, neutron imaging provides high transmission through metallic materials where X-rays are strongly attenuated. At the same time neutrons are very sensitive to many light elements, such as hydrogen or lithium. This makes neutron imaging an ideally suited tool for investigations of hydrogen distributions in metals, water or other media [1-4] in fuel cells [5-9], or lithium and electrolyte distributions in batteries [10, 11]. This is represented in the attenuation cross sections for a selected number of elements in **Figure 1.1** the area of each disk scales with the corresponding attenuation cross section. An example, compared to X-Rays the attenuation cross section of steel is less with a neutron beam and hence, the penetration depth of the neutron beam is larger [12, 13]

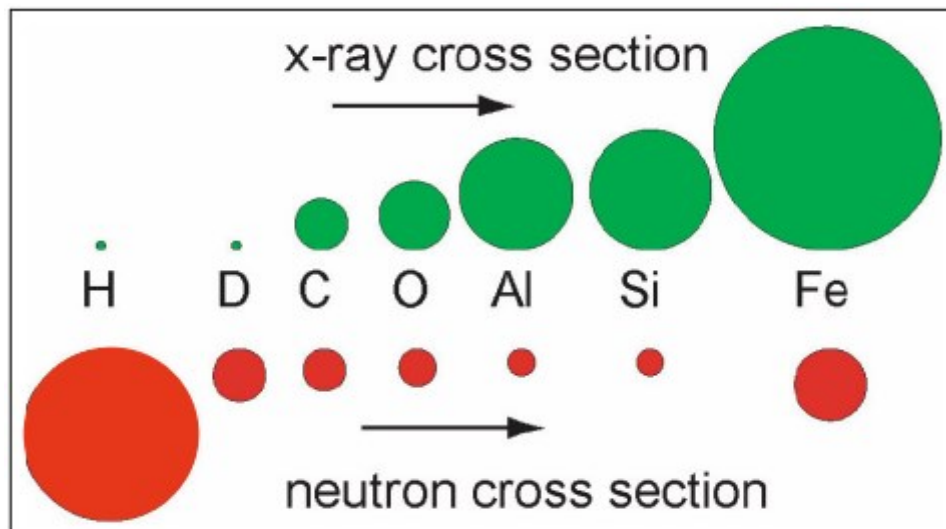


Figure 1.1. X-ray and neutron cross-section of some common elements [14].

The radiographic images are formed due to the interaction probability of the beam with the material that leads to its attenuation. In the ideal case, when a beam (X-rays, neutrons or others) of intensity I_0 passes through a sample with thickness D , it is attenuated along the path. This attenuation μ is described by the Beer-Lambert law to each ray through the sample hitting a detector pixel at coordinate (x, y) :

$$T(x, y) = I(x, y)/I_0(x, y) = \exp^{-\mu(x,y)D(x,y)} \quad (1.1)$$

where $I(x, y)$ and $I_0(x, y)$ are the attenuated and incident intensities, respectively. The transmission image $T(x, y)$ is the ratio of the intensities of two images: the image with the sample $I(x, y)$ and without sample $I_0(x, y)$. The latter is known as the flat field or open beam image. μ and D are the linear attenuation coefficient and the penetrated thickness of the sample, respectively. The deviations from the exponential attenuation law often are not regarded in qualitative radiology, but they could become considerable in quantitative imaging.

There are some typical well-known corrections that should be applied in order to obtain accurate quantitative results from measured radiographs: the dark field correction caused by the dark current I_{dark} of a detector (e.g., a CCD camera) that is subtracted from the radiographic images $I(x, y)$ and $I_0(x, y)$, and the flat field correction requiring the division of the measured flux of a radiograph by the measured open beam intensity (**Figure 1.2**) [15]:

$$\mu D_{\text{corr}} = -\ln\left(\frac{I(x, y) - I(x, y)_{\text{dark}}}{I_0(x, y) - I(x, y)_{\text{dark}}}\right) \quad (1.2)$$

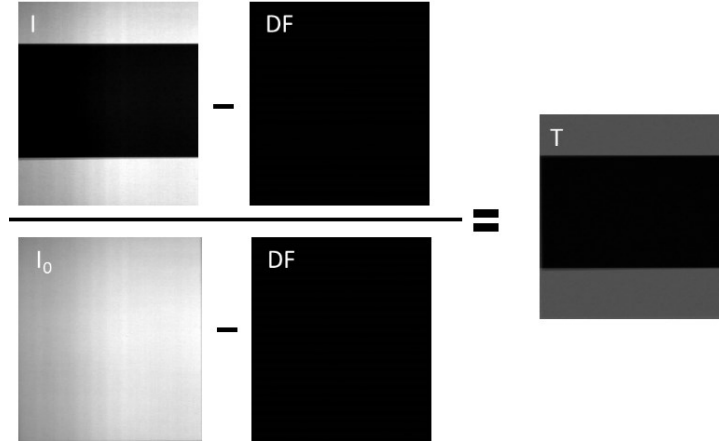


Figure 1.2. Taking the ratio of image with (I) and without sample (I₀) after subtracting the dark field DF yields the transmission image T [15].

Furthermore, beside these corrections there are other sources of errors that should be taken into account, for example the sample scattering component that is also being interpreted as reduced attenuation or as a lower mass density of the material. In addition, the rays missing the sample can be scattered at the surrounding of the sample (e.g., the camera box) or at the shielding and may produce secondary radiation. In case of neutron imaging such problems were previously addressed e.g. by Tremsin *et al.* [16] using collimators, by Hassanein *et al.* [17] using iterative scattering

correction tools, and Peetermans *et al.* [18] using energy selection and by Raventos *et al.* [19] using scintillator-based detection systems .

However, neutron imaging based on the attenuation has a long history and is very popular for the investigation field of the large metallic component. It also allows in some cases changing the material contrast in radiographic images due to wavelength-dependent attenuation properties of materials. Therefore, a wavelength selective neutron imaging technique is routinely applied to polycrystalline materials. This technique exploits variations in the transmitted neutron beam caused by scattered neutrons due to diffraction at the crystal lattice and is especially useful to investigate temperature-driven effects, such as phase transformations in metallic materials.

The wavelength-dependent neutron attenuation coefficient exhibits discontinuities whenever the conditions for Bragg scattering can no longer be fulfilled upon increasing wavelengths – the so-called Bragg edges [20]. The positions of the Bragg cut-offs are related to the corresponding d_{hkl} spacings. Shifts of the Bragg edges [21, 22] can be used to detect the presence of residual stresses in metallic samples affecting the d spacing. The Bragg edge height can be connected to the presence of texture [23, 24], while the Bragg edge shape relies on grain size [25].

Recently, new neutron imaging methods have been developed that connect real-space with reciprocal-space approaches [26-29] and allow for investigations of microstructures in bulk materials [30, 31] on length scales down to 20 μm by employing high-resolution detector systems [8, 32-35]. The combination of such high spatial resolution with the new imaging methods enables one to directly visualise magnetic structures, stress and strain fields, textures, heterogeneous microstructures, etc. [2, 23, 36-48] A step towards nanometer-sensitivity can be made with the help of imaging methods that connect the real with the reciprocal space such as grating interferometry [49-53] and Bragg edge mapping [13, 24, 26, 54-56] in propagation geometry. In this case, one can detect structures down to the nanometer size range.

However, the different probability types of interaction absorption and scattering, both coherent and incoherent, elastic and inelastic are characterized by neutron cross sections, which depend on material properties and on neutron energy. Neutron cross sections (conveniently expressed in terms of barns, 1 barn = 10^{-28} m^2) and represent the cross sectional area of a chemical element towards an incoming neutron to perform scattering or absorption. However, for quantitative data analysis, it is necessary to take into consideration that the diffracted intensity depends on the temperature

of the investigated material. The Debye-Waller factor describes the decrease of the elastically diffracted intensity caused by thermal vibrations of atoms at finite temperatures.

Simulations were performed with the application of a Monte Carlo based on program code 'McStas'[26, 57]. It is used for the design and optimization of the instruments as well as to understand its behavior and the principle of the devices such as double crystal monochromator, choppers and detectors.

With the work presented here, a series of wavelength selective in-situ neutron imaging experiments are performed, in order to

1. investigate the influence of thermal effects, described by the Debye-Waller factor on Bragg-edge height by investigating the corresponding Bragg-edge at a different temperature and the comparison to theoretical calculations based on the nxsPlotter software [58] has been performed. The nxsPlotter program was used to calculate total cross sections of crystalline compositions as a function of neutron wavelength and compare them with experimental results. The changes of the transmitted intensity are analyzed in order to investigate the effect of the thermal expansion and thermal vibration according to the Debye Waller factor on the neutron cross section and attenuation coefficient of the selected steel.
2. understand the behaviour and the principle of a double-crystal monochromator device. The basic principles and properties of a double-crystal monochromator used for the monochromatisation of the neutron beam and the obtained wavelength gradient are studied. In addition, a new neutron radiography technique for Bragg edge mapping in imaging experiments utilizing a neutron wavelength gradient at the sample position was developed and Monte Carlo simulations based on 'McStas' have been performed. In addition, in order to improve the wavelength resolution of the measurements, a Fourier self-deconvolution technique is applied on the transmission neutron spectrum of the selected steel sample.

In addition, the quantification of attenuation values are investigated and corrected to obtain accurate quantitative results from measured radiographic images. There are many effects that hinder a sufficient quantification accuracy e.g. the quality of the detector and scintillator systems,

scattering coming from the sample or beam hardening. This study concerns the basic research and development on quantitative neutron radiography using a first order approach in order to systematically correct the distortion of the quantitative information about absorption data. Therefore, we investigated an effect that is mostly neglected in quantitative imaging, the so-called backlighting effect caused by scattered light in the detection system itself. We have varied two parameters to study the backlighting effect: the detector coverage and the penetration length through a sample.

2 Neutron instruments

This chapter describes the basic principle of the setups for neutron instruments utilized within this work. The neutron wavelength selective experiments presented herein are conducted at the BERII research reactor of Helmholtz-Zentrum Berlin (HZB) in Germany, by using;

a) The cold neutron radiography instrument (CONRAD-2) V7 applied with the double-crystal monochromator. [59]

b) The ESS testbeamline V20 using time-of-flight (TOF) spectroscopy by a specifically designed chopper system.[60]

The basic principle of these instruments is given in the following:

2.1 CONRAD-2

Figure 2.1 shows the instrument of CONRAD-2 (COLD Neutron RADiography) used for our investigations e.g. [12, 16, 61, 62].

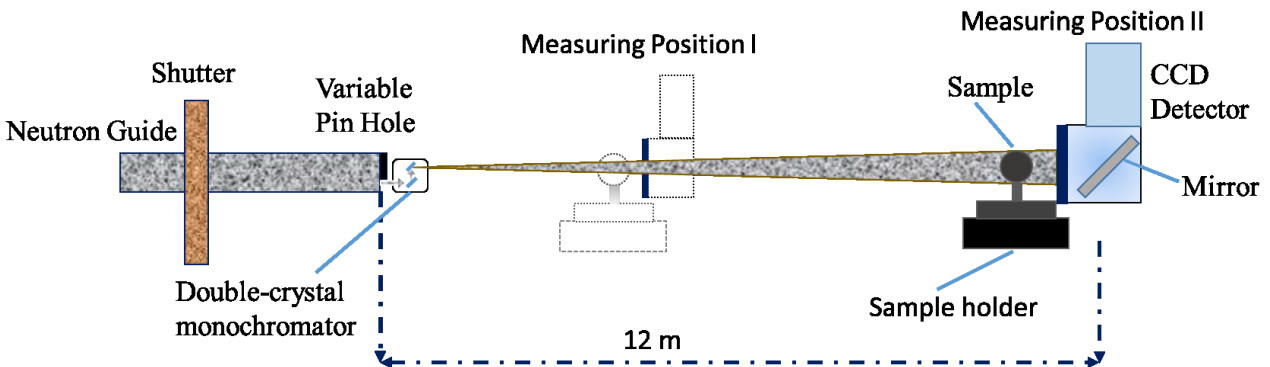


Figure 2.1. Layout of the neutron-imaging instrument CONRAD-2.

2.1.1 The CONRAD-2 neutron guide

Cold neutrons are transported from the cold neutron source at the 10 MW research reactor BER II to the experiment through neutron guides, which contains a curved guide section of 15 m length and a bending radius R of 750 m, which is sufficient to keep fast neutrons and γ photons away from the experimental end station. The curved guide has different wall coatings ($m = 2.5$ for the inner wall and $m = 3.0$ for the outer, top and bottom walls) that provide the best result in terms of

transport beam intensity and homogeneity. In front of and behind the curved guide are straight guide sections ($m=2$). The role of the final straight section is to homogenize the beam intensity over the guides' cross section. All guide sections have a constant cross section of height \times width = 12 \times 3 cm. The neutron beam at CONRAD-2 is polychromatic with wavelengths mainly between 2 and 6 Å and a maximum intensity at about 3.0 Å.

At the end of the guide, a double-crystal monochromator was installed in combination with a pinhole set as shown in **Figure 2.1**. This configuration allows for remotely switching between monochromatic and polychromatic neutron beams.

A flight path of $L = 12$ m is available downstream of the final straight guide section. This distance is necessary in order to make full use of the pinhole configuration, where a certain L/D ratio can be realized by using apertures with different diameter D at the beginning of the flight path. For apertures with typical diameters of 1 cm to 3 cm, the calculated L/D ratios are between 1200 and 400, respectively.

2.1.2 Double-crystal monochromator

The double-crystal monochromator at the CONRAD-2 instrument consists of two parallel plates, with dimensions of 6 \times 5 cm² (length \times width), of highly oriented pyrolytic graphite HOPG (002) single crystals. These are aligned one above the other with a fixed distance $h = 7.4$ cm [26]. The crystal lattice spacing is given by $d_{002}=3.348$ Å. As shown in **Figure 2.2** the orientation and positioning of the monochromator crystal plates is performed by selecting a desired neutron wavelength λ as an input parameter from which the Bragg angle θ is calculated using Bragg's law:

$$\theta = \arcsin\left(\frac{\lambda}{2d_{002}}\right), \quad (2.1)$$

The monochromator plates are parallel and neutrons of corresponding wavelength λ will undergo double reflection. The advantage of this arrangement is that the direction of the extracted monochromatic beam is parallel to the initial neutron beam. For setting a defined wavelength, the two plates are rotated to the corresponding angle θ and the bottom plate is moved horizontally along the neutron beam direction to a position Z determined by

$$Z = h \tan(90^\circ - 2\theta), \quad (2.2)$$

where h refers to the vertical distance between the plates and Z to the linear translation on the Z -axis of the lower plate respectively, **Figure 2.2**

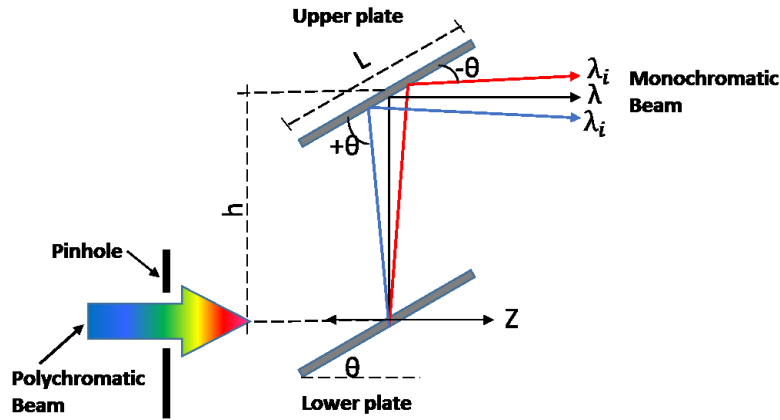


Figure 2.2. Schematic drawing of the double-crystal monochromator setup at CONRAD-2 as well as the wavelength distribution behind it.

The HOPG crystals have a certain mosaicity (degree of crystallite misalignment), which allows for selecting a broader wavelength band around the corresponding wavelength fulfilling the Bragg reflection condition for the set scattering angle θ . By ray-tracing the neutron beam through the double-crystal device, one can expect a spectral divergence depending on the direction of the neutrons flight paths through double reflection as shown in **Figure 2.2**. The mosaicity of the crystallites will allow smaller scattering angles for the longer wavelengths and larger angles for the shorter wavelengths. Considering the configuration shown in **Figure 2.2** the wavelength gradient is expected to be along a vertical line, with longer wavelengths on the bottom and shorter wavelengths on the top.

2.1.3 Detector system

The neutron detector used at HZB consisted of a ${}^6\text{LiF}$ scintillator screen of 200 μm thickness, which converts the transmitted neutrons into visible light and an optical CCD camera with an objective lens [7, 63]. The converted light is subsequently reflected by a mirror into an objective camera lens. The camera used contains a CCD chip with 2048×2048 pixels each with a size of $13.5 \times 13.5 \mu\text{m}^2$ with a 16-bit AD-converter. More technical information about the setup can be found elsewhere [59].

2.1.4 Data analysis

After the detector captures the intensity of the transmitted neutron beam, the evaluation of radiographic image experiments is conducted with image processing. Basically, three different types of images are required to perform the data normalization to obtain spatially resolved transmission values.

- Image of the sample: Provides the sample properties such as material structure, its dimensions and beam attenuation.
- Flat field image (FF): Refers to the beam profile, i.e. an image without the sample including neutron flux distribution, camera and scintillator defects and sensitivity.
- Dark field image (DF): Gives an image without the beam referring to the properties of the CCD-array since the camera is not only sensitive to photons but also to thermal energy. For these images, the beam has to be fully blocked with the beam shutter.

In the first step, the dark field image is subtracted from the original sample image and the flat field image in order to eliminate the signal offset resulting from thermal influences. Then the sample image is divided by the FF image. in order to obtain transmission values Within this thesis, The analysis of the images was accomplished by using the program ImageJ [64].

2.2 ESS testbeamline V20

The ESS testbeamline (TBL) V20 as shown in **Figure 2.3** is a multi-purpose time-of-flight (TOF) neutron instrument [65, 66]. In its wavelength-resolving neutron imaging setup [67-69] a wavelength spectrum from 1.8 Å to 10 Å is scanned, where the wavelength is determined by the time t it takes for a neutron to travel a given known distance L to reach the detector. This can be achieved either through generating neutron pulses by chopping a continuous neutron spectrum from a reactor source or through generating the neutrons in pulses at an accelerator source which is called neutron spallation sources, such as the European Spallation Source (ESS). V20 is built at the BER II research reactor at the Helmholtz-Zentrum Berlin and designed to mimic the pulse of the ESS spallation source.

The ESS testbeamline V20 is a time-of-flight beamline, where different neutron pulses can be created using a specific chopper cascade resulting in a time-of-flight or wavelength spectrum.

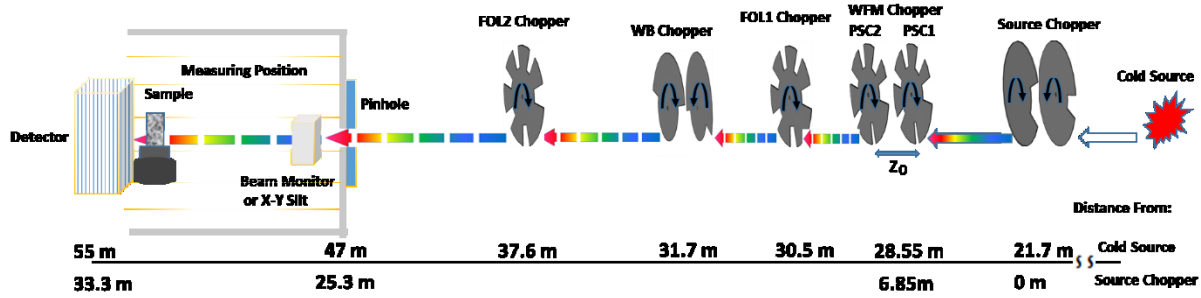


Figure 2.3. Layout of the test beamline (TBL) with locations of all choppers.

2.2.1 The V20 guide system

Neutrons are transported from the continuous cold neutron source to the measuring position through neutron guides which contain a curved guide section (5 m of radius $R_1=1500$ m and 30.45 m of radius $R_2=2300$ m) to avoid fast neutrons and γ photons from the cold source of the reactor to reach the experiment. The final 5 m of the guide being straight, ending at 46.17 m from the cold source [65]. The supermirror guide has wall coatings with an m-value of $m = 3.0$ that provide excellent results in terms of transport beam intensity and homogeneity. More information about the parameters and geometry of the guides can be found in section 4.2.2 (Table 3-1). In order to install eight choppers the guide system provides several gaps: Gaps of 15 cm, 10 cm, 25 cm and 10 cm at distances of 21.7 m, 30.4 m, 31.5 m and 37.6 m, respectively, from cold source as shown in Figure 2.3. An additional relatively large gap of 0.6 m provides space for the wave frame multiplication (WFM) pulse shaping choppers (PSC) at 28.3 m to 28.9 m. All guide sections have a constant cross section of height \times width = 6 \times 12.5 cm.

2.2.2 The choppers system

The TBL V20 has been intended to emulate the neutron long pulse time structure of the European Spallation Source (ESS) by utilizing a complex chopper framework that gives a particular time structure of the ESS. While a continuous spectrum is coming from the reactor through the neutron guide containing various neutron energies, the first chopping of the continuous neutron beam happens at 21.7 m where a counter rotating double disc source chopper is installed as shown in Figure 2.3 and hence the ESS source pulse is mimicked. Further, downstream, the double disc wavelength band chopper is installed at 31.7 m that warrants separating pulses and confining the wavelength bandwidth.

Two chopper modes have been used: a) the ESS long pulse mode and b) the wavelength frame multiplication (WFM) mode.

a) ESS Long Pulse

In this mode the source pulse and the wavelength band double disc choppers are operated and the resulting neutron velocity selection is depicted in a distance-versus-time plot in **Figure 2.4**, produced by the McStas simulation package [57]. The relatively low wavelength resolution is depending on the wavelength range where the slower neutrons are separated more clearly than the faster neutrons; typical values for the wavelength resolution are 4.2% at 8 Å to 16.6% at 2 Å at a distance of 55 m from the cold source [70].

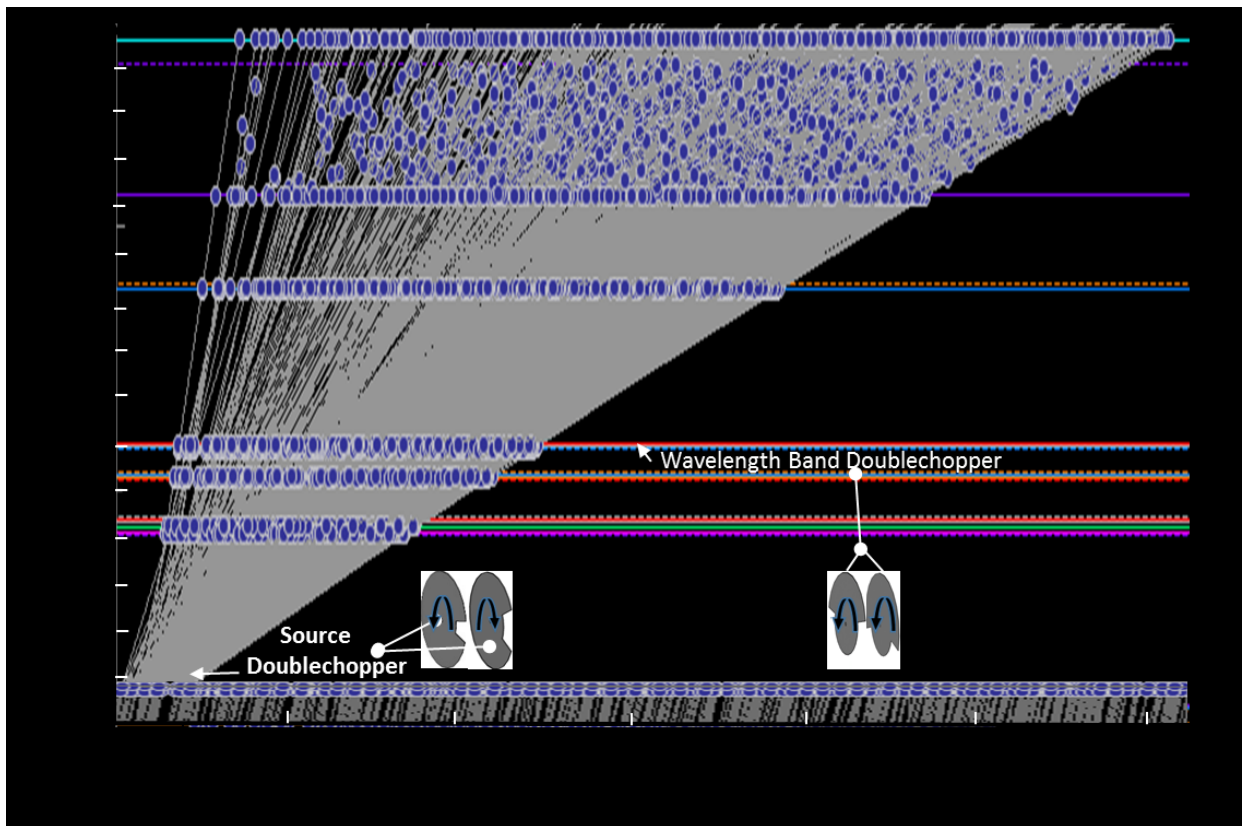


Figure 2.4. Shows the Time-of-flight diagram in case of a long pulse mode illustrating the disc profile of the choppers included main elements of the TBL instrument simulated with McStas.

b) Wavelength Frame Multiplication (WFM)

Since many scattering and imaging methods profit from better wavelength resolution, one solution is additional pulse shaping. Therefore, for better and tuneable wavelength resolution, the wavelength frame multiplication (WFM) chopper system was installed at V20 that provides six sub-pulses from each source pulse as shown in **Figure 2.5**.

The distance z_0 between WFM chopper 1 and 2 can be changed between 140 mm and 427 mm by moving them simultaneously along the beam axis, which provides maximum and minimum wavelength resolution at $z_0 = 140$ mm and $z_0 = 427$ mm respectively [66]. Then the neutrons hit on frame overlap chopper 1 (FOL1) in order to avoid overlap between the wavelength frames in time-of-flight.

In addition, three slits (5×10 cm² between the WFM choppers that is adjustable, 5×10 cm² after the FOL chopper 1 and 2×10 cm² after the FOL chopper 2) are placed in the guide system to reduce contaminant neutron trajectories [65].

Finally, at this mode, the constant high wavelength resolution can be achieved ranging between 0.63% (WFM high-resolution) to 3% (WFM low-resolution) depending on the detector position, i.e. the neutron flight path, and the distance between the WFM choppers z_0 .

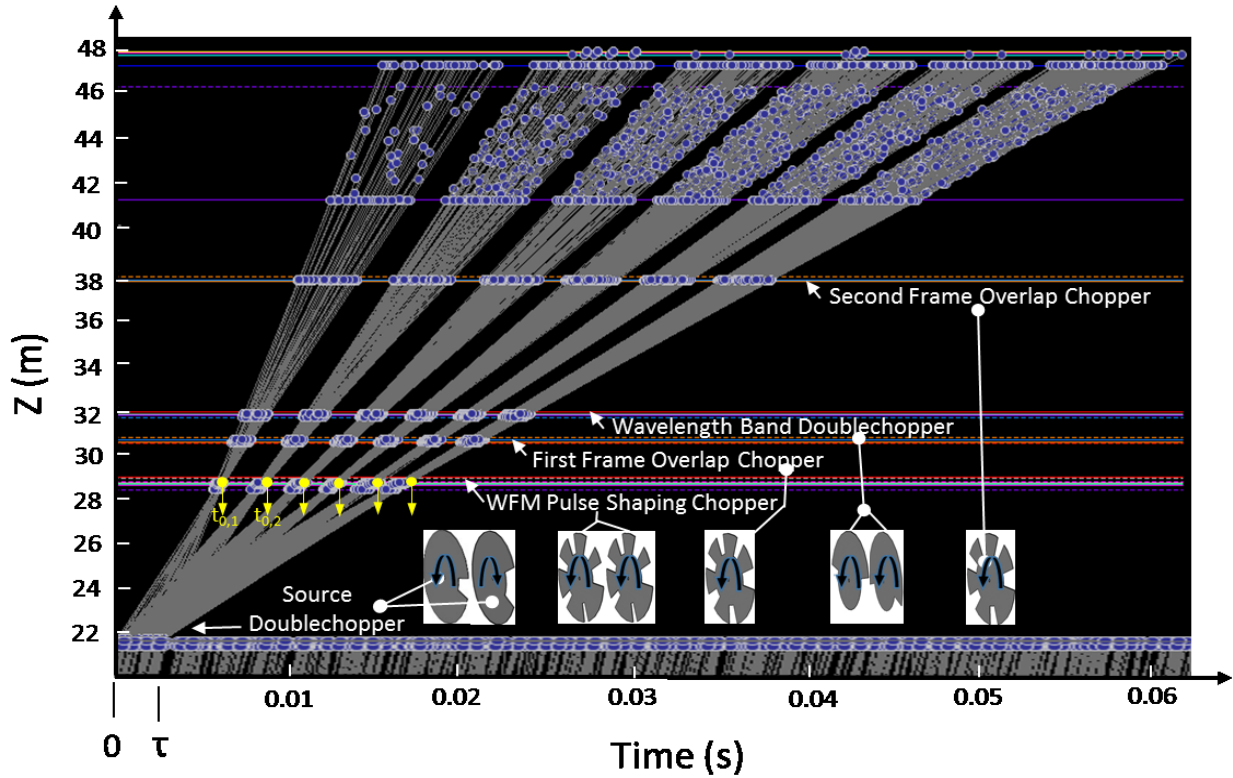


Figure 2.5. Shows the time-of-flight diagram when WFM mode is activated, the distance of all eight working disc choppers included main elements of the TBL are also displayed. Shown is a simulation by McStas. Note that the yellow arrows represent the reference time t_0 for each of the six frames.

2.2.3 Measurement position

At the end of neutron guide, the beam should pass a slit as well as a detector. A beam monitor, with a detection efficiency of 10^{-5} to 10^{-3} at 1.8 \AA is placed behind the end of the neutron guide. The measuring position is within 6 m length from 47.1 to 53.1 m from the cold source while the length could even be increased up to 60 m. The beam hits the sample which is fixed to a specific holder where it is exposed to the neutron beam.

Part of the beam is diffracted and the transmitted part is detected by a detector that is directly behind the sample, In that way, the detector records the transmitted signal.

2.2.4 Detector system

For the work presented in this dissertation, neutron-sensitive microchannel plates (MCPs) detector has been utilized to measure wavelength depended neutron transmission values in time-of-flight mode at the ESS testbeamline instrument. This detector consists of a stack of MCP's and Timepix

chips, where incoming neutrons are converted into an electron signal, which is amplified by two standard microchannel plates installed in direct contact with the front one. The MCP glass structure is doped with ^{10}B to enhance the neutron interaction within the MCP, the detector efficiency is determined by the efficiency of neutron conversion in the front plate and is measured to be around 70% for a cold neutron beam. The active area of the present detector is determined by the size of the Timepix chip, which has a diameter of 40 mm. A More technical information about the instrumentation can be found in this reference [71]

2.2.5 Data collection and analysis

In order to record the neutron intensity, the detector is placed in the appropriate position in the neutron beam the sample is installed directly in front of the detector where it is visually aligned using an alignment laser. By varying the chopper settings and the detector position, the several instrument configurations with different wavelength resolutions are used for investigations.

However, to achieve sufficient signal statistics, an appropriate exposure time is selected for a given spatial resolution.

To obtain the transmission profile, the sample spectrum is normalized by the open beam spectrum measured without sample, therefore, an open beam measurement is recorded for the normalization and the detector settings have to be the same for the sample and open beam experiment. In addition, the open beam collection time and the sample data should be scaled to the same of exposure time.

The incident beam spectrum is shown in **Figure 2.6** and one can observe six distinct neutron pulses: These correspond to the individual wavelength frames. In the region between these frames, the instrumentation concept of WFM yields neutrons that are well separated in time on the detector, but actually have an overlap in wavelength. After a data reduction procedure, commonly referred to as 'stitching', a continuous time-of-flight and hence wavelength band is covered. Therefore, a python-based interface for processing and stitching the TOF spectrum was developed within the MANTID [72] software framework. This relies on the fact that every chopper opening (in this case 6) represents a separate 'source' with its own t_0 . i.e. every individual pulse that form from the two WFM choppers of the six frames in total at TBL has its own time as shown in **Figure 2.5**

The well visible drops around 23 ms, 33 ms, 42 ms, 48 ms and 55 ms are clearly observed in the raw data occurring in the wavelength frame overlap regions. These discontinuities in the spectrum

occur on the measured data due to the gaps between the neighboring frames on the frame overlap regions when the WFM mode is activated as described in section (3.2.2b).

Figure 2.6b shows in contrast to **Figure 2.6a** the time of flight of neighboring frames overlap after the time correction according to the opening times of the WFM chopper windows, as a result, the intensities in the overlap regions are added together and now the shaping chopper pulses are corrected and produced a continuous TOF spectrum as seen in **Figure 2.6c**.

The same corrected procedure, a) through c), is also applied for the sample spectrum, e.g. bcc steel sample as shown in **Figure 2.6d** and to obtain the transmission spectrum, the bcc sample spectrum is normalized by the open beam spectrum measured without sample the result is shown in **Figure 2.6e** for high-resolution setting. It can be seen that the sharp intensity peaks, occurring in the frame overlap regions of the spectra, vanish in the normalization and are hence not present anymore in the resulting transmission spectrum.

On the other hand, the neutron wavelength is calculated by the time-of-flight that is measured from the source to the detector with the distance between the choppers and detectors L_{Det} . The conversion formula is [70].

$$\lambda = \frac{h t_{\text{TOF}}}{m L_{\text{Det}}} \quad (2.3)$$

Where m is the mass of neutron and h is Plank constant.

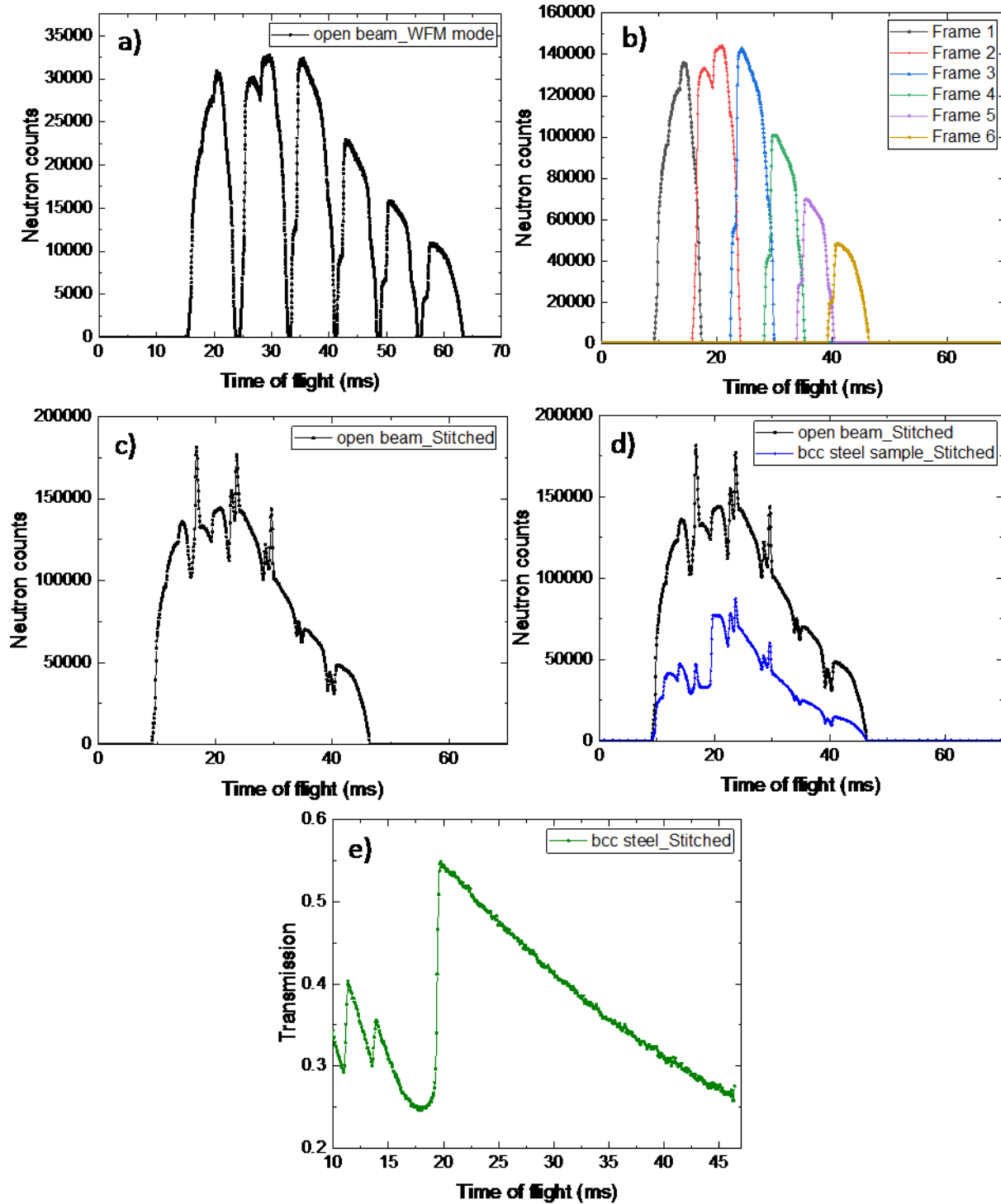


Figure 2.6. Conversion of the TBL recorded data (on WFM intensity spectrum mode) into a continuous TOF spectrum a) the wavelength frames are separated in TOF at the detector position b) the stitching procedure for each frame using MANTID software are performed according to the opening times of the WFM chopper windows. c) The continuous spectrum is achieved d) the same procedure is performed when placing a bcc steel sample in front of the detector e) The transmission spectrum by normalization (divided the sample spectrum by the open beam spectrum) of the stitched data with the characteristic Bragg edges.

3 McStas – A neutron ray-trace simulation of neutron scattering instrument.

3.1 Overview

To understand the physical effect affecting the neutron spectrum and to determine their consequences quantitatively. A virtual model of the instrument has been subject to Monte-Carlo ray-tracing simulations [73] of the experiments. This has been implemented in a software package in McStas [74], which is an effective tool for simulating neutron scattering instruments. In McStas one can compute all aspects of the instrument's performance, enhance the existing instrument components, and compare the results with real experiments. Furthermore, it is useful to design new instruments and create a virtual model of the experiments, for training, experimental planning or data analysis.

To demonstrate the instrument and perform a virtual experiment, both instruments, CONRAD-2 and ESS testbeamline (V20) as displayed in **Figure 3.1** and **Figure 3.2** respectively, which were built up. Full virtual experiments were performed on various samples with different characteristics.

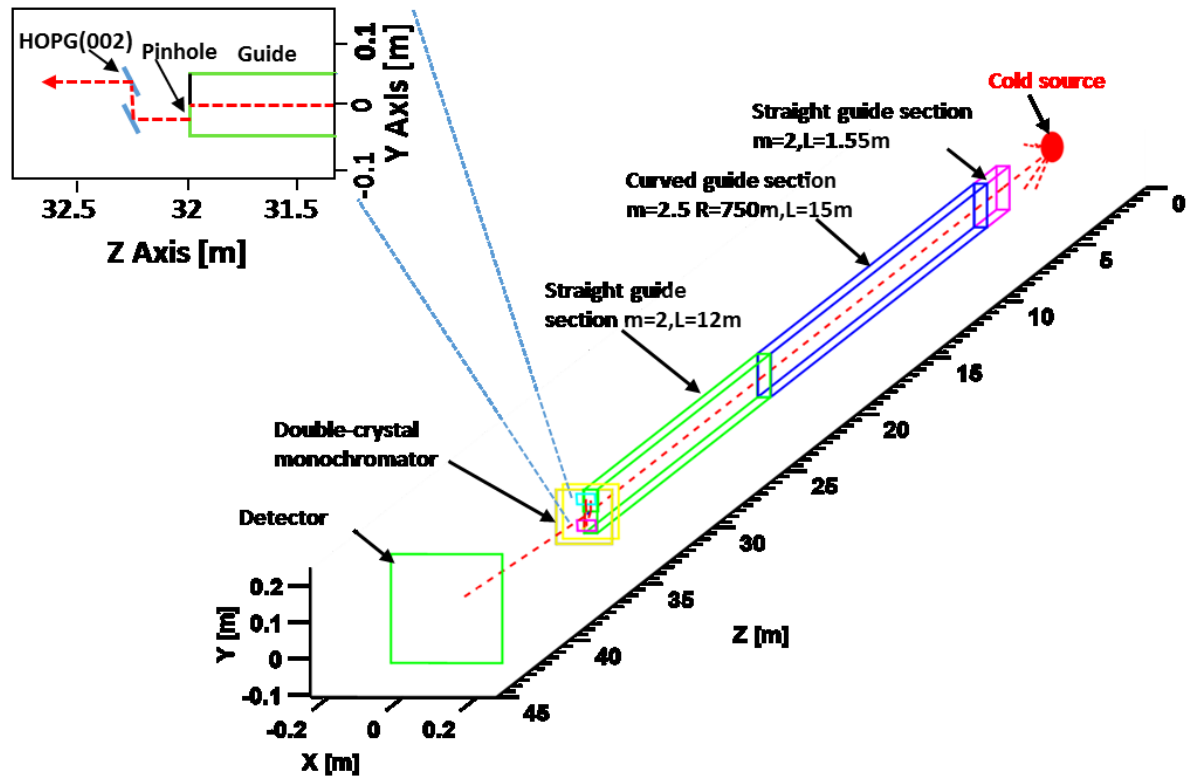


Figure 3.1. 3D view of the neutron beam path to the imaging instrument CONRAD-2.

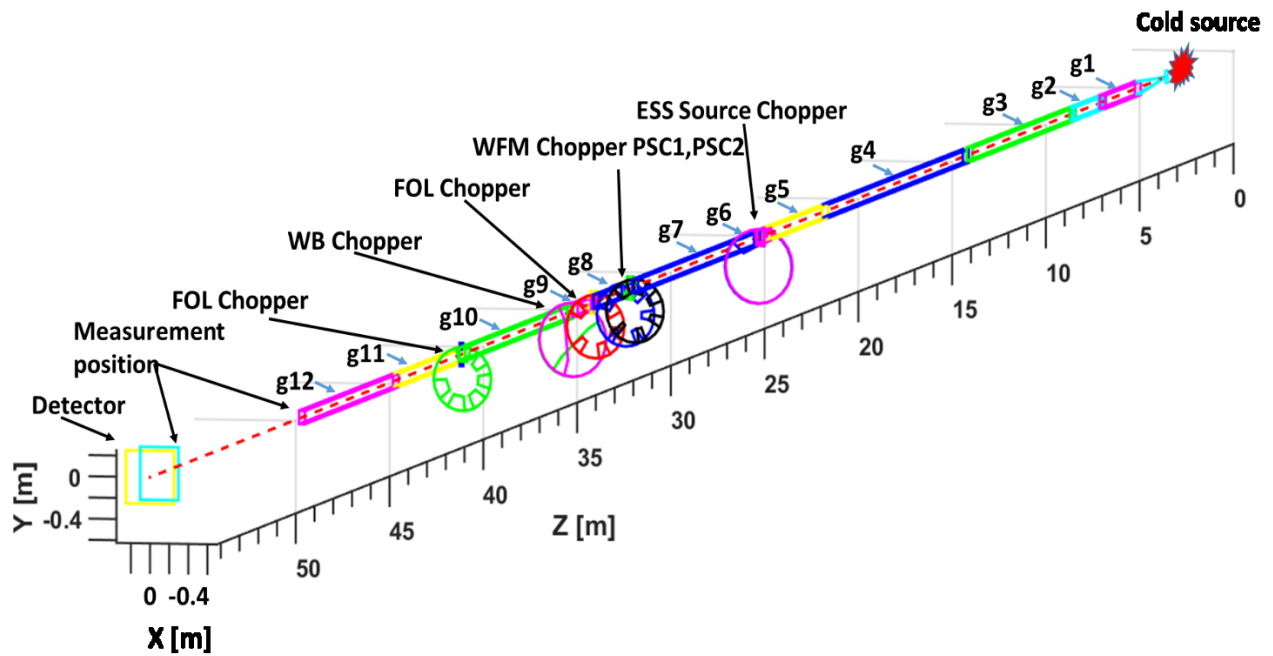


Figure 3.2. 3D view of the neutron beam path to the imaging instrument of ESS testbeamline, gx denote the modular neutron guide, see **Table 3-1** for details of the guide geometry and parameters.

3.2 McStas components used for CONRAD-2 and ESS Testbeamline

3.2.1 Neutron source

In order to simulate a neutron beam incident on the sample, the spectrum was simulated using a Source_Maxwell_3 component to parameterize a continuous neutron source with a Maxwell distribution with temperatures of 45 K and 137.2 K as shown in **Figure 3.3**. The wavelength range between 1 Å and 10Å is selected and the source intensity of 1.4×10^{12} counts are chosen and the initial neutron ray direction is centered within a rectangular entry of (width, height) parallel to the x-y plane.

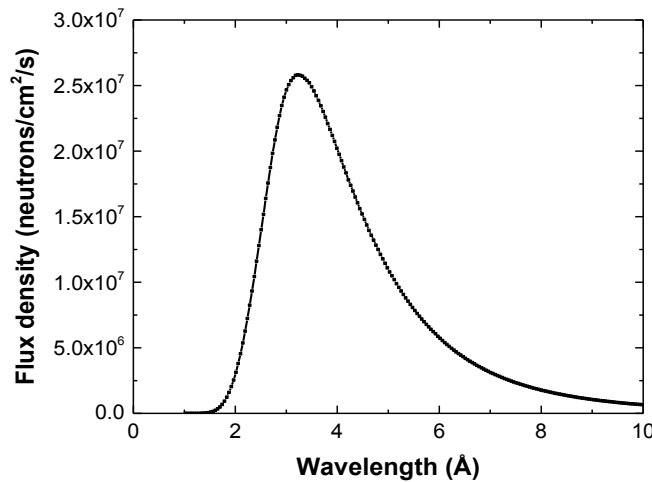


Figure 3.3. The Maxwell spectrum at the exit guide of CONRAD-2 instrument.

3.2.2 Neutron guide

A modular neutron guide (straight or bender) components are selected containing of four flat mirrors that have a different wall coating ($m = 2.5$ for the inner wall and $m = 3.0$ for the outer, top and bottom walls) to avoid fast neutrons and γ photons from the cold source of the reactor to reach the experiment and then give the best outcome as far as transported beam intensity. The straight guide is centered on the z-axis with rectangular entry and exit parallel to the x-y plane. Besides, the bender component is a curved neutron guide that bends to the negative x-axis at a different bending radius through the neutron beam line. The dimension of the entrance guide has the same geometry with an exit in (x, y) plane and are set at $z = 0$ and $z = L$ at the neutron inlet and exit guide respectively, where L is the guide length. This simulation does not take into account the effects of the gravitation on the neutron beam.

The guide details of the CONRAD-2 instrument are clearly shown in **Figure 3.1**. In addition, **Table 3-1** shows the details of the testbeamline V20 instruments guides

Table 3-1. The geometry of the guide sections that are used in testbeamline , the m-value of the material is 3 for all the guide sections.

Guide number	Dimension (w x h) cm	Length (m)	Guide type	Bending radius (m)
g1	6 x 12.5	1.87	Straight	0
g2	6 x 12.5	1.53	Channeled	0
g3	6 x 12.5	5.50	Bender	1500
g4	6 x 12.5	7.50	Bender	2300
g5	6 x 12.5	3.00	Bender	2300
g6	6 x 12.5	0.45	Bender	2300
g7	6 x 12.5	6.50	Bender	2300
g8	6 x 12.5	1.5	Bender	2300
g9	6 x 12.5	1	Bender	2300
g10	6 x 12.5	5.75	Bender	2300
g11	6 x 12.5	3.5	Bender	2300
g12	6 x 12.5	5	Straight	0

3.2.3 Monochromator

A double-crystal monochromator is used at the CONRAD-2 instrument, which is simulated using the Monochromator_flat component, this component describes an infinitely thin single crystal with a single scattering vector, $Q_0 = 2\pi/d_m$ perpendicular to the surface. A typical use for this component is to simulate a simple monochromator or analyzer.

The physical model used in monochromatic_flat component is a rectangular piece of material composed of many small micro-crystals. The orientation of the microcrystals slightly differs from the nominal crystal orientation. Therefore, the likelihood of a specific micro-crystal orientation is symmetrical to a Gaussian model in the angle between the specific and the nominal orientation. The full width half maximum of the Gaussian is specified by the mosaic spread, of the crystal. In this component, and in the real experiment, the mosaicity given is that of the reflected signal [74]. More details about the monochromator geometry parameters are given in chapter 3.

3.2.4 Disk chopper

We implemented this component at the testbeamline instrument V20 to chop a continuous neutron beam into short pulses and control the pulse shape in time. This device consists of a thin disk of radius R having a frequency of rotation (the slower chopper at TBL runs at 14 Hz) with the rotating axis parallel to the neutron beam that consists of neutron absorbing materials. The disk can have a slit of a chosen height h and angular width θ_0 as shown in **Figure 3.4**. In addition, the direction of rotation can be adjusted in order to simulate counter-rotating chopper.

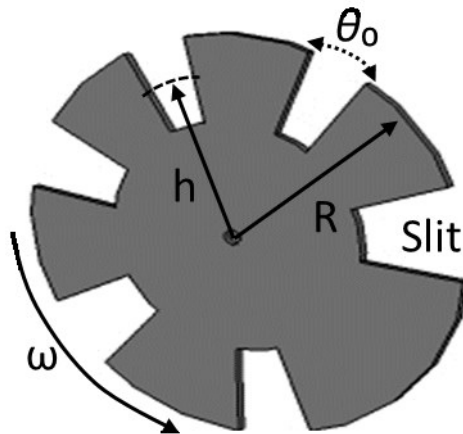


Figure 3.4. Sketch of a disc chopper with geometry parameter.

3.2.5 Monitors

- PSD Monitor: the PSD Monitor is a position-sensitive monitor that detects the incident neutron beam in the (x, y) plane which is divided into pixel columns and rows (n_y, n_x) . It also shows the error connected with the total integrated intensity across the surface of the PSD together with it.
- LambdaYPSD or LambdaXPSD monitor is used to count neutrons and store their wavelength and their lateral positions (Y-position and X-position) at the detector area. The monitor geometry is simplified to a plane area where the neutron position parameters (x, y) and the wavelength will be recorded [75].
- Wavelength monitor and L-monitor: This monitor is rectangular monitors that measure the wavelength of arriving neutrons
- TOF monitor: the time of flight (TOF) monitor is again rectangular monitor that counts a neutron intensity as a function of time of flight.

For more technical details of these McStas components can be found in the manual of McStas components [76]

3.2.6 Sample component

The `nxs_sample` component is the implementation of the `nxs` program library into a McStas component [58] which is used in the presented simulation. Geometry can be a cylinder or a box defined by radius or width, height, and thickness, respectively. The `nxs_sample` component treats the neutron scattering and neutron transmission of the materials. Therefore, this component is useful for imaging and diffraction instruments at the same time.

The simulation has been built for different material definitions and compositions, e.g. Al, Cu, Fe and AISI steel. This component offers the user to choose between a cylindrical, rectangular and three-dimensional geometry sample, from a given instrument file.

4 Effect of Debye-Waller factor on neutron Bragg-edge imaging

In this chapter, we investigate the influence of thermal effects, described by the Debye-Waller factor on the Bragg-edge height by investigating the corresponding Bragg-edge at different temperatures and the comparison to theoretical calculations based on the nxsPlotter library. In this work, neutron transmission spectra are recorded at the CONRAD-2 instrument (equipped with a double crystal monochromator), while heating a super martensitic stainless steel (SMSS) sample inside a furnace. The intensity reduction due to the thermal movement of the atoms on the sample has been determined from analysis of the attenuation coefficients. Subsequently, it is compared to theoretical calculations of the neutron cross sections that are influenced by the temperature. This study shows that the effects can be evaluated from the transmission spectra and it can serve as a basis for corrections during in-situ studies and/or to exploit it for quantitative measurements.

Note: The following parts have been submitted to the “Journal of Applied Crystallography”, Authors: Ala’a M. Al-Falahat, Nikolay Kardjilov, Robin Woracek, Mirko Boin, Henning Markötter, Luise Theil Kuhn, Malgorzata Makowsk, Markus Strobl, Beate Pfretzschner, John Banhart and Ingo Manke.

4.1 Theory

4.1.1 Debye-Waller factor

The Debye temperature θ_D of a bulk solid state is a measure of the rigidity of the bonds inside the crystal where the movement of one atom about its site makes the neighboring atoms to react to this motion and the outcome is that many atoms oscillate as one, and this collective movement spreads throughout the crystal (taken from [77]). Each type of lattice has its own attribute mode or frequencies of oscillation called regular mode, and therefore the overall collective oscillation movement of the lattice is a combination of many regular modes (taken from [78]).

The Debye temperature considering the binding force between atoms can be utilized to signify the properties of the many materials, which include thermal vibration of atoms or phase transition (taken from [79]) and has received a great deal of attention. The Debye temperature of a crystal is $\theta_D = h\nu_D/k_B$, where ν_D is the characteristic Debye frequency, k_B Boltzmann's and h Planck's constant [80].

The Debye-Waller factor (isotropic displacement factor) B_{iso} is connected to the Debye temperature through the following equation (compare e.g. Ref.[81]):

$$B_{\text{iso}} = \frac{3h^2 \varphi_1(x)}{M k_B \theta_D} \quad (4.14)$$

where M is the mass of the scattering nucleus, $\varphi_1(x)$ is the Debye integral function with its argument $x = T / \theta_D$ and T the sample temperature:

$$\varphi_1(x) = \int_{-1}^1 \frac{\varepsilon d\varepsilon}{e^{(\varepsilon/x)} - 1} \quad (4.2)$$

The value of the Debye temperature θ_D can be determined by various experimental methods such as specific heat, elastic constant and diffraction measurements [82, 83]. For this study, the elastic constant method is used to calculate the Debye temperature θ_D at which nearly all modes of vibrations in a solid are excited. It is given by: [82]

$$\theta_D = \frac{h}{k_B} \left(\frac{4\pi}{9} \right)^{-1/3} \rho^{1/3} \left(\frac{1}{v_l^3} + \frac{2}{v_t^3} \right)^{-1/3} \quad (4.3)$$

where ρ is the density of the solid and v_l and v_t the longitudinal and transverse velocities of sound waves, respectively. These velocities are given by the following relations: [84, 85]

$$v_l = \left(B + \frac{4}{3} \mu \right)^{1/2} \rho^{-1/2}, \text{ and} \quad (4.4)$$

$$v_t = \mu^{1/2} \rho^{-1/2}, \quad (4.5)$$

where B is the bulk and μ the shear modulus. Eqs. (4.4) and (4.5) show the longitudinal and transverse velocity of sound waves, which are a function of the elastic properties as well as density (in the presented case of martensitic steel).

For the comparisons and results presented herein, the relations of reference [84] are implemented to calculate the values of elastic properties at several temperatures. The density of the used steel at different temperatures can be calculated from the analysis of Miettinen et al. [86].

Calculated values of the Debye-Waller factor B and the Debye temperature θ_D at different temperatures for the body-centered cubic (bcc) steel are shown in **Figure 4.1**. From these calculations, a Debye temperature of 468.3 K is found at 294 K (21 °C) sample temperature and

about 412.6 K when rising the temperature T to 873 K (600 °C). In contrast, the inverse trend takes place for the Debye-Waller factor, which starts at 0.328 \AA^2 at 294 K and increases to 1.5 \AA^2 at 873 K.

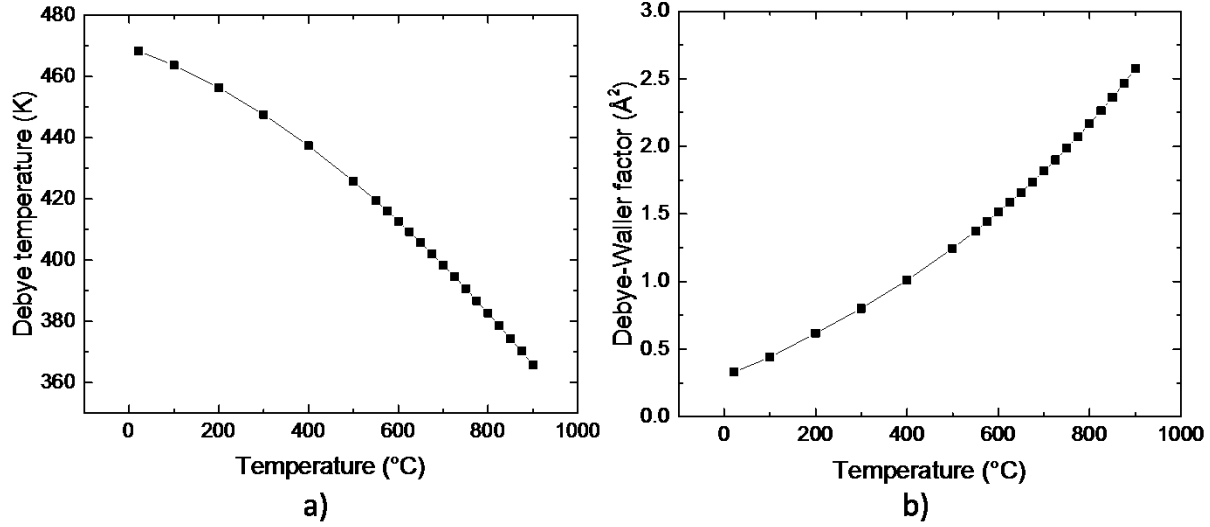


Figure 4.1. a) Calculated Debye temperature θ_D as a function of sample temperature. b) Calculated Debye-Waller factor B for the same sample (super martensitic steel).

4.1.2 Scattering cross sections

To understand the temperature dependence of the Debye-Waller factor in polycrystalline materials, the total microscopic neutron cross section σ_{tot} of an isotope is calculated, which is the cross section to an incoming neutron to interact with the material. It is given by its incoherent and coherent scattering, σ_{coh} , σ_{incoh} , as well as its absorption, σ_{abs} , contributions [87, 88]:

$$\sigma_{\text{tot}}(\lambda) = \sigma_{\text{coh}}(\lambda) + \sigma_{\text{incoh}}(\lambda) + \sigma_{\text{abs}}(\lambda). \quad (4.6)$$

The probability for a neutron to be scattered is determined by the sum of the first two cross sections. In particular, coherent (ordered) scattering appears if a regular spacing of atoms causes many scattered waves to interfere constructively. Incoherent scattering occurs due to the randomness (disorder) of the phases of the scattered waves. Besides, one distinguishes between elastic and inelastic scattering, where the latter process describes the probability for neutron interaction with the sample's crystal lattice involving the creation or destruction of phonons throughout that the neutron loses or gains energy, while with elastic scattering this energy remains

constant. The total neutron attenuation coefficient considering the structure of the material can hence be written as: [88, 89]

$$\mu_{\text{tot}}(\lambda) = [\bar{\sigma}_{\text{coh}} S_{\text{coh}}^{\text{el}}(\lambda) + \bar{\sigma}_{\text{incoh}} S_{\text{incoh}}^{\text{el}}(\lambda) + \sigma_{\text{total}}^{\text{inel}}(\lambda) + \sigma_{\text{abs}}(\lambda)] \rho_A, \quad (4.7)$$

where ρ_A is the atomic density and $\bar{\sigma}_{\text{coh}}$ and $\bar{\sigma}_{\text{incoh}}$ are the average cross sections calculated from the scattering length b of the nucleus: [90, 91]

$$\bar{\sigma}_{\text{coh}} = 4\pi \langle b \rangle^2, \quad (4.8)$$

$$\bar{\sigma}_{\text{incoh}} = 4\pi (\langle b^2 \rangle - \langle b \rangle^2), \quad (4.9)$$

The scattering functions S describe the influence of the spatial arrangement of nuclei and their corresponding dependence on the neutron wavelength and $\sigma_{\text{total}}^{\text{inel}}(\lambda)$ the total inelastic scattering cross section:

$$\sigma_{\text{total}}^{\text{inel}}(\lambda) = \sigma_{\text{coh}}^{\text{inel}}(\lambda) + \sigma_{\text{incoh}}^{\text{inel}}(\lambda) = (\bar{\sigma}_{\text{coh}} + \bar{\sigma}_{\text{incoh}}) S_{\text{incoh}}^{\text{inel}}(\lambda), \quad (4.10)$$

The first component of Eq.(4.7) accounts for the coherent elastic component of the scattering cross section and is calculated by means of the structure factor F_{hkl} and the interplanar distance d_{hkl} for every set of planes in the crystal [88],[92]:

$$\bar{\sigma}_{\text{coh}} S_{\text{coh}}^{\text{el}}(\lambda) = \frac{\lambda^2}{2V_0} \sum_{\text{hkl}} |F_{\text{hkl}}|^2 d_{\text{hkl}}, \quad (4.11)$$

where V_0 is the unit-cell volume and the structure factor F_{hkl} given by:

$$F_{\text{hkl}} = w_{\text{hkl}} \sum_n o_n b_n \exp(2\pi i (hx_n + ky_n + lz_n)) \exp\left(\frac{-B_{\text{iso},n}}{4d_{\text{hkl}}^2}\right), \quad (4.12)$$

where w_{hkl} the multiplicity of a lattice plane and o_n is the site occupation factor, which relates to the atom concentration. Furthermore, the placement (x, y, z) of the n – th atom is used to calculate the structure factor with respect to the hkl lattice plane. In addition, the absorption cross section is determined as: [93]

$$\sigma_{\text{abs}}(\lambda) = \frac{\sigma_{\text{abs}}^{2200}}{1.798 \text{ \AA}} \lambda, \quad (4.13)$$

where λ is the neutron wavelength, $\sigma_{\text{abs}}^{2200}$ the absorption cross section for thermal neutrons at a wavelength of $\lambda_0 = 1.798 \text{ \AA}$ (equivalent to a neutron standard velocity $v_0 = 2200 \text{ m}\cdot\text{s}^{-1}$).

The overall formulation of the total cross section is given by Granada [88] and Vogel [87]. It was later applied by Boin [58] in the nxsPlotter software for cross section calculations, which we use in this work. In this model, all types of neutron scattering of the material at different Debye-Waller temperatures as well as varying sample temperatures are included. This is given by its incoherent and coherent (elastic and inelastic) scattering as well as its absorption contribution as seen in **Figure 4.2a**. This calculation allows us to study the effect of the Debye-Waller factor on the total neutron cross section. Eq. (4.10) assumes the crystal to be a powder-like assembly of small crystal grains of random orientation.

The sum of the contributions from absorption and scattering is used to compute the transmission shown in **Figure 4.2b** via the attenuation coefficient μ as described by Beer–Lambert’s law:

$$I = I_0 e^{-\mu_{\text{tot}} l}, \quad (4.14)$$

where I_0 is the intensity of the incident beam and I is the intensity that is detected, while l is the sample thickness and the linear attenuation coefficient μ_{tot} is defined by the particle density N and the total microscopic cross section σ_{tot} : [92, 94]

$$\mu_{\text{tot}} = N \sigma_{\text{tot}}, \quad (4.15)$$

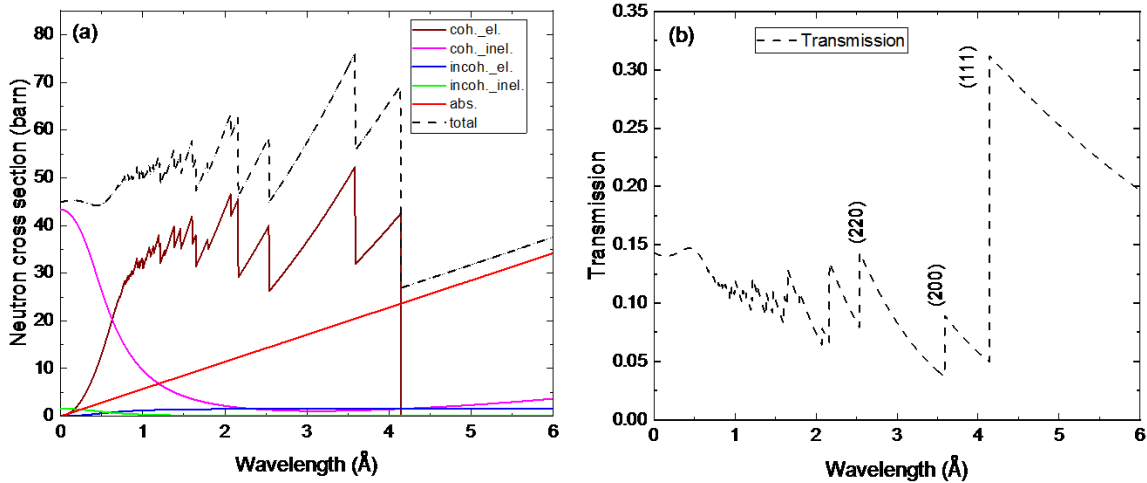


Figure 4.2. Theoretical neutron cross sections (a) for a fcc iron unit cell and (b) ideal transmission spectrum through 2-cm thick iron calculated by the nxsPlotter software [58].

4.2 Experimental details

Neutron wavelength selective experiments were conducted at the BERII research reactor of Helmholtz-Zentrum Berlin for Materials and Energy (HZB) in Germany by using the cold neutron radiography instrument (CONRAD-2) and a double crystal monochromator [59, 95, 96].

The CONRAD imaging setup consists of a 200- μm thick ^6LiF -scintillator converting transmitted neutrons into visible light, which is guided via a mirror to a CCD detector to form images. A double crystal monochromator allows for adjusting the wavelength continuously between 2 Å and 6 Å. More technical information about the instrumentation can be found elsewhere [7, 59, 63].

Ferritic super martensitic stainless steel (SMSS) X1CrNiMoCu12-7-3 (EN 1.4423) was selected for the present investigation. Its chemical composition is listed in Table 1. It has a bcc crystal structure.

Table 4-1. Chemical composition of the super martensitic stainless steel in wt%.

C	Mn	Si	Co	Ni	Cr	Mo	Fe
0.006	1.87	0.294	0.475	6.498	11.65	2.33	76.877

A sample of 33.1 mm x 9.3 mm x 5.6 mm (length x height x thickness) size was heated in a furnace while radiographic neutron imaging was performed.

At CONRAD-2, a series of wavelength scans at different temperatures, namely 21 °C, 200 °C, 400 °C, 500 °C, 600 °C, 700 °C and 800 °C were conducted. The sample was heated by two infrared heaters, each of which were equipped with six halogen quartz lamps and water-cooled polished aluminum reflectors which illuminate an area of 100 mm \times 75 mm. More technical information about the setup can be found elsewhere [97]. The sample was kept inside the innermost of two concentrically arranged quartz tubes as shown in **Figure 4.3**. Furthermore, the tube is sealed at the ends and the sample temperature was controlled remotely by a program written in LabVIEW utilizing feedback from a thermocouple attached to the sample. The sample was heated to different temperatures at a rate of 50 K /min.

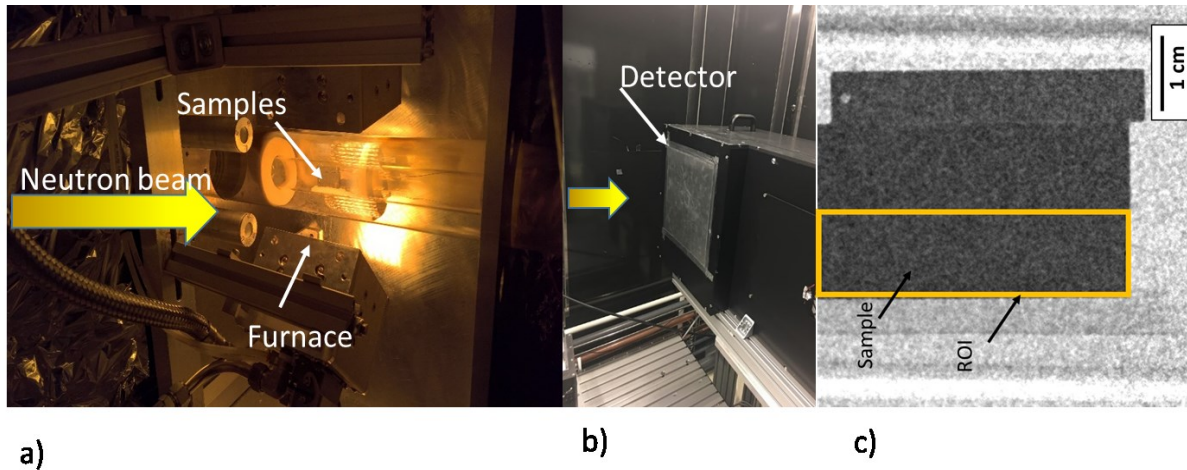


Figure 4.3. Experimental setup with a) furnace (placed in front of the detector). b) detector (shown without furnace for better visibility). c) the radiography image of the sample inside the furnace taken at 4.02 Å neutron wavelength (note that there are three samples, but this study focuses only on the sample that is highlighted by an orange box (ROI)).

With an exposure time for each image of 60 s, a wavelength scan from 3.7 Å to 4.2 Å and in some cases up to 4.4 Å with steps of 0.02 Å was performed, where for each step the transmission through the sample was measured. The transmission was obtained by normalizing the images of the sample by open beam images as well as dark field images. Thus, any beam inhomogeneity was corrected. The analysis of the images was accomplished by using the software ImageJ [98]. The wavelength dependent neutron transmission through the sample can be plotted for each pixel of the detector. However, for the presented results, the overall intensity of a region of 91 mm x 33 mm size (length x width) (at a constant sample thickness of 5.3 mm) was selected in order to increase the signal intensity (for faster measurements) and to reduce noise.

4.3 Results and Discussion

Figure 4.4 shows the effect of the temperature on the neutron cross section as calculated using the program nxsPlotter based on input parameters such as sample temperature, Debye temperatures and crystal lattice constants.

The largest coherent elastic scattering for any wavelength is found at low temperature (**Figure 4.4a**) and a nearly constant value of the neutron cross section of incoherent elastic scattering of ~3.5 barn is found for 0.1 K. (**Figure 4.4b**).

Next, the dynamic contributions due to thermal movements at 200 °C, 400 °C, 500 °C and 600 °C are calculated. Due to the fact that an atom in a crystal is never in rest but oscillates around its average position, and by using the Debye model for crystal vibrations, the coherent elastic scattering amplitude is reduced by the Debye-Waller factor as shown in **Figure 4.4a**.

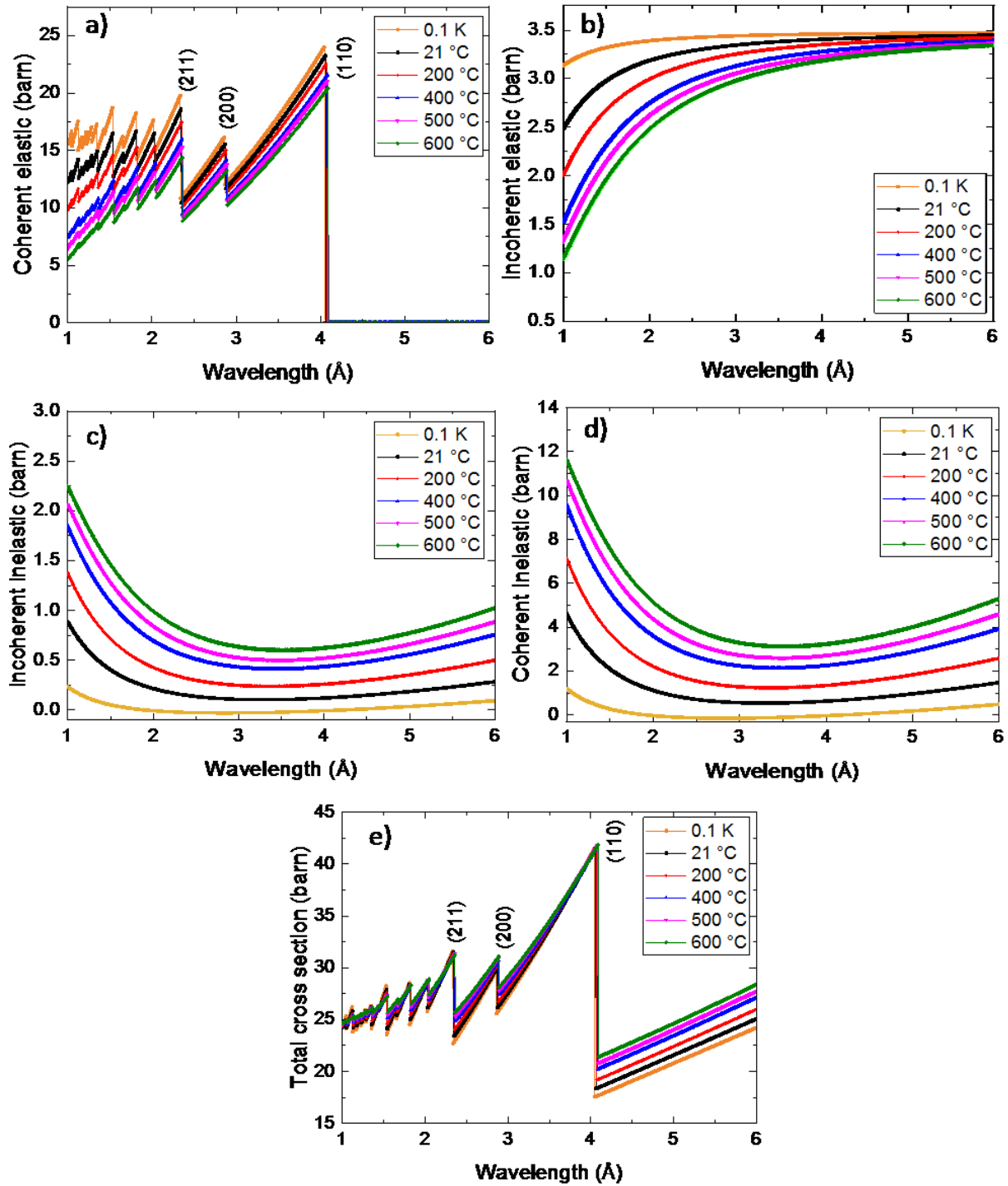


Figure 4.4. Calculated contributions (coherent and incoherent; elastic and inelastic) to the (total) neutron scattering cross sections of bcc iron for the static contribution at (0.1 K) and a dynamic contribution at five different temperatures.

According to the Bragg law, coherent elastic scattering by a crystalline material cannot occur for neutrons with longer wavelengths than λ_{\max} , which is twice the largest d-spacing of the possible reflections. This causes the typical Bragg edges. At elevated temperatures, the thermal expansion of the lattice distance causes a shift of the Bragg edge at wavelength λ_{\max} by approximately 0.013 Å, 0.027 Å and 0.042 Å at 200 °C, 400 °C and 600 °C, respectively. These values are calculated according to the lattice parameter of the phase with the same material (X1CrNiMoCu12-7-3) [99]. The shifts are seen best when the energy scale is magnified such as in **Figure 4.4c**.

As shown in **Figure 4.4b** the neutron cross section of the disordered (incoherent) part of elastic scattering decreases with temperature in a similar way as for the ordered (coherent) component because the cross section is proportional to the Debye-Waller factor. Moreover, for longer wavelengths beyond the cut-off wavelength for coherent scattering λ_{\max} , the incoherent part of the cross section provides a constant contribution of about 3.3 barns at 21 °C and the deviation of the neutron cross section at elevated temperatures is reduced, see **Figure 4.4b**.

The inelastic scattering contributions are shown in **Figure 4.4c** and **Figure 4.4d**. With increasing thermal motion, inelastic scattering becomes more and more important especially at long wavelengths and the effect of the Debye-Waller factor on the total neutron cross section is obvious. The cross section values of the coherent inelastic scattering part increase most (**Figure 4.4d**), for example from about 1 barn to 4 barns when going from 21 °C to 600 °C, but also for the incoherent inelastic part (**Figure 4.4c**) that increases significantly from about 0.012 barns to 0.588 barns for the same temperature increase (in both cases for 4.2 Å wavelength). For this wavelength, the temperature effect in absolute numbers is largest for coherent inelastic scattering, featuring an increase of 3.4 barns of cross section compared to 0.58 barns for inelastic incoherent scattering. For other wavelengths, the effect is similar.

In the total neutron cross section (**Figure 4.4e**), inelastic scattering gives rise to the most pronounced effect above the Bragg cut-off scattering at 4.2 Å where the coherent elastic part is zero.

In addition, the total neutron cross sections above the Bragg edge cut-off is proportional to the sample temperatures with total neutron cross sections of about 18.6 barns, 19.3 barns, 20.7 barns, 21.3 barns and 21.7 at 4.2 Å at temperatures of 21 °C, 200 °C, 400 °C, 500 °C and 600 °C, respectively as seen in **Figure 4.4e**.

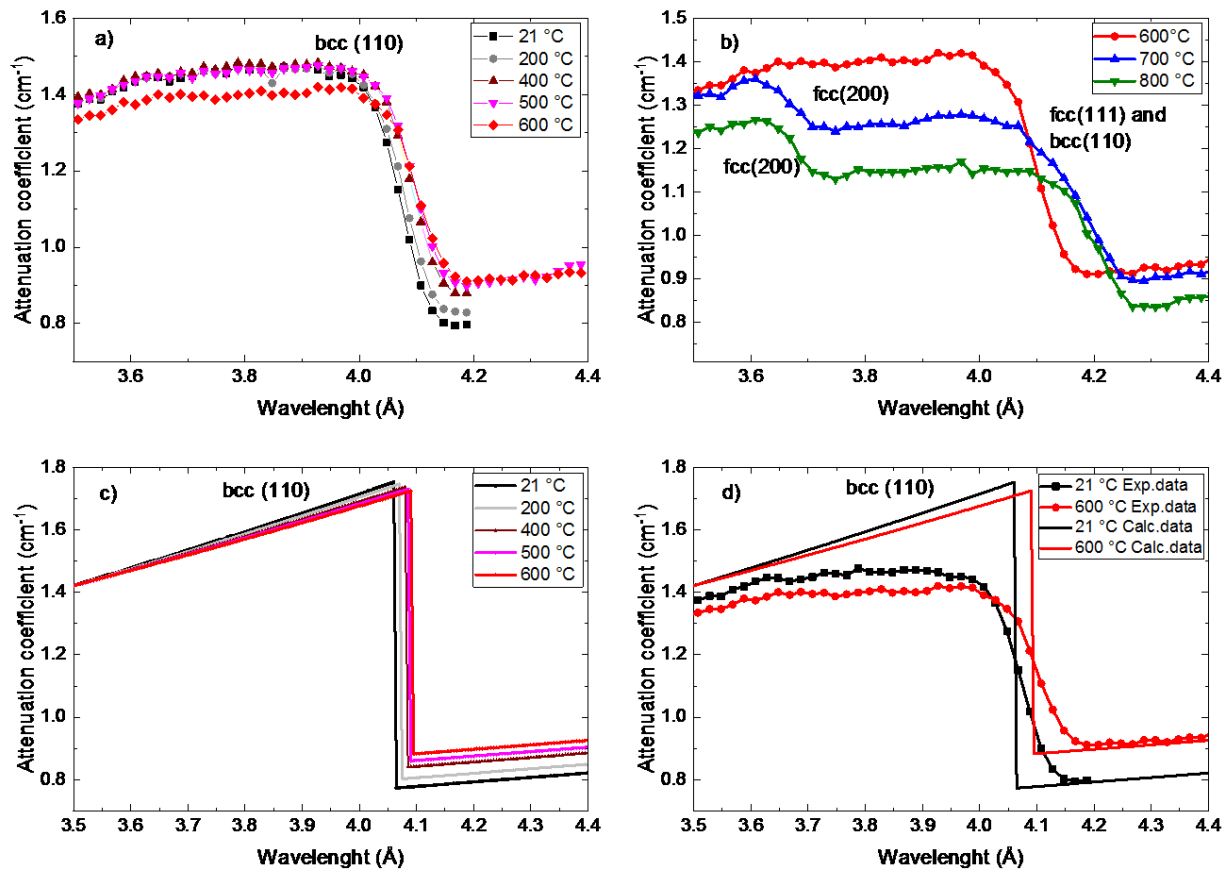


Figure 4.5. Calculated and measured wavelength dependent attenuation coefficients of bcc iron at temperatures between 21 °C and 800 °C. a) Measurements at 21 °C, 200 °C, 400 °C, 500 °C and 600 °C b) Measurements at 600 °C, 700 °C and 800 °C, where we observe a gradual phase transformation from martensite to austenite with temperatures exceeding 600 °C c) values calculated using software nxsPlotter d) comparison between experimental data measured at 21 °C and 600 °C - taken from a) - and corresponding calculated values given in c).

Wavelength scans of the wavelength dependent attenuation coefficients at the Bragg edge between 3.5 Å to 4.4 Å are shown in **Figure 4.5**.

The attenuation coefficient at a wavelength of 4.2 Å as seen in **Figure 4.5a** shows a notable increase during heat treatment from 21 °C to 600 °C from about 0.8 cm⁻¹ to 0.95 cm⁻¹ respectively. In addition, the changes of the measured attenuation during heating of the sample up to 500 °C at a wavelength of 3.9 Å (see **Figure 4.5a**) are small and agree well with the calculated results (**Figure 4.5c**). However, at 600 °C a significant drop of the measured attenuation coefficient from 1.46 cm⁻¹ to 1.39 cm⁻¹ at 3.9 Å is observed.

The wavelength-dependent attenuation coefficients measured at 600 °C, 700 °C and 800 °C given in **Figure 4.5b** show that austenitization starts already around 600 °C and the fraction of austenite gradually increases upon heating as can be concluded from the Bragg edge appearing at $\sim 3.6 \text{ \AA}$, which corresponds to the (200) plane of a fcc lattice. Correspondingly, the (110) Bragg edge of the bcc structure at $\sim 4.2 \text{ \AA}$ is fading, while fcc (200) becomes more pronounced.

Figure 4.5c shows calculated attenuation coefficients at various temperatures. A rather small variation is found for the attenuation coefficient through a temperature rise before the Bragg edge at a wavelength of 4.05 \AA which is in total a drop of approximately 0.06 cm^{-1} through temperature change from 21 °C to 600 °C (i.e. from 1.69 cm^{-1} to 1.63 cm^{-1}).

Furthermore, at elevated temperatures the thermal expansion of the lattice distance causes a shift of the Bragg edge at wavelength λ_{max} from 21 °C to 600 °C by approximately 0.040 \AA as seen in **Figure 4.5c**.

In **Figure 4.5d**, measured and calculated attenuation coefficients are compared. Unlike the sharp calculated Bragg edge, the experimental data exhibit a gradual decrease of attenuation from 3.95 \AA to 4.15 \AA , which is common for a real microstructure containing local misorientations and texture and giving rise to multiple scattering [23, 62].

In addition, the influence of the temperature rise from 21 °C to 600 °C in both measured and calculated attenuation coefficients is clearly shown at 4.2 \AA , showing an increase of the attenuation coefficient from about 0.77 cm^{-1} to 0.91 cm^{-1} .

Moreover, the comparison between measured and calculated attenuation coefficients at 3.9 \AA from 21 °C to 600 °C shows only minor variations of the calculated attenuation coefficient from 1.65 cm^{-1} to 1.62 cm^{-1} , but in contrast, a notable drop of the measured attenuation coefficient from 1.46 cm^{-1} to 1.39 cm^{-1} is observed. This observation also supports the assumption that this notable decrease in attenuation is caused by the start of transformation from martensite to austenite since the neutron attenuation by martensite is larger than by austenite within the wavelength range between 3.6 \AA to 4 \AA as shown in **Figure 4.6**.

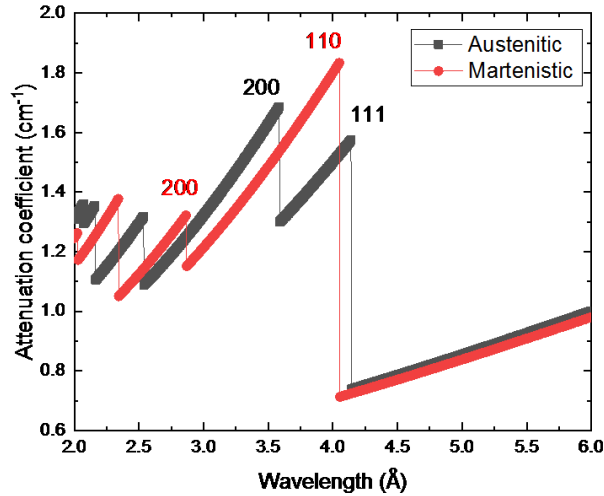


Figure 4.6. Comparisons between the attenuation coefficient of the martensitic structure and the austenitic structure at 21 °C as calculated by the software nxsPlotter.

Bragg edge height and position are extracted from the attenuation coefficient spectrum by using nonlinear least squares fitting. The derivative of the attenuation spectrum is taken and a Gaussian fit applied. The area of the Gaussian represents the height of the Bragg edge as shown in **Figure 4.7a**. On the other hand, the theoretical Bragg edge height is determined by subtracting the minimum from the maximum attenuation coefficient value as a function of temperature. The results are shown in **Figure 4.7b** and **Table 4-2**.

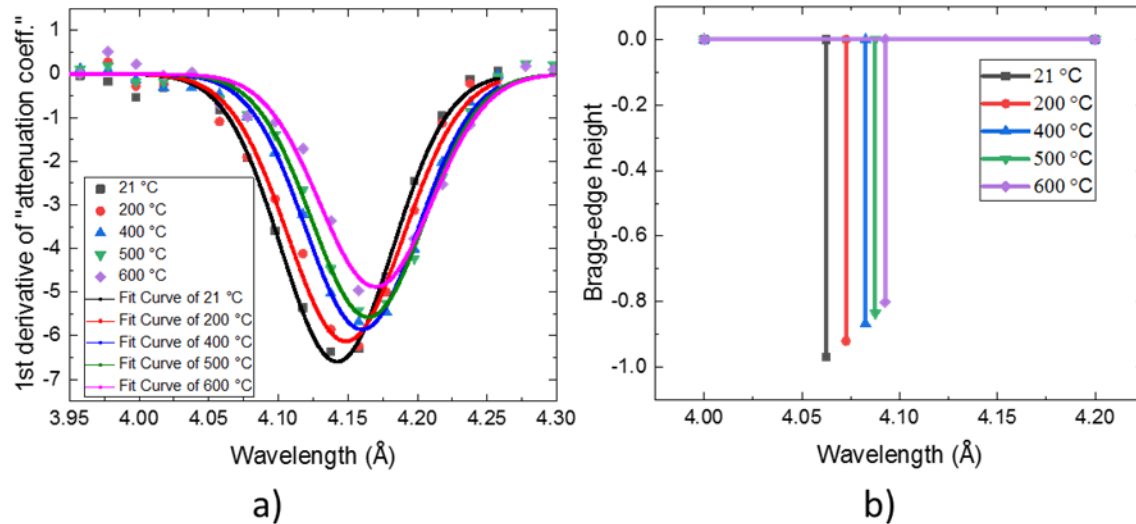


Figure 4.7. Bragg edge height of the attenuation coefficient profile for the five different temperatures (21 °C, 200 °C, 400 °C, 500 °C and 600 °C) by: a) Derivative and Gaussian fit of the measured Bragg edge. b) Values of the Bragg edge height calculated by subtracting the minimum and maximum value of the attenuation coefficient from Figure 4.5c. The distinct shift of the position is a result of changing thermal expansion.

Table 4-2. The height and the relative height of the Bragg edge as a function of temperature as measured and calculated.

Temperature (°C)	Bragg edge height experiment	FWHM	($\Delta\lambda/\lambda$) (%)	Bragg edge height calculated	Relative Bragg edge height experiment (%)	Relative Bragg edge height calculated (%)
21	-0.663±0.014	0.09	2.2	-0.969	100	100
200	-0.637±0.026	0.09	2.2	-0.920	96±4	95
400	-0.591±0.014	0.09	2.2	-0.867	89±3	89
500	-0.561±0.016	0.09	2.2	-0.836	85±3	86
600	-0.491±0.020	0.09	2.2	-0.802	74±4	83

The spectral resolutions ($\Delta\lambda/\lambda$) of the CONRAD-2 instrument are given in **Table 4-2**. The spectral resolution remains constant at ~2.2% through the temperature rise. The error estimates determined from the least squares fit are obtained for the five Bragg edge peaks at several different temperatures and the relative total errors are calculated by Eq. (4.17).

The influence of the thermal vibrations of atoms with increasing temperature on the Bragg edge height can be observed in both measured and calculated data. In order to calculate the relative decrease, the measured heights must be normalized with respect either to the initial height or to final height.

The value at 21 °C is taken as the initial height $h(21^\circ \text{C})$ of the Bragg edge. The relative decrease of the Bragg edge height is calculated using Eq. (4.16) for all temperatures applied, for both experiment and calculation as shown in **Table 4-2**.

$$\text{Relative Bragg edge height} = \left[1 - \frac{h(21^\circ \text{C}) - h(T^\circ \text{C})}{h(21^\circ \text{C})} \right], \quad (4.16)$$

$$\text{Total error} = \frac{h(21^\circ \text{C}) - h(T^\circ \text{C})}{h(21^\circ \text{C})} \left[\frac{\sqrt{(E_{h(21^\circ \text{C})})^2 + (E_{h(T^\circ \text{C})})^2}}{h(21^\circ \text{C}) - h(T^\circ \text{C})} + \frac{E_{h(21^\circ \text{C})}}{h(21^\circ \text{C})} \right], \quad (4.17)$$

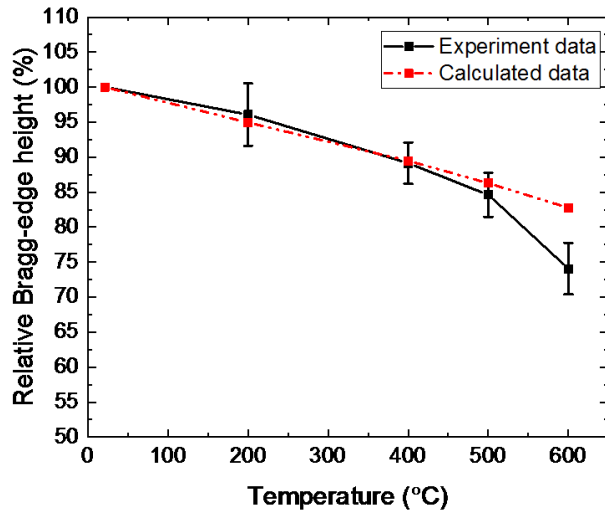


Figure 4.8. Relative decrease of the height of the Bragg edge as a function of temperature as calculated and measured. At 600 °C, the experimental value is ~33% below the calculation due to effect of incipient transformation to austenite. Error bars indicate the total standard deviation calculated from the relative Bragg edge height.

As a result, the Bragg edge height decrease of the experiment at 200 °C, 400 °C and 500 °C are about 4%, 11% and 15% respectively lower than a 21 °C as seen in **Figure 4.8** and **Table 4-2**, which can be fully attributed to the Debye-Waller factor. This trend, caused by the temperature rise, is in good agreement to the calculated results.

At 600 °C, the experimental Bragg edge height drops to 74.4% whereas the calculation predicts only a drop to 83%. This difference can be attributed to the appearance of austenite, which starts to form during heating while the volume fraction of the martensitic phase is reduced [99]. In addition, the height of the Bragg edge for the austenite is smaller than for the martensitic phase at 21 °C. Therefore, it can be clearly seen at 600 °C that this change in height of the Bragg edge is caused by the superimposition of two effects, the Debye-Waller factor and the martensite-to-austenite phase transformation.

4.4 Conclusions

The influence of thermal effects on the Bragg edge height has been studied by carrying out neutron attenuation measurements on a martensitic steel at different temperatures and comparing data with

calculations based on the nxsPlotter library. The Debye-Waller factor was used to describe the observed effects.

Thermally induced vibrations affect all contributions to neutron scattering including elastic and inelastic scattering. However, with increasing crystal temperature the elastic neutron cross section decreases whereas the inelastic scattering cross section increases. In addition, the coherent inelastic scattering has a significant effect on the change of the cross section when heating the sample compared to the other neutron cross section contributions.

The changes in the scattering intensities due to the thermal movement of atoms in a martensitic sample have been determined by analysing the neutron attenuation coefficients. A significant reduction in Bragg edge height was observed at elevated temperatures. The analysis of the attenuation coefficients showed that the Bragg edge varies in height for two reasons: the Debye-Waller factor decreases the diffracted intensity with increasing temperatures and phase change reduces the volume fraction of the martensitic phase. In martensitic steel up to 500 °C Bragg edge height reduction can be fully assigned to the Debye-Waller factor.

The theoretical and experimental data are in good agreement except in the high-temperature range where the phase starts to change from martensite to austenite, which have not been considered in the theoretical calculations

The observed effect is notable with a 15 % change of attenuation coefficient (Bragg edge height) at 500 °C. If this effect is not taken into account properly wrong interpretations of in-situ heating/cooling experiments could be the consequence.

This study can be used as a basis to introduce corresponding corrections in future experiments such as precise determination of phase volume fractions during in-situ heat treatments by improved interpretation of transmission spectra where typical analysis of the Bragg edges are utilized. Besides accounting for this effect, a method to determine sample temperatures in in-situ neutron transmission measurements could be developed.

5 Energy-selective neutron imaging by exploiting wavelength gradients of double crystal monochromators – simulations and experiments.

The capability of wavelength resolved neutron transmission experiments is nowadays well known. This chapter focuses on the performance of double crystal monochromators, which are widely used at various imaging facilities. Simulation results based on neutron ray tracing are compared with experimental results in order to provide a better understanding of the device. Its design and geometry is shown in **Figure 2.2**.

Note: The following parts have been submitted to the “Nuclear Instruments and Methods in Physics Research Section A: Accelerators, Spectrometers, Detectors and Associated Equipment”, Authors: A. M. Al-Falahat, N. Kardjilov, T. V. Khanh, H. Markötter, M. Boin, R. Woracek, F. Salvemini, F. Grazzi, A. Hilger, S. S. Alrwashdeh, J. Banhart and I. Manke

5.1 Results and discussion

The simulation performed here is equivalent to an open beam measurement, i.e. there is no sample in the beam to be transmitted.

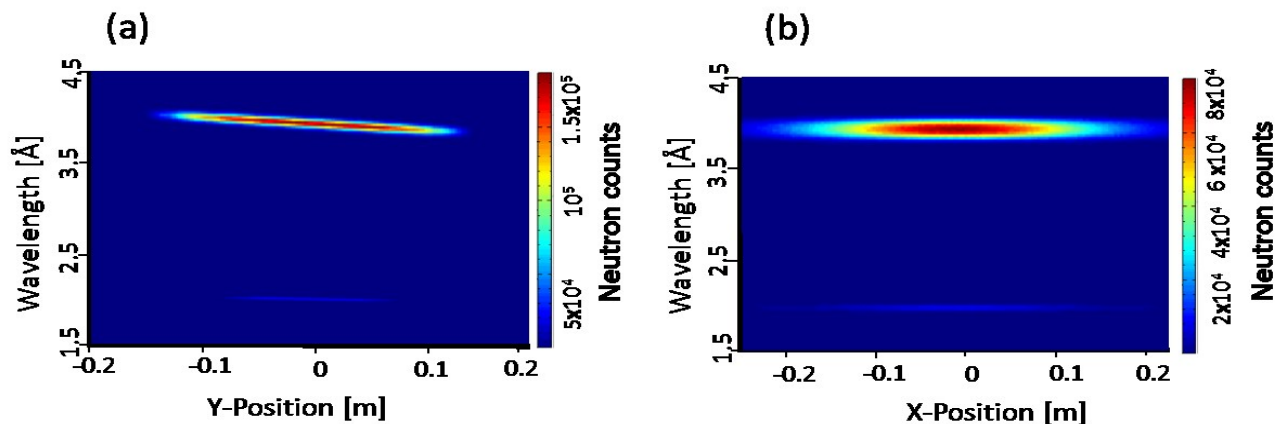


Figure 5.1. The wavelength distribution at the detector x and y position for $\lambda=4$ Å obtained by using a ‘LambdaYPSD_monitor component’ of McStas. a) Y-Position; b) X-Position.

The calculated intensity distribution as a function of neutron wavelength for varying vertical positions on the McStas LambdaYPSD_monitor for the monochromator set to 4 Å is shown in

Figure 5.1a. A slope of the neutron wavelength distribution (i.e. gradient of wavelength) along the (vertical) Y-axis is clearly visible. The analogous horizontal distribution along the X-axis is shown in **Figure 5.1b**. Contrary to the vertical position, the neutron wavelength along the horizontal X-axis remains the same, i.e. no change in neutron wavelength over the width of the detector occurs. The second order monochromator reflection, which also satisfies the Bragg condition, leads to neutron intensity distribution around 2 Å which can be seen in the graph as well. This has to be taken into account also for the experimental setup.

For an estimation of the wavelength distribution at different positions on the detector plane, the wavelength monitors were used in two positions (X and Y position) with 10 cm distance between them, see **Figure 5.2a**. The neutron spectra for different mosaicities of the crystals (0.8, 2.0 and 3.0) were measured in boxes of 1 cm x 1 cm in order to estimate the wavelength gradient in the horizontal and vertical directions as described above. The results for the horizontal direction (P4, P1 and P5) and for the vertical direction (P3, P1 and P2) are shown in **Figure 5.2**. In addition, the intensity distribution over the detector plane is shown.

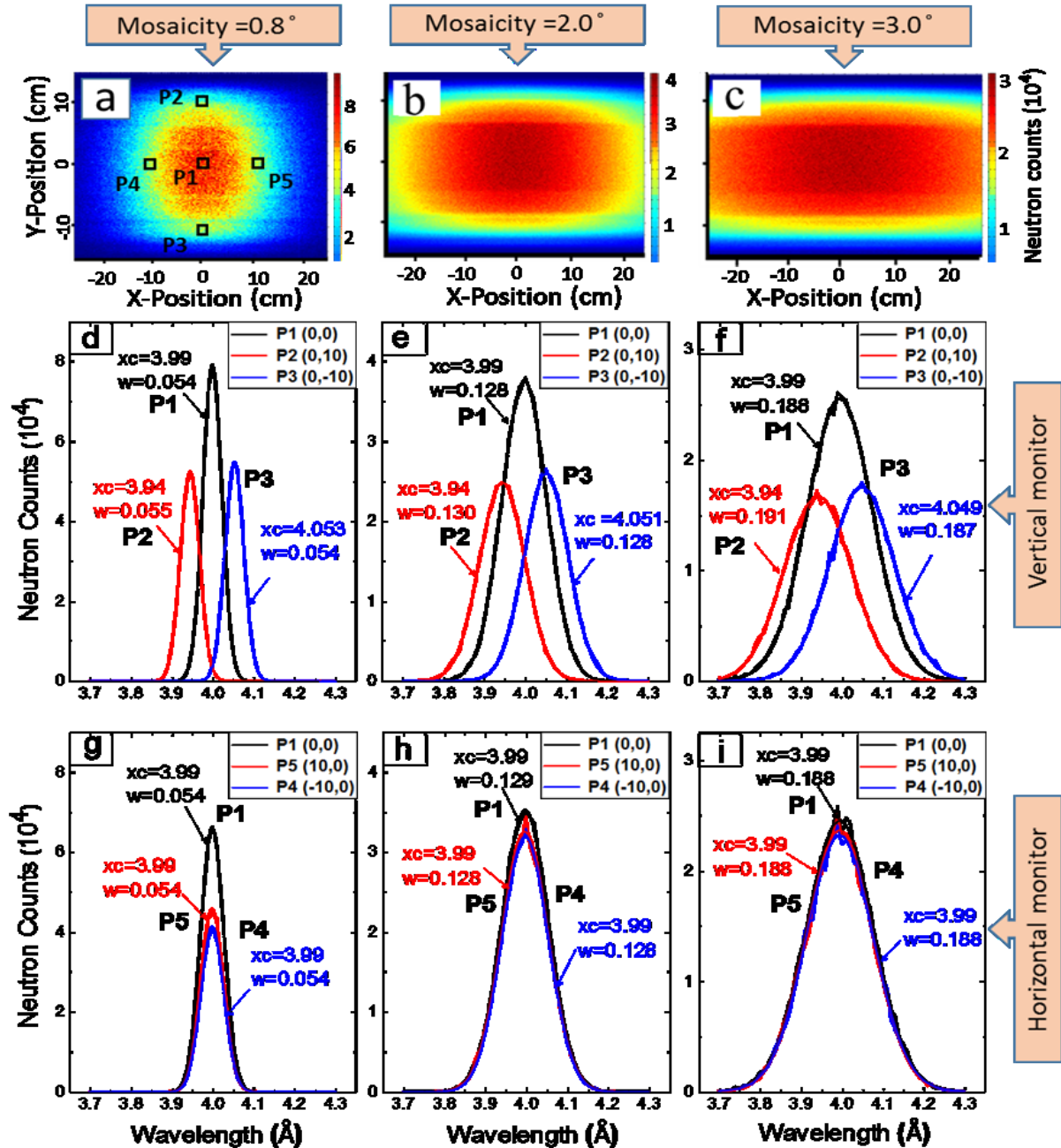


Figure 5.2. Images in first row – a), b) and c) – show the simulation simulated intensity captured by the PSD-monitor of cross section (50 cm x 30 cm) for three different mosaicities 0.8, 2.0 and 3.0. Second and third rows display wavelength-resolved intensities captured by the five L-monitors. P3, P1, P2 are arranged vertically (d), e), f), bottom to top), P4, P1, P5 horizontally (g), h), j), left to right). The symbols x_c and w represent the centre and the FWHM of a Gaussian fitting respectively. Monochromator set to 4 Å.

The values for the wavelength resolution taken from **Figure 5.2** (x_c and w , represent the centre and the FWHM of Gaussian fitting respectively) are summarised in **Table 5-1**.

Table 5-1. The peak positions and the wave resolutions of the middle region (P1) at a different mosaicities. Scatter bar reflects values given by the software McStas and the Gaussian fit software Origin.

Mosaicity	Peak position (x_c) (P1) (Å)	($\Delta\lambda/\lambda$)(%)	Area under the curve (P1)
0.8°	3.9996(4)	1.36	7040.4
2°	3.9980(21)	3.20	8081.5
3°	3.9957(44)	4.70	8070.8

The following statements can be derived from these results:

- The wavelength resolution ($\Delta\lambda/\lambda$) gets worse with increasing crystal mosaicity, following a linear trend for the used range, see **Table 5-1**.
- For crystal mosaicities larger than the divergence of the incident neutron beam (estimated to be 1° determined by the reflection from the walls of the neutron guide), the neutron flux at the sample position does not depend on the crystal mosaicity, which means that a larger mosaicity provides larger beam divergence and the neutrons are distributed over a larger area. In this way, the neutron flux is fixed for a certain distance between the monochromator and the detector. This statement is confirmed by the values shown in **Table 5-1** where the neutron flux (area under the curves in **Figure 5.2**) is the same for the crystal mosaicities (2° and 3°) but smaller for the crystal with a mosaicity of 0.8°.
- The beam size increases asymmetrically with the increase of crystal mosaicity (**Figure 5.2 a-c**). The increase is in the direction pointing along the rotation axis of the monochromator only.

5.1.1 Comparison with experimental results

In order to verify the results of the Monte Carlo simulations wavelength distributions were determined experimentally within the detector plane at the neutron imaging instrument CONRAD-2 located at the reactor of the Helmholtz-Zentrum Berlin for Materials and Energy (HZB, Germany) [63, 95]. For this purpose, a mild steel (body-centred cubic (bcc) crystal structure) plate of dimensions 30 cm x 30 cm x 1 cm (B x H x T) was used to cover the detector. A double-crystal monochromator with the parameters used in the Monte Carlo simulations and mosaicity of 0.8°

was used to select different neutron wavelengths. A wavelength scan from 3.6 Å to 4.5 Å in steps of 0.02 Å was performed. For each step, the transmission through the mild steel plate was measured by the position sensitive detector. A transmission map was obtained by normalizing the images of the sample by the open beam images, thus correcting for the beam inhomogeneity. As a result, a wavelength-dependent neutron transmission through the steel plate can be plotted for each point/pixel of the detector.

The analysis of the images was accomplished by using ImageJ, where the height of the plate was discretised by rectangular regions of interest (ROI) of 1 cm height and 25cm width, as shown in **Figure 5.3a**. The wavelength-dependent transmission showing the Bragg edge for bcc steel can be plotted for each ROI in the vertical direction as shown in **Figure 5.3** for three ROIs (#2, #12 and # 22).

In order to investigate the wavelength variation, a ROI#12 is selected to be the middle of the field of view and ROI #2 as well as ROI#22 are at 10 cm distance below and above the middle region as shown in **Figure 5.3a**.

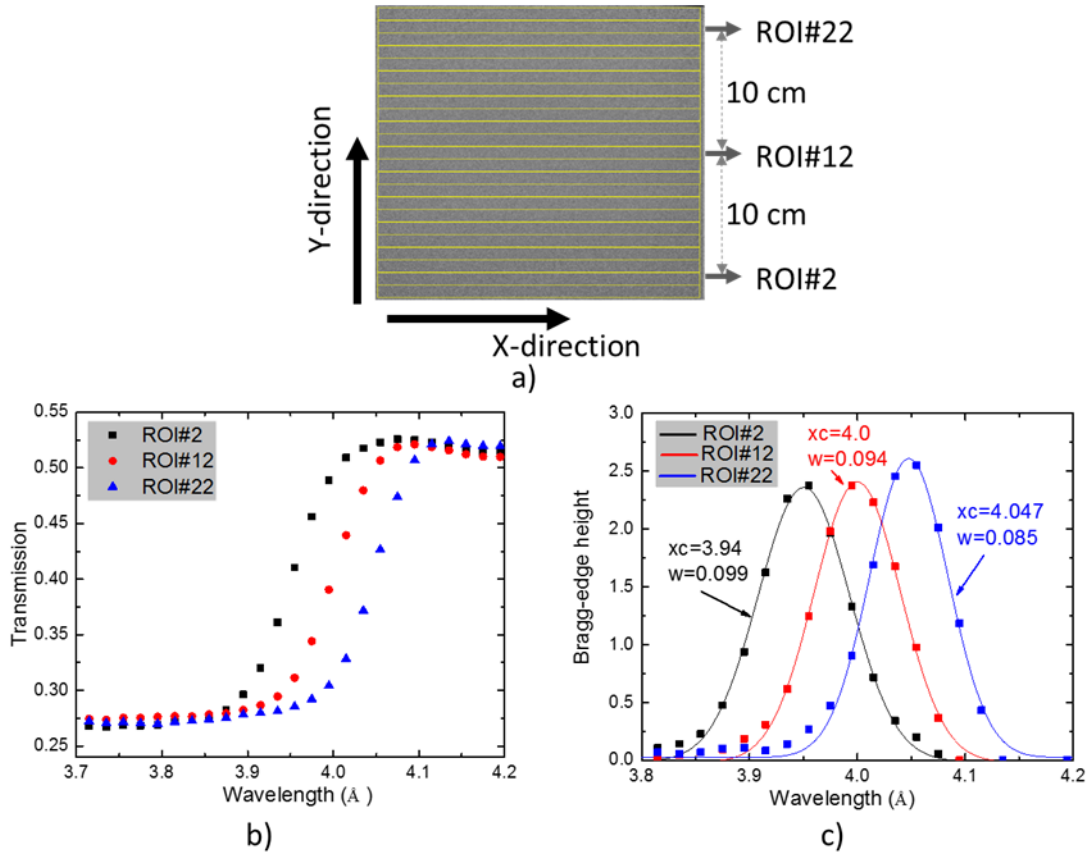


Figure 5.3. a) Radiographic image of steel plate divided into 23 ROIs with dimensions of 1 cm height x 25 cm width from the lower to the upper edge along the Y-direction. b) Bragg edge positions for three different Y-positions (corresponding to P2, P1, P3 in the simulations) c) Derivative and Gaussian fit of the Bragg edge transmission profiles for the same three Y-positions. The symbols x_c and w represent the centre and the FWHM of the Gaussian fitting, respectively.

The position of the Bragg edge was determined by nonlinear least squares fitting. The derivative of the transmission spectrum is taken and a Gaussian fit applied. The centre of the Gaussian represents the location of the Bragg edge and corresponds to a Bragg peak shift as shown in **Figure 5.3c**. This shift is a result of the wavelength gradient produced by the double-crystal monochromator. The obtained Gaussian fitting parameters are shown in **Figure 5.3c** and allow us to compare the experimental data with the Monte Carlo simulation results. Such a comparison is presented in **Table 5-2**.

Table 5-2. Comparison of the wavelength shift obtained from the simulation and from the experiment. Mosaicity = 0.8°.

position	$\lambda_{\text{centre}} (\text{Å})$		$\Delta\lambda$ (Wavelength shift (Å))	
	Experiment	Simulation	Experiment	Simulation
Upper ROI#22	4.047	4.053	0.047	0.053
Middle ROI#12	4.000	3.999	0	0
Bottom ROI#2	3.946	3.945	0.053	0.054

An agreement between experimental and simulated data better than 1 % for the absolute wavelength values was obtained, which proves the reliability of the simulations. In addition, one can conclude that the wavelength shift over 10 cm distance in the vertical direction is approximately 0.05 Å.

5.1.2 Wavelength-gradient translation imaging (WGTI)

While seemingly an undesired effect, the wavelength gradient obtained can be used for imaging purposes in order to measure the Bragg edges of different materials without performing a scan with the double-crystal monochromator. For this, it is necessary to select a wavelength in the middle of the Bragg edge. When the sample is translated through the wavelength gradient (e.g. from top to bottom) a narrow Bragg edge profile will be obtained. The advantage compared to the traditional wavelength scanning method is an increased wavelength stability due to the missing uncertainty coming from the mechanical fine-positioning system of the monochromator orientation for each step of a scan.

An example for such an investigation is presented in **Figure 5.4**, where a Roman coin made of bronze (face-centred cubic (fcc) crystal structure) was fixed by steel screws (bcc crystal structure) and visualised using the two energy-selective methods. For the standard wavelength scan using the double-crystal monochromator a step of 0.01 Å was used. For wavelength gradient imaging, the double-crystal monochromator was set to 3.95 Å, 4.05 Å and 4.15 Å, where for each setting a stepwise shift of the sample over 20 cm with a step of 5 mm was performed. The wavelength regions covered by the three measurements are marked with different background colours in **Figure 5.4c**.

If we consider the measured wavelength shift of $0.05 \text{ \AA} / 10 \text{ cm}$ this means that the wavelength resolution per step of 5 mm would be 0.0025 \AA without considering the wavelength broadening due to the mosaicity of the crystals.

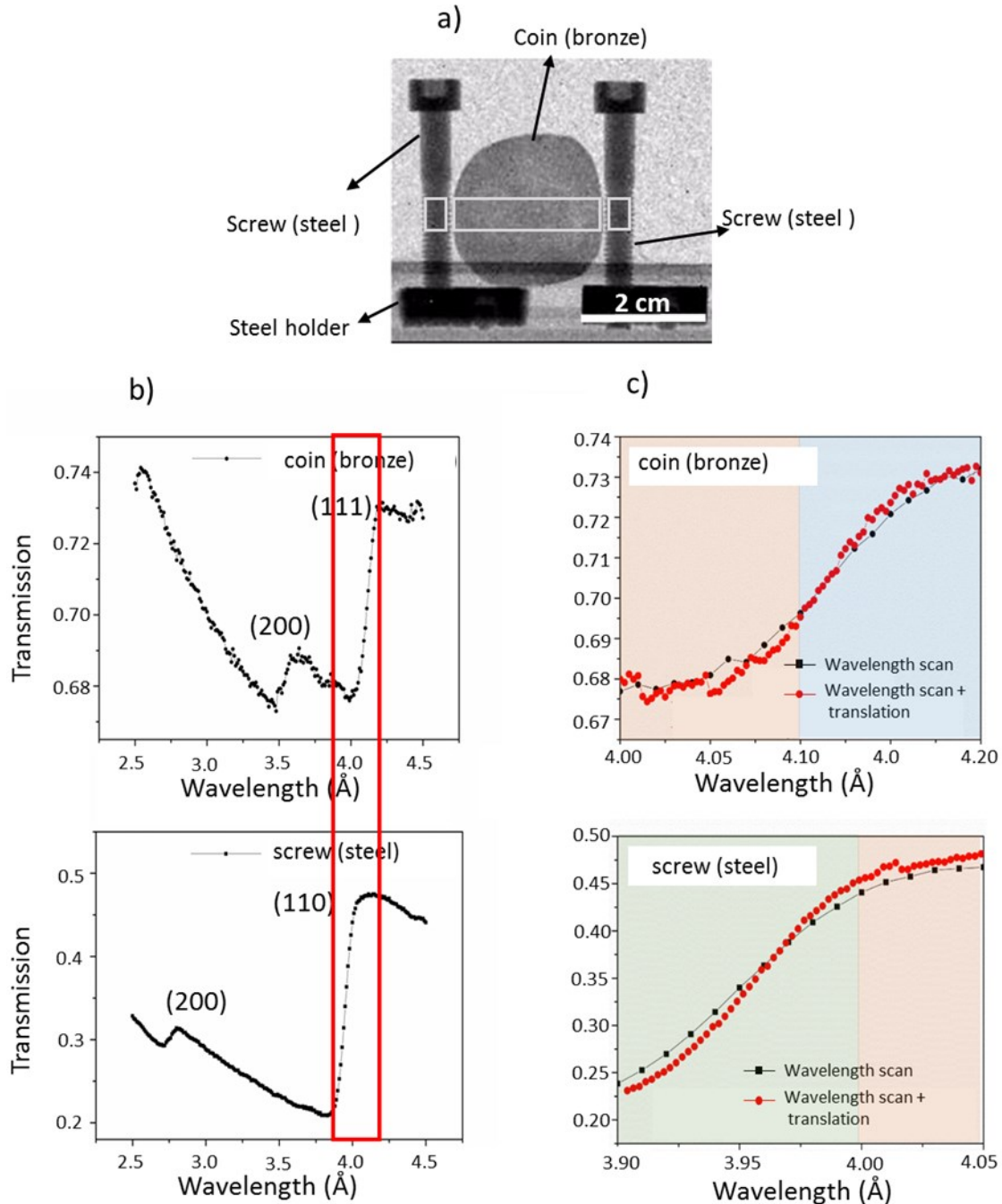


Figure 5.4. a) Radiograph of a bronze coin (fcc crystal structure) and steel screws (bcc crystal structure) holding the coin. White boxes denote 5 mm-high regions, in which transmission values were averaged. b,c) Comparison of the Bragg edges measured for bronze and steel by b) standard scanning and by c) wavelength gradient translation imaging. The red box corresponds to the wavelength range in c).

The correspondence of the Bragg edge profiles measured by the two methods shows that wavelength gradient translation imaging can be used for collecting data with excellent sampling resolution and supports a reliable fitting procedure providing the position and the amplitude of the Bragg edge. In addition, the WGTI method can be used for precise wavelength scans at facilities with static DCM device where the position of the monochromator crystals is fixed.

5.2 Conclusions

The double-crystal monochromator is a very important device for energy-selective imaging at continuous neutron sources. The simulations and analytical calculations presented herein help to understand its functionality and to optimise its parameters. The influence of crystal mosaicity on the beam size and intensity at the sample position was studied. The wavelength gradient caused by crystal mosaicity was simulated and measured and good agreement obtained. A new method for wavelength-gradient translation imaging (WGTI) using a translation scan through the wavelength gradient was proposed and tested. Such wavelength-gradient imaging provides better sampling (~200 times more points on the plot) of Bragg edge measurements and can be used to determinate its position and shape by using a fitting function. In addition, the new technique allows for wavelength scans at monochromator devices with fixed crystals.

6 Enhancement of the monochromatic beam resolution at the CONRAD-2 instrument based on a deconvolution algorithm.

Note: The following parts will be submitted to a scientific Journal, Authors: Ala'a M. Al-Falahat, Nikolay Kardjilov, Henning Markötter, Robin Woracek and Ingo Manke.

6.1 Theory

The recorded intensity $I(\lambda)$ spectrum can be represented as a convolution of broadening function $I_o(\lambda)$ with a higher resolution spectrum $I'(\lambda)$

$$I(\lambda) = I_o(\lambda) \times I'(\lambda), \quad (6.1)$$

The goal of the deconvolution technique is to take out the function $I'(\lambda)$ from Eq. (6.1). Using the convolution theorem, the deconvolution spectrum $I'(\lambda)$ can be stated as follow [100-102]

$$I'(\lambda) = F^{-1} \left\{ \frac{D(x)I(x)}{I_o(x)} \right\} \quad (6.2)$$

where F^{-1} is inverse Fourier transform, $D(x)$ is the familiar apodization function which is used to minimizing the amplitude of side-lobes in the deconvoluted spectrum i.e. produce the maximum improvement in the spectrum by smoothing the data where the function is unity when $x=0$ and falls to zero when $x=1$. Different forms of such a function are available [101, 103].

$I_o(x)$ is the Fourier transform (FT) of broadening function $I_o(\lambda)$ where $I_o(x)$ describes the line shape of the bands. There are various approaches to the interferogram $I_o(x)$ used as a deconvolution function. The Lorentzian line shape function is implemented in our work;

$$I_o(\lambda) = \frac{1}{\pi} \frac{\gamma'}{(\gamma'^2 + \lambda^2)}, \text{ and} \quad (6.3)$$

where the γ' is the half width at half maximum (HWHM) of the new spectrum band. If we consider the origin of the HWHM band to be γ_i then the HWHM will be reduced to $(\gamma_i - \gamma')$. It is also to note that the area of each band is unchanged and the peak of each band $(A_i^0)'$ is therefore increased to a value given by:

$$(A_i^0)' = A_i^0 \frac{\gamma_i}{(\gamma_i - \gamma')} \quad (6.4)$$

The ratio of the HWHM before and after deconvolution, $\gamma_i/(\gamma_i - \gamma')$, is called the resolution enhancement factor k [101].

For the data analysis presented in the current work, the Fourier deconvolutions code is written in MATLAB. The used deconvolution routine is based on the theory described above and it can be performed by varying two parameters: “ γ' ” and “smoothing factor X “. γ' is the amount by which the full bandwidth at half maximum (FWHM) is reduced and the smoothing factor X is used to smooth the deconvoluted spectrum which must be between 0 and 1. The larger the γ' the better the band narrowing, and the larger the smoothing factor X , the smoother the deconvoluted spectrum. Both parameters must be changed simultaneously to optimized the resolution enhancement procedure and to minimize deconvolution artifacts and distortions [102].

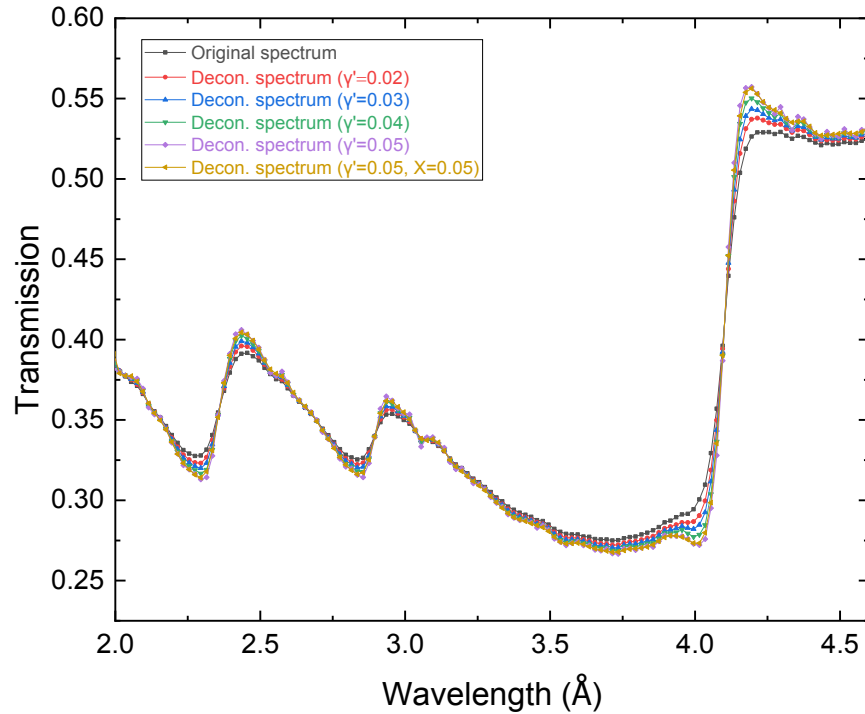


Figure 6.1. Series of a progressively deconvoluted spectrum of CONRAD-2 instrument profile at increasing of γ' (here 0.02, 0.03, 0.04 and 0.05) and the smoothing factor X .

A series of deconvoluted Bragg-edge spectra of bcc steel structure is shown in **Figure 6.1** where it can be seen that the resolution is greatly improved by using the resolution enhancement technique compared with the original spectrum. Since there is always noise present in the

experimental spectrum, the appearance of the typical side lobes is observed at around 4.1 Å. Therefore, the appearance of side lobes depends on the strength of the deconvolution as it increases with the increasing of γ' value. Furthermore, as smaller as possible the value of the filter should be used in order to obtain a comparable degree of smoothing of the deconvoluted spectrum as compared to the original spectrum.

The optimal deconvolution parameters from a theoretical point of view would be optimal to select a value for γ' that is as large as possible, corresponding to the resolution of the spectrum. However, in practice, the highest achievable resolution enhancement is limited by the S/N ratio. Noise in the spectrum is treated for the deconvolution procedure like bands with very low HWHM.

It must be noted that the original spectrum should be measured with the highest possible signal to noise ratio (S/N) in order to achieve maximum band narrowing and minimizing the noise and the side lobes. In some cases, fewer high resolution components through the spectrum range are observed and consequently, fewer high-frequency noise components remaining in the resultant deconvolved spectrum are negligible.

6.2 Experimental procedure

CONRAD-2: With an exposure time for each image of 20s a wavelength scan from 2.0 Å to 4.8 Å with steps of 0.02 Å was performed, where for each step the transmission through the sample was measured. The transmission was obtained by normalizing the images of the sample by open beam images as well as dark field images. Thus, any beam inhomogeneity was corrected. The analysis of the images was accomplished by using the software ImageJ [98]. As a result, the wavelength dependent neutron transmission through the sample was plotted for each pixel of the detector. The full width at half maximum (FWHM) of the Bragg edge was determined by nonlinear least-squares fitting. The derivative of the transmission spectrum was taken and a Gaussian fit was applied.

The higher order wavelength contamination of the monochromatic beam produced by a double crystal monochromator should be corrected using the Bragg's law.

$$2d_{hkl} \sin\theta = n\lambda \quad (6.5)$$

Where d_{hkl} is crystal plane spacing, θ is the orientation angle of the crystal planes in respect to the beam and λ the reflected wavelength of order $n = 1, 2, 3 \dots$. For an angle that should diffract the wavelength λ , the Bragg condition is fulfilled by $\lambda/2$ and $\lambda/3$ (and so on) as well.

This effect becomes very considerable at higher wavelengths as seen in **Figure 6.2**, therefore, the neutron monochromatic beam from the highly oriented pyrolytic graphite HOPG crystal (mosaic spread = 0.8°) and its higher order were simulated using McStas software for different neutron wavelengths. The wavelength distribution for a monochromatic neutron beam with a wavelength of 5 \AA produced by the double crystal monochromator is plotted in **Figure 6.2a**. It is clear that the intensity of the first order wavelength is contaminated with the higher orders (second and third order of reflections). This contamination is non-negligible and it is around 20% from the higher order at 5 \AA . Consequently, the relative contribution of the first order and the higher orders were calculated within the wavelength band from 2.8 \AA to 5.3 \AA as displayed in **Figure 6.2b**. It can be observed that the percentage of the second order reflection start effected at 3.3 \AA and increases with the wavelength. For instance, the contribution of the second order at 5.3 \AA is at about 28%.

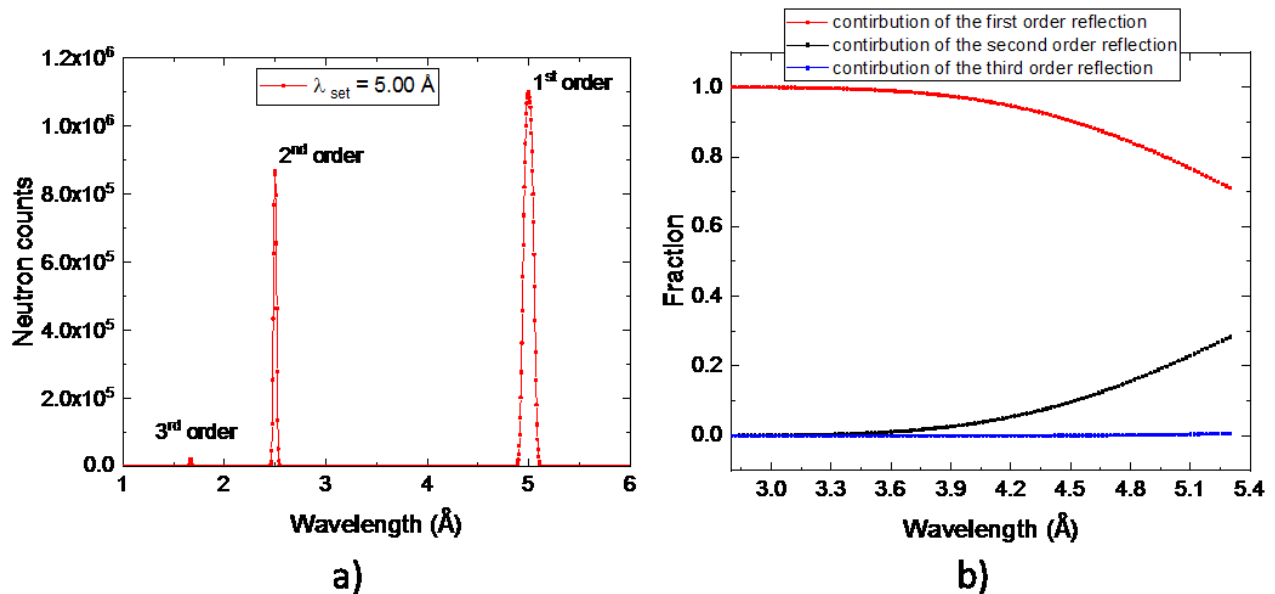


Figure 6.2. a) Recorded the first order and higher order of the CONRAD-2 spectrum for the double crystal monochromator set to 5 \AA . b) Relative contribution of the higher order component to the total number of a neutron by using McStas software.

Therefore, the transmission spectra can be corrected to eliminate the higher order beam components as clearly seen in **Figure 6.3**.

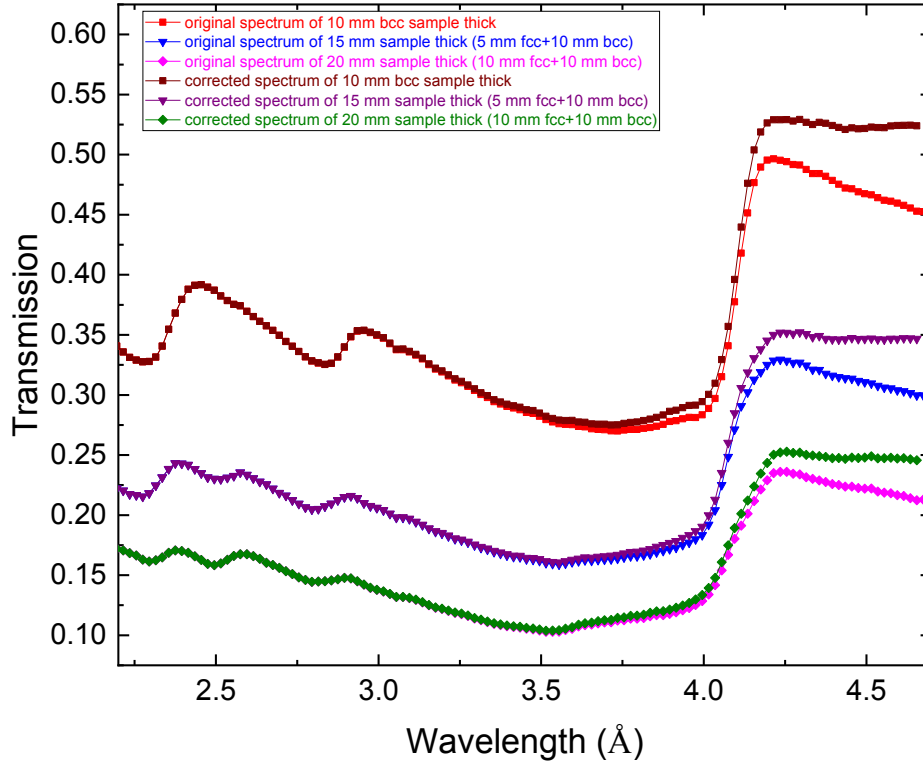


Figure 6.3. Comparison between the original and corrected transmission spectrum of CONRAD-2 instrument at a different thickness of both bcc and fcc steel structure.

6.3 Fourier-self deconvolution

In order to investigate the potential advantage of the deconvolution technique described above a wavelength transmission spectrum was measured by time of flight (TOF) technique which provides much better resolution (below 1%) than the double-crystal monochromator resolution of approximately 2.5 %. For this purpose, the ESS test beamline (TBL) at HZB was used. The neutron pulses were prepared by a wavelength frame multiplication (WFM) chopper arrangement at high resolution mode.

The results are shown in **Figure 6.3** for the high resolution setting recorded at detector position $L_{\text{det}} = 47.63$ m from the neutron source. The transmission of the neutron beam was obtained by recording the beam spectrum behind the sample. Steel samples with different fractions of bcc and fcc phases were selected. A measurement without sample was recorded as well in order to get the spectrum of the initial beam which was used to perform intensity normalization of the transmission spectra.

A python-based interface for processing and stitching of the TOF spectrum was applied within the MANTID software framework[72] in order to eliminate the frame overlap regions of the spectrum. As a result, the processed TBL spectrum is displayed in **Figure 6.4**.

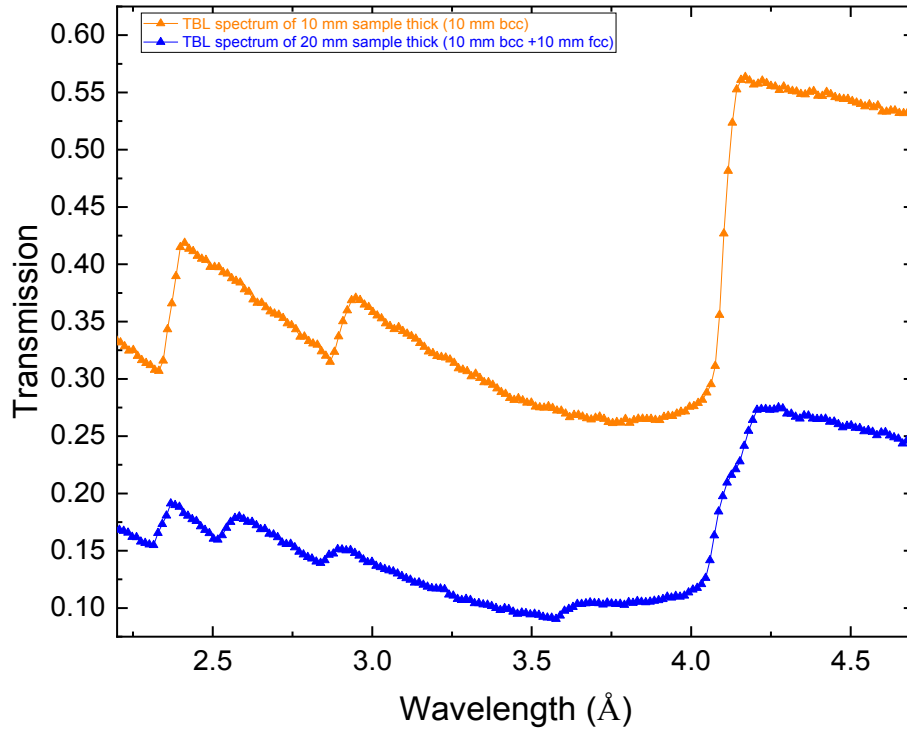


Figure 6.4. TBL transmission spectrum of high resolution mode at a different thickness of both bcc and fcc steel structure. The highest resolution setting produces relatively sharpest Bragg edge as expected and shoulder on the Bragg edge at around 4.1 Å is observed due to the double phase of bcc and fcc structure.

The comparison between the transmissions spectra from the two instruments CONRAD-2 and ESS Test beamline (TBL) are shown in **Figure 6.5**. It can be seen that the sharp Bragg edges from the TBL are pronounced while the Bragg edges obtained from the CONRAD-2 instrument show coarse resolution. Furthermore, the sharp TBL Bragg edge shows a shoulder like shape with a double edge which is not visible at on the CONRAD-2 spectrum around 4.1 Å for the sample with 50% fcc (austenite) and 50% bcc (10 mm bcc and 10 mm fcc plates placed behind each other).

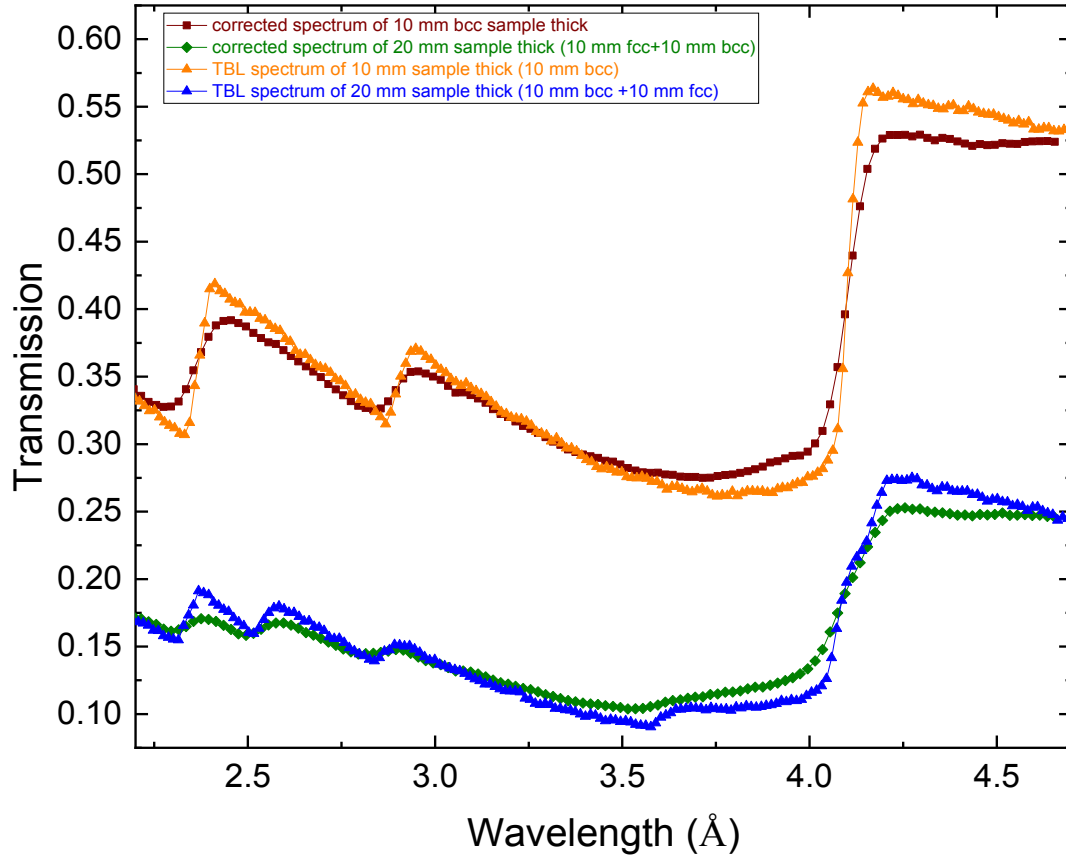


Figure 6.5. Comparison between TBL transmission spectrums of high resolution mode for 10 mm thick of bcc phase and 20 mm total thickness (10 mm bcc phase and 10 mm fcc phase behind each other) and corrected CONRAD-2 spectrums at the same samples

Using the deconvolution procedure described above the wavelength resolution of the spectra taken at the CONRAD-2 instrument can be enhanced and compared with TBL spectrum. The choice of optimal deconvolution parameters is important for this type of spectral analysis. In our approach, the degree of deconvolution is determined by the values of two parameters: $\gamma' = 0.065$ and a smaller value of the filter must be used to obtain a comparable degree of smoothing as compared to an original spectrum, here $X= 0.02$ is selected. In this way, the deconvolution provides the best matching between the CONRAD-2 with the TBL spectrum as shown in **Figure 6.6a**. In our case, the resolution enhancement factor K is 3.16, which means that the deconvolution approach increases the wavelength resolution of CONRAD-2 instrument by a factor of 3.16.

To illustrate the effect of the Fourier deconvolution, the original and deconvolved transmission spectra measured at the CONRAD-2 instrument for different steel samples are compared in **Figure 6.6a**. The transmission spectra measured at the TBL are shown for guidance as well. The original spectra resolve the position of the broad Bragg edges, where the effect of the different fractures of bcc and fcc phases cannot be clearly identified. However, the enhancement of the wavelength resolution using the deconvolution technique provides the information that the sample material consists of two crystallographic phases. Thus, the obtained Bragg edge from the deconvolution spectra at around 4.16 Å are now matching with the data from the TBL instrument measurements as displayed in **Figure 6.6**. The effect of the Fourier self-deconvolution does not change the position of the Bragg edges and does not change the Bragg edge shape but increases the wavelength resolution. The main advantage of the Fourier self-deconvolution is to reduce precisely the widths of individual bands (FWHM) without affecting the position or the total band area.

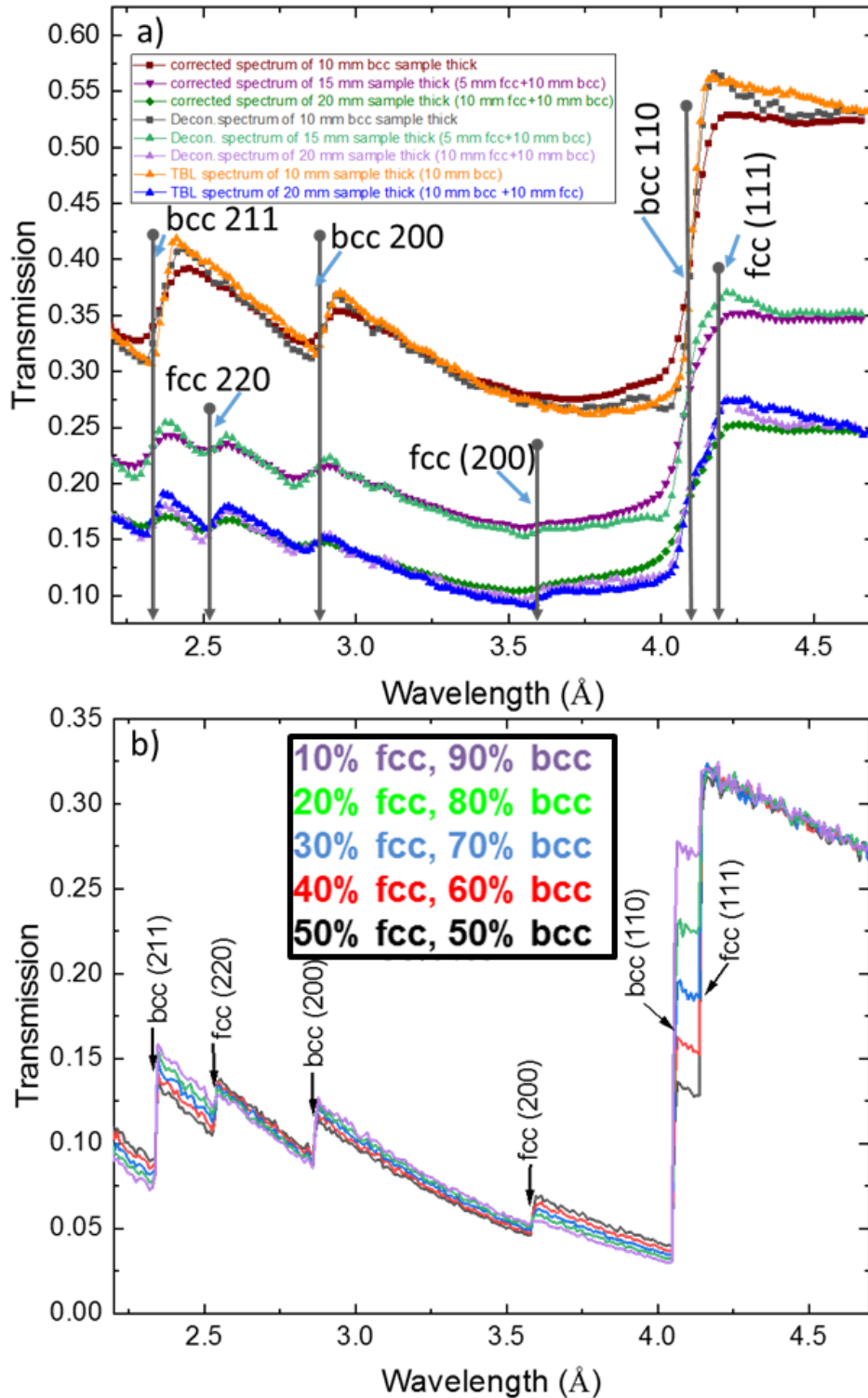


Figure 6.6. a) Comparisons between deconvolution spectrum of the CONRAD-2 instrument and both TBL transmission spectrums of high resolution mode at 10 mm and 20 mm thickness of steel and corrected CONRAD-2 spectrums at 10 mm, 15 mm and 20 mm thickness at a different steel structure. b) Simulation Bragg edge spectrum for a 20 mm steel thick of the bcc and fcc phases at a different percentage of steel phases.

In order to clarify the steel transmission spectra of both the bcc phase and the fcc phases, simulations of the Bragg edges for steel sample with 20 mm thickness is performed by using a McStas software [57] as shown in **Figure 6.6b**. The positions of the double phase Bragg edges for different phase fractions are clearly identified as well as the small shift in the Bragg edge position at around 4.2 Å.

The simulation results for the two phases steel mixtures agree well with the experimental data which allows for a microstructure analysis related to local disorientations and textures [23, 62].

Finally, we would like to emphasize that this deconvolution technique is generally applicable to any spectrum for improving its information content. The implemented approach to adjust the parameters of apodization and deconvolution function is convenient for the user and saves time.

6.4 Conclusions

Deconvolution technique for enhancing the wavelength resolution in transmission spectroscopy experiments at continuous neutron sources using double-crystal monochromator devices is proposed. This technique is very useful for microstructural analysis based on a Bragg edge spectroscopy.

7 Investigation and correction of detector backlighting effects in transmission imaging experiments

In this section, we study the backlight scattering also called “back illumination” in neutron imaging. In the detection system, this can affect significantly the quantification of attenuation coefficients and can lead to severe errors and image artifacts. Therefore, correction such backlighting effects would be desirable. In this study, the backlighting effects in neutron imaging experiments are investigated by varying the illuminated detector area and the magnitude of the attenuation. The attenuation coefficients of multiple metal plates are determined by polychromatic neutrons at the CONRAD-2 instrument. In addition, in section 6.2, we present a newly developed algorithm for correction of detector backlighting based on a simplified theoretical model.

7.1 Investigation of detector backlighting effects

Note: The following parts will be submitted to a scientific Journal, Authors: Ala’a M. Al-Falahat, Nikolay Kardjilov, Henning Markötter and Ingo Manke

7.1.1 Technical details

In order to investigate the observed effect systematically, we performed an attenuation experiment at the cold neutron radiography (CONRAD-2) instrument.

The neutron detector used at HZB consisted of a Li_6F scintillator screen of 10 μm thickness, which converts the transmitted neutrons into visible light and an optical CCD camera with an objective lens. The effective pixel size in the presented data was 55 μm , resulting in an $11.2 \times 11.2 \text{ cm}^2$ field of view (FOV).

7.1.2 Variation of the detector coverage:

The so-called detector backlighting effect is investigated with a standard neutron imaging detector [63]. When the neutron beam is almost totally absorbed by a sample, there is still a measurement signal behind the sample, because of the backlighting effect.

In order to investigate the backlight effect systematically for neutron transmission radiography with full polychromatic cold neutron spectrum, a standard detector configuration was chosen as shown in the schematic drawing in **Figure 7.1**. A cadmium plate of 10 cm x 6 cm (length x width) at a constant thickness of 0.5 mm was selected for this purpose. The thickness was chosen in a way

that almost the whole beam is attenuated except for a very small part of about 0.6% (simulating the case of an extremely strong absorbing sample).

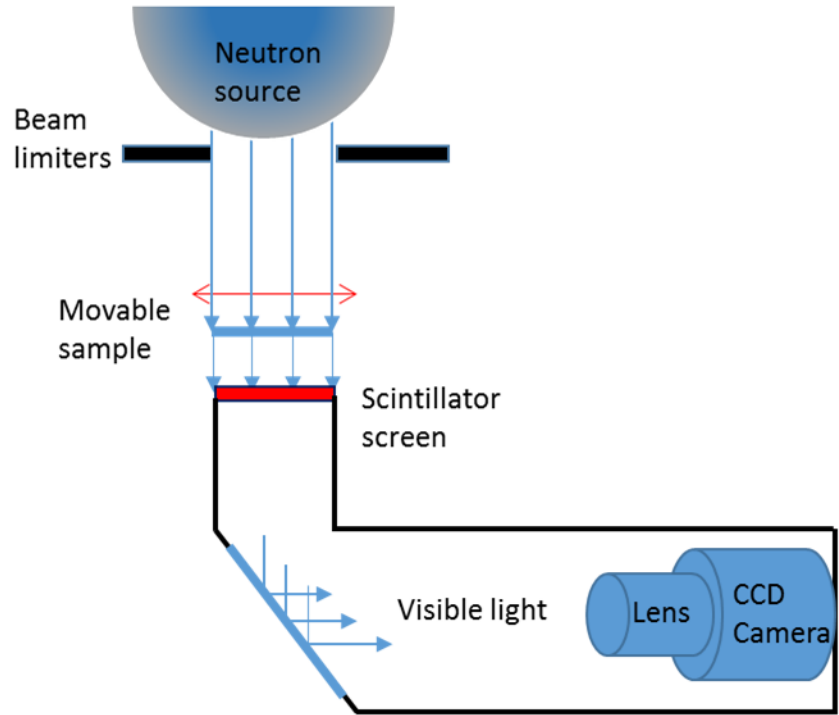


Figure 7.1. Experimental setup geometry for neutron radiography.

A series of neutron imaging measurements were performed, where a sample of cadmium (Cd) was moved stepwise from full coverage of the limited detector area to the completely flat field (without sample) through the movable stage. The changes of the transmitted intensities were analyzed in order to investigate the effect of the detector backlighting on the attenuation coefficient of the selected sample.

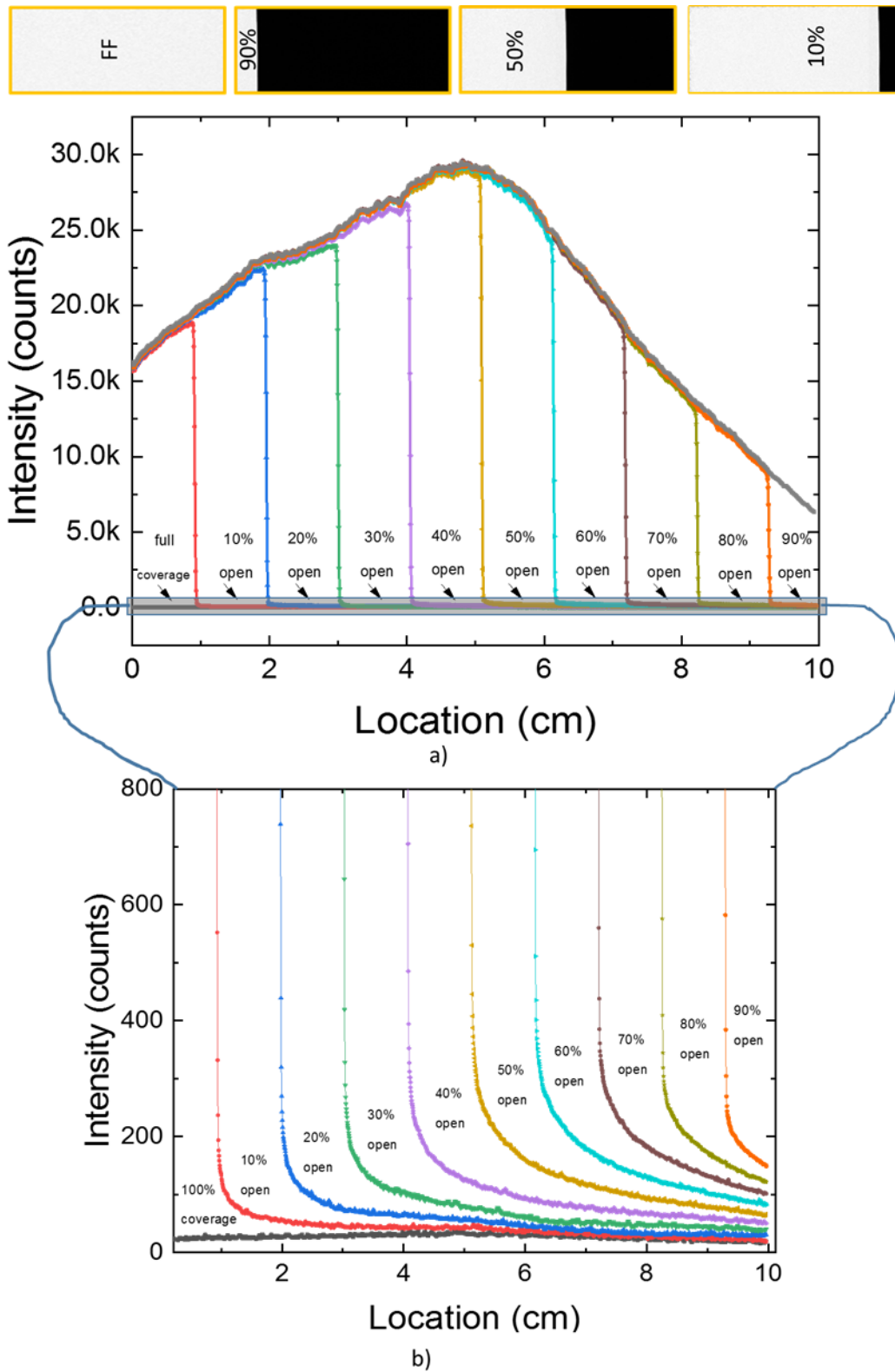


Figure 7.2. Line profiles taken from open beam neutron radiography images at different detector coverages (from 10% to fully coverage i.e. 100%) by a 0.5 mm thick cadmium plate. The numbers given in a) refer to the flat field (FF) intensity after dark field correction, in b) to the intensity attenuated by the cadmium plate.

The intensity of cadmium plates was measured by the detector at different positions of the plate. In **Figure 7.2**, the line profiles through the radiographic projection images taken at different coverages with a cadmium plate are shown. Coverages (percentage of covered area) were changed from 10% to 90% with steps of 10%. The measured intensity values in the open beam areas are not constant but depend on the detector coverage and on the distance to the covered area as shown in **Figure 7.2a**.

The area covered by cadmium is also affected. The intensity attenuated by the sample is reduced gradually by increasing the detector coverage area as shown in **Figure 7.2b**. *e.g.* from about 180 to 16 counts at 10% and 90%, respectively, after dark field correction.

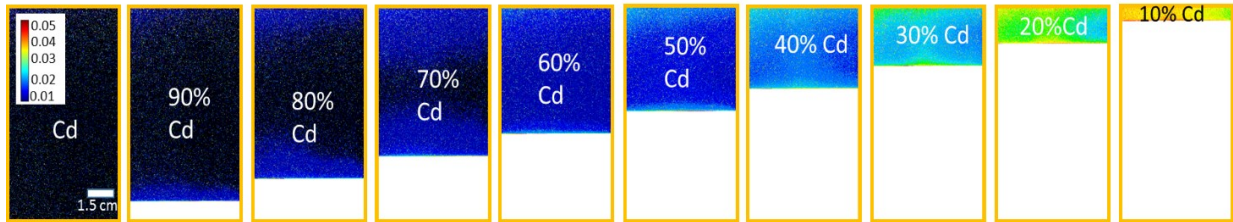


Figure 7.3. Color maps of the beam intensity distributions in the areas covered by a cadmium plate (Cd) as a function of detector coverage. The intensity values are given in fractions of the open beam at the corresponding area, i.e. after open beam normalization.

Figure 7.3 shows effect of backillumination in the neutron radiographic images for the different detector coverages (from full detector coverage to 10%) in the area covered by the Cd plate by using a color map and after normalization with the open beam. The spatial distribution of the measured intensity is not uniform but shows some increased intensity at both edges, close to the illuminated area and on the opposite edge.

Commonly used flat field and dark field corrections do not take into account such effects, leading to data misinterpretation of the sample.

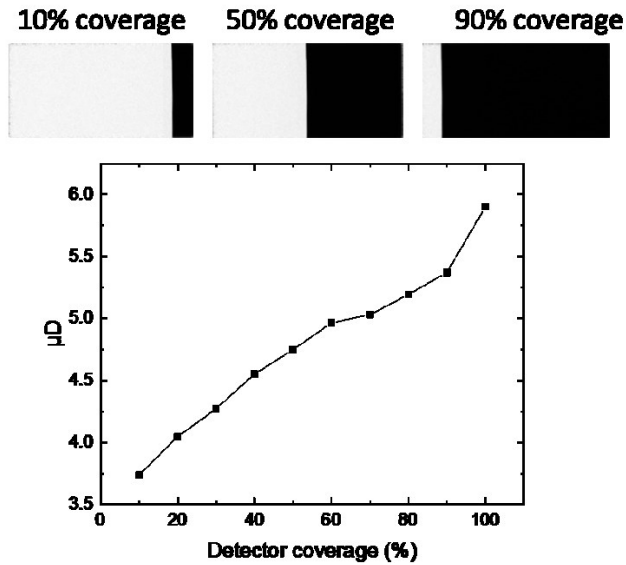


Figure 7.4. Discrepancies of the conventional exponential law in polychromatic neutron radiography; top radiographs of 0.5 mm cadmium plate at different detector coverage (here: 10, 50 and 90%, from left to right); bottom plot of average non-constant cross sections as a function of detector coverage.

From the measurements, the attenuation values of the 0.5 mm cadmium plate were calculated using the standard corrections for dark and flat field. The results are shown in **Figure 7.4** for different detector coverages. At a thickness $D = 0.5$ mm, the theoretical attenuation coefficient $\mu_{Cd}(2.95\text{\AA})=120.1\text{ cm}^{-1}$ [104] results in $\mu D = 6.005$. However, in order to exclude most pure edge effect contributions, the sum of the average transmission values over the whole covered areas were taken (excluding the area very close to the edges).

Apparently, the average attenuation coefficients (μ) at a constant thickness (as calculated from the intensity values) increase with the gradual closing of the beam due to the reduced backlighting signal. The observed variations – if not corrected – would lead to results not in agreement with the Lambert-Beer's law because the values for the attenuation coefficients depend on the actual detector coverage. The largest observed relative difference amounts to approximately 36.7% compared to the expected theoretically calculated value. The effect that causes this observed variation indicated by different values of attenuation for constant plate thickness and material is referred to as detector backlighting (although other effects cannot be excluded completely).

7.1.3 Variation of the penetrated thickness

Next, we have investigated the effect of different sample thicknesses at two different detector coverages on the attenuation values. For this purpose, 3 mm thick fcc phase (Fe-austenite) stainless steel plates (with dimensions 6 cm x 5 cm) were used and the attenuation gradually increased by the number of plates from 1 to 6, *i.e.*, increasing the overall sample thickness. By means of the beam limiter, the field of view was adjusted to the sample size.

The attenuation coefficient of steel ($Z=26$, $\rho=7.8$ g/cm³) at wavelength 2.9 Å is $\mu_{Fe}= 1.18$ cm⁻¹. [58]. This results in an attenuation of $\exp(-0.3543) = 0.702 = \exp(-\mu D)_0$ per single plate. By increasing the number of plates, a linear dependence $N^*(\mu D)_0$ is to be expected in theory if no other effect than absorption is taken into account.

7.1.3.1 Full detector coverage

In the first part of the experiment, the steel plate covered the entire active detector area as shown in **Figure 7.5a**. The red graph in **Figure 7.5c** shows the measured attenuation μD . The blue graph shows the theoretical values for neutrons at a wavelength of 2.9 Å (in case of an ideal monochromatic beam, what is an approximation to the polychromatic beam used for these experiments). The measured μD values are starting at about the same value as the calculated graph at $\mu D=0.356$. However, for increasing thickness, the values become smaller than in the calculated graph, mostly because of beam hardening due to the use of a polychromatic neutron beam which is discussed and corrected in many other works *e.g.* [105, 106]. Beam hardening causes the value to be at $\mu D = 1.99$ for 18 mm steel thickness (6 layers), compared to $\mu D = 2.13$ for the graph calculated for a single wavelength, *i.e.* for a monochromatic neutron beam with 2.9 Å. This is a difference of 7 %. Note: In the case of monochromatic synchrotron X-ray radiation such a difference was not reported by Lange *et al.* [107] as to be expected.

7.1.3.2 Partial detector coverage

In the second part of the experiment, the plate was covering only a part of the active detector area leaving the outside margin fully exposed to the neutron beam (see **Figure 7.5b**). The black graph in **Figure 7.5c** shows the obtained μD values for the covered area (black). These values differ from the values of the red graph (for the experiment with full detector coverage). The difference between the measured (μD) and the true (μD)₀ value increases as a function of the absorber thickness. The

maximum reduction is found to be approximately 6%. This is caused mainly by backlighting effects (in addition to other possible effects like e.g. neutron scattering at the sample edges that cannot be excluded). The additional light scattered into the covered area “reduces” the found μD values.

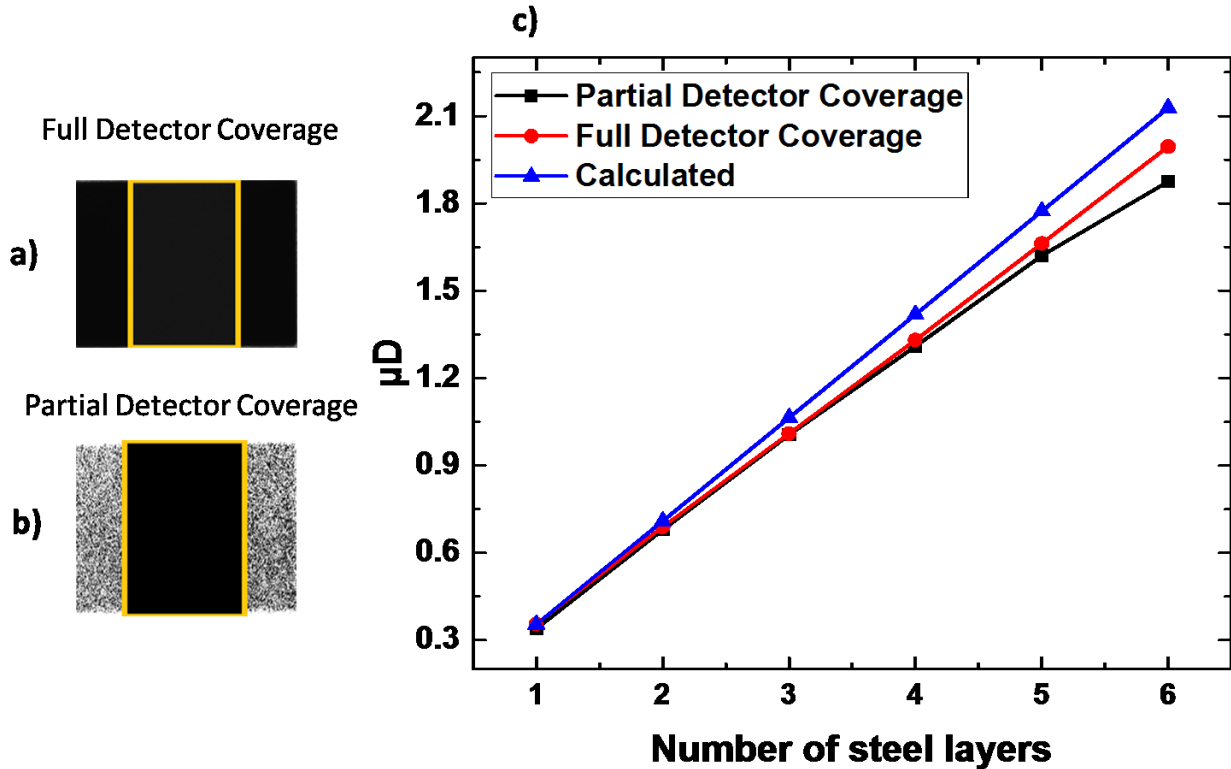


Figure 7.5. a) Full stainless steel coverage (length x width=5x6 cm²) of the detector area. b) Partial detector coverage with stainless steel. c) From the measured intensity values within the yellow marked areas in a) and b) calculated μD values. Attenuation coefficient as a function of the number of steel layers at full detector coverage (red line). Significant deviations from the linear attenuation as a function of steel layers are visible in case of partial detector coverage (black line). Theoretical results are calculated by nxsPlotter [58] of fcc stainless steel as a function of steel thickness (blue line). The difference between the red and blue curve is mainly due to beam hardening and the polychromatic neutron spectrum not taken into account in the calculated graph.

From the obtained results, we conclude that the normalized images have a non-uniform distribution of the intensity as a function of covered and open beam area. This is mostly due to the backlight effect which gives false values for the attenuation coefficients and therefore wrong normalization results and a nonlinear relationship between the attention coefficients and the material thickness that makes the quantitative interpretation of images very challenging. This is especially the case for tomographic imaging where a measured sample causes different detector coverages during rotation depending on the size and shape of the sample. This results in deviations from the true μD

values in every single tomographic projection image that hampers quantification of 3D images and may even cause artifacts.

7.1.4 Summary of investigation of the Backlighting effect

We have shown that backlighting effects can strongly affect the quantification of neutron imaging data. Especially for highly absorbing materials, the effect can be very strong, causing measurement errors of the attenuation coefficient from a few to over 10%. The effect increases with decreasing detector coverages. Furthermore, we have shown that commonly used procedures for flat field and dark field corrections (Eq.(1.2)) are not always sufficient because both signals depend on the actual detector coverage by the sample and on the location. In general, it can be expected, that the backlighting effect strongly depends on the used imaging detection system and scintillator and can be much different in other systems. With upcoming improved quantification in neutron imaging experiments backlighting has to be taken into consideration in data analysis in future. Our results are also important for X-ray imaging experiments at lab and synchrotron sources where highly accurate data quantification are key issues in many research fields, like *e.g.* for quantification of water [108-110] or other liquid media [4, 111, 112] in fuel cells or batteries [113-115] and for quantitative segmentation [116-118] in tomographic imaging in general. In addition, this effect might be important even in many other fields where similar 2D detector systems are used [119-122]. Next step could be the development of correction algorithms for backlighting effects [123]. The final goal is to reach the precision of radiometry (usually performed with photon counting single channel detectors) for imaging systems.

7.2 Correction approach of detector backlighting in radiography

The following parts have been submitted to the “Review of Scientific Instruments”,
Authors: Ala’a M. Al-Falahat, Andreas Kupsch, Manfred P. Hentschel, Axel Lange,
Nikolay Kardjilov, Henning Markötter, and Ingo Manke

7.2.1 Backlighting model

When radiation of intensity I_p enters a detector it is considered that due to scattering a backlight factor α will cause an additional intensity at the incident positions proportional to I_p and resulting in a registered intensity $I_0 = (1+\alpha) I_p$. Such an approach was taken for an empirical correction of backlighting of X-ray detectors by Lange *et. al.* [124-126] using redistribution of an intensity fraction throughout all the active detector area. Although substantial improvements of X-ray radiographs were reported, no proof of the correction procedure has been provided up to now. A critical investigation and improvements are to be discussed in the following.

For the sake of illustration, the relevant intensity terms related to the background intensity generation and correction are schematically shown in **Figure 7.6**. I_p is the (true) source intensity and I_t the (true) sample transmission intensity. The backlighting factor α is a uniform measure of the isotropic scattering of the incident radiation at all detector locations, and specific for a selected detector. If the measured detector intensity I_0 is used for reference at full detector illumination then the primary source intensity I_p can be written as

$$I_p = \frac{I_0}{1 + \alpha}, \quad (7.1)$$

The detector coverage c represents the detector area covered by the sample cross section. It is a value between 0 for no coverage (no sample) and 1 for full coverage (large sample). As shown by **Figure 7.6**, the fraction α is assumed to be identical at all excitation position. It refers to measurements with sample and without (flat field), accordingly. In an earlier rather empirical approach to reveal corrected attenuation values $(\mu D)_{corr}$, both images are corrected by subtracting the weighted average intensities due to the backlight scattering, resulting in corrected intensities $I_{0\ corr}$ and I_{corr} [16, 17, 123]

$$(\mu D)_{corr} = \ln \left(\frac{I_{0\ corr}}{I_{corr}} \right) = \ln \left(\frac{I_0(r) - \alpha \bar{I}_0}{I(r) - \alpha \bar{I}} \right), \quad (7.2)$$

where $I_0(r)$ is the detected intensity without sample at all detector positions r and \bar{I}_0 its average. $I(r)$ is the local intensity with sample and \bar{I} is the intensity with sample averaged over the open detector area and the section covered by the sample. Beyond the requirement of isotropic scattering, the idealized scenario implies long range scattering within detector dimensions. Furthermore, parallel beam conditions of the source are assumed.

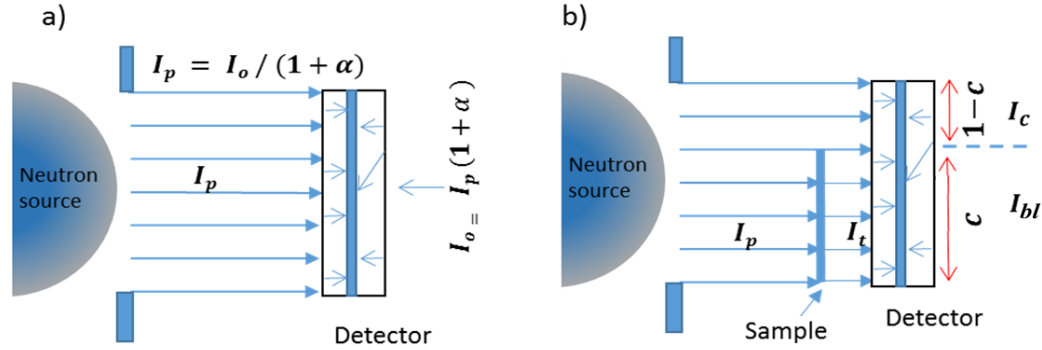


Figure 7.6. Illustration of the backlighting effect of the detector based on the source intensity I_p from an idealized parallel beam; a) open detector intensity I_0 without sample; b) intensities as a function of detector coverage c : the open detector intensity including backlighting I_c , the theoretical intensity I_t after transmission of the sample and the observed intensity I_{bl} with backlighting.

7.2.2 Determination of backlight factor

The backlight factor α is required for modelling the modified partial intensities and their correction. It may be determined by a virtual slit experiment according to **Figure 7.6** with a fully absorbing sample defining a slit in a diaphragm. A variable (relative) detector coverage c , corresponding to a slit opening $(1-c)$ and at given α the detector intensity I_c in the open slit range will be

$$I_c = I_p (1 + \alpha (1 - c)) \quad (7.3)$$

From the measurable intensities I_c at two different detector coverages c_1 and c_2 and rearranged Eq. (7.3) the backlight factor α is available:

$$\alpha = \frac{(I_{c1} - I_{c2})}{I_{c2}(1 - c_1) - I_{c1}(1 - c_2)} \quad (7.4)$$

For a chosen factor $\alpha = 0.1$, **Figure 7.7** shows the expected intensities I_c over c according to Eq. (7.3) and the source intensity I_p . For convenience, at $c = 0$, the detector intensity without coverage

is $I_0 = 1$. At closed slit, the extrapolated (virtual) intensity level corresponds to I_p . According to the discussed scenario, the backlight factor α of a specific detector depends on the investigated samples.

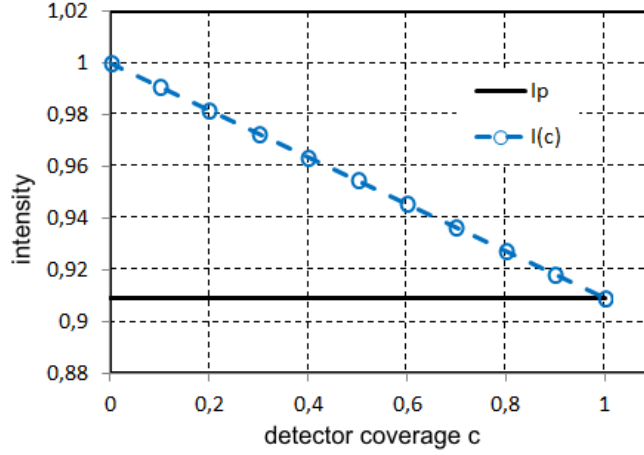


Figure 7.7. Detector Intensities I_c within slit as a function of coverage c (Eq. (7.3)), backlight factor $\alpha = 0.1$ source intensity I_p

7.2.3 Modeling of backlighting intensity

In the following section, the backlighting behavior is considered regarded assuming two different backlighting factors α in dependence of the detector coverage c . For convenience, a homogeneous sample of constant wall thickness $D=1$ and attenuation is chosen. The measurable intensity I_c in the fully irradiated section $(1-c)$ of **Figure 7.6b** is the sum of the primary beam I_p and the intensity due to backlighting of the illuminated detector section αI_p . For reference $I_0 = 1$ is set.

According to Eq. (1.2), the correct sample transmission intensity (**Figure 7.6b**, covered section) is denoted by

$$I_t = I_p \exp(-\mu D) \tag{7.5}$$

Based on I_t , the modified intensity I_{bl} due to backlighting is composed of the transmission of the sample I_t and the backlight intensities from the open beam part $\alpha I_p (1 - c)$ and from the covered detector part $\alpha I_t c$

$$I_{bl} = I_t + \alpha (I_t c + I_p (1 - c)) = I_t (1 + \alpha c) + \alpha I_p (1 - c) \tag{7.6}$$

In case of full detector coverage $c_1 = 1$ by a sample and with Eq. (7.1) I_{bl} becomes

$$I_{bl}(c_1) = (1 + \alpha) I_t = I_0 \exp(-\mu D), \tag{7.7}$$

which characterizes an experiment providing the correct μD by an experimental I_0 regardless of backlighting as required by Eq. (1.2).

Some examples of modified transmission intensities I_{bl} are plotted in **Figure 7.8** as a function of detector coverage c for two selected transmissions $0.2 I_p$ and $0.5 I_p$ and at backlight factors 0.02 and 0.1. The intensity deviations above the I_t references due to backlighting are stronger for small transmission and for high α and always decrease over detector coverage c . The simulated intensities might be of practical meaning, as the backlight factors are chosen within the range of reported X-ray investigations of 2.8 % from a 60 kV polychromatic laboratory fluorescent screen system and of $\alpha = 10.5$ % for a transparent CdWO_4 single crystal screen at 15 keV [123].

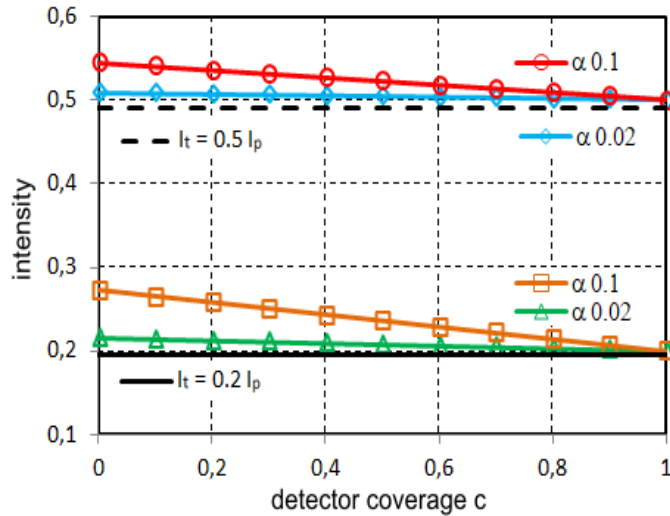


Figure 7.8. Examples of modified transmission intensities I_{bl} over detector coverage c referring to correct transmissions $I_t = 0.2$ and $I_t = 0.5$ at backlight factors 0.02 and 0.1.

In order to regard the attenuation $(\mu D)_{bl}$ with backlighting, the intensity I_{cs} in the open detector section is needed. It stands for the experimental reference of the primary beam intensity. I_{cs} is the analogue to I_c in Eq. (7.3) supplemented with the backlight contribution from the covered region c (see **Figure 7.6**):

$$I_{cs} = I_p(1 + \alpha(1 - c)) + \alpha I_t c \quad (7.8)$$

The attenuation $(\mu D)_{bl}$ with backlighting effect is then derived from Eqs. (7.6) and (7.8):

$$(\mu D)_{bl} = \ln \left(\frac{I_{cs}}{I_{bl}} \right) = \ln \left(\frac{I_p(1 + \alpha(1 - c)) + \alpha I_t c}{I_t + \alpha I_t c + \alpha I_p(1 - c)} \right) \quad (7.9)$$

For demonstrating examples of $(\mu D)_{bl}$ with backlighting, the above transmission intensities I_{bl} (of **Figure 7.8**) and the expected I_{cs} of the open beam are introduced into Eq. (7.9) and plotted in **Figure 7.9**. The indicated reference levels μD_1 and μD_2 (black line) refer to the transmission intensities $I_t = 0.2 I_p$ and $I_t = 0.5 I_p$ respectively.

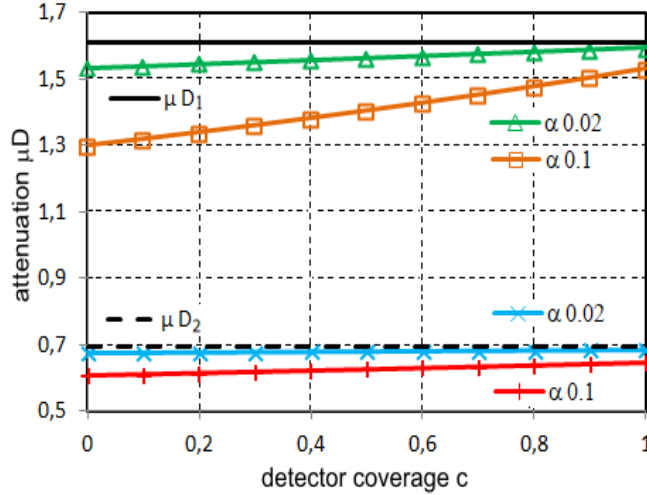


Figure 7.9. Examples of $(\mu D)_{bl}$ with backlighting based on the above transmission intensities I_{bl} of Figure 7.8 according to Eq. (7.9) demonstrating considerable deviations from the correct reference levels μD_1 and μD_2 (black lines).

The deviations decrease with increasing coverage but they increase with higher attenuation and of course at higher backlight factor. **Figure 7.9** shows even a small $(\mu D)_{bl}$ deviation at full detector coverage. This is due to the use of the intensity I_{cs} in Eq. (7.9) instead of I_0 which would give the true value according to Eq. (7.7). However, in radiography I_{cs} is commonly taken for the open beam intensity.

7.2.4 Correction of backlighting effects

The considerable high deviations of the modelled attenuations by detector backlighting require correction. In order to eliminate the effect of backlighting at given α for all detector coverages, the correction procedure should rely solely on the intensities I_{bl} and I_0 which would be experimentally accessible. By definition, the true μD values are provided by I_t and I_p according to Eq. (7.5). The sample transmission intensity I_t from Eqs (7.6) and (7.1) is

$$I_t = \frac{1}{1 + \alpha c} \left(I_{bl} - \alpha I_0 \frac{1-c}{1+\alpha} \right) \quad (7.10)$$

The exactly corrected attenuation coefficient is then

$$(\mu D)_{\text{excorr}} = \ln \left(\frac{I_p}{I_t} \right) = \ln \left(\frac{I_0/(1+\alpha)}{\frac{1}{1+\alpha c} (I_{bl} - \frac{\alpha}{1+\alpha} I_0 (1-c))} \right) = \ln \left(\frac{I_0(1+\alpha c)}{(1+\alpha) I_{bl} - \alpha I_0 (1-c)} \right) \quad (7.11)$$

A comparison of Eq. (7.11) with the former empirical formula Eq. (7.2) is drawn by substituting \bar{I}_0 and \bar{I} . From **Figure 7.6** and Eq. (7.1) the average intensity with a sample is

$$\bar{I} = I_{bl} c + I_c(1 - c) \quad (7.12)$$

From Eqs (7.2) and (7.12) the corrected attenuation follows by

$$(\mu D)_{\text{corr}} = \ln \left(\frac{I_0(r) - \alpha \bar{I}_0}{I(r) - \alpha \bar{I}} \right) = \ln \left(\frac{I_0(1-\alpha)}{I_{bl} - \alpha (c I_{bl} + I_c(1-c))} \right), \quad (7.13)$$

when I_{bl} replaces $I(r)$ and $I_0(r)$ is a constant I_0 . With the approximations $(1-\alpha) \cong 1/(1+\alpha)$ and the expansion of the fraction with $(1+\alpha)(1+\alpha c)$ it follows

$$(\mu D)_{\text{corr}} = \ln \left(\frac{I_0(1+\alpha c)}{(I_{bl}(1-\alpha c)(1+\alpha) - I_0 \alpha (1-c)(1+\alpha(1-c))}(1+\alpha c)} \right), \quad (7.14)$$

and with the further approximations $\alpha^2 \cong 0$ and $\alpha^3 \cong 0$ then

$$(\mu D)_{\text{corr}} \cong \ln \left(\frac{I_0(1+\alpha c)}{(1+\alpha) I_{bl} - \alpha I_0(1-c)} \right), \quad (7.15)$$

which is equal to $(\mu D)_{\text{excorr}}$ in Eq. (7.11). Thus Eq. (7.13) should be a good approximation of Eq. (7.11), regarding all higher order terms of α as sufficiently small.

A numerical test of the currently modelled parameters via Eq. (7.13) reveals a residual mismatch of up to 4 % for low sample coverage at the high attenuation case. But at 50 % transmission, the deviations do not exceed 1 %. Finally, the approximations determine generally the validity range of Eq. (7.1) to compare well with common noise levels in radiography.

For the current model of homogenous flat samples the new correction formula of Eq. (7.11) provides clearly higher precision than the earlier empirical approach of $(\mu D)_{\text{corr}}$ (Eq. (7.2)). The numerical test of the $(\mu D)_{\text{excorr}}$ reveals precisely the attenuation input for all parameters considered. However, the application of Eq. (7.1) does not require the determination of the sample coverage and may be more suitable for experimental requirements. It reduces the backlighting deficiencies always by an order of magnitude.

As backlighting deficiencies strongly depend on the actually used imaging detector system, they become especially relevant in case of new detector installations regarding scintillators or optics and when high radiometric precision is required.

7.2.5 Summary and conclusions of the correction of the backlighting effect

Based on the concept of backlighting in radiography due to long-range isotropic scattering within the irradiated detector volume, an algorithm for the correction of deficient transmission images is derived by modelling the backlighting details of partial intensities defined by the detector coverage of sample projections. A straightforward procedure is given to determine the backlighting factor that provides a measure for the strength of the effects due to the detector scattering properties. The deviations from correct attenuation coefficients depending on the backlighting factor, the sample transmission and the detector coverage of samples are modelled. At usual radiography conditions, backlighting is found to strongly affect materials attenuation data up to some 10%. A former correction approach of practical advantages has been verified to be well suitable and an exact procedure of higher precision has been obtained. The presented scenario is specific to the incident cross section on the detector and limited to long-range scattering. It is universal with reference to the physical nature of backlighting in radiation imaging. The given procedures may be useful for all kind of imaging detectors beyond radiography in general.

8 Summary

An overview on neutron imaging is given in the beginning of this work. Neutron imaging is a highly versatile technique that is used in the field of engineering science and technology. The basic principle of making images with neutron is described. The attenuation μ is described by the Beer-Lambert law to the neutrons that are transmitted through the sample reach the detector in ideal experimental conditions. Moreover, attenuation-based neutron imaging allows in some cases changing the material contrast in radiographic images due to wavelength-dependent attenuation properties of materials.

The basic principle of the setups for neutron imaging instruments used within this thesis is presented in chapter two. In addition, a virtual model of the instruments was implemented using Monte-Carlo ray-tracing simulation based on McStas software package. It is used to compute the performance of instruments, optimize the existing instrumentation and compare the results with real experiments. A virtual instrument detail was presented in chapter three.

The principal interaction of neutrons with matter is discussed in chapter four where the total microscopic cross-section of the crystalline materials is quantitatively determined by its coherent and incoherent scattering as well as absorption contributions. The difference between coherent and incoherent scattering was quantitatively described included elastic and inelastic scattering for both types of scattering. This calculation based on the nxsPlotter software allows us to study neutron scattering from the crystal lattice with thermal motion by calculation of the effect of the Debye-Waller factor on the total neutron cross section.

In order to experimentally investigate the thermal effect on the total neutron cross section, wavelength selective neutron imaging was performed. The transmission spectrum shows significant variations of the Bragg edge height as a function of sample temperature. It was found that the decrease of the Bragg edge after increase of the temperature to 500 °C is only referred to the Debye Waller factor. In addition to these basic experiments, phase transformations in selected metals i.e. martensitic steels was investigated at high temperatures.

Given the results described in chapter five we can confirm that the Monte Carlo simulations of the double-crystal monochromator which is one of main components in the CONRAD-2 instrument provide sufficient information of the performance of the double-crystal monochromator in terms

of crystals mosaicity and a wavelength gradient of the neutron beam. The results achieved in this study was obtained of about 0.005 Å/cm wavelength gradient caused by crystal mosaicity at the sample position and the wavelength resolution gets worse with increasing crystal mosaicity. The comparison between simulated and measured of the wavelength gradient was obtained in a good agreement. In addition, the wavelength gradient can be exploited to obtain spectroscopic information of a sample providing a new energy-selective neutron imaging method as described in chapter five section 1.2.

In chapter six, it is shown how the wavelength resolution of the spectra taken at the CONRAD-2 instrument using the double-crystal monochromator could be enhanced by about a factor of three by applying a Fourier self-deconvolution procedure. The results are compared with results from the ESS Test beamline (V20), which provides a much better resolution than the double-crystal monochromator at CONRAD-2.

In chapter seven, it is shown that the commonly used procedures for flat field and dark field corrections are not always sufficient because both signals depend on the actual detector coverage by the sample. Therefore, the quantification accuracy of neutron radiography was studied by investigated the detector backlighting effects caused e.g. by scattered light within the irradiated detector area that yield inaccurate quantification of attenuation coefficients. This effect was studied in detail by changing the detector coverage area and the magnitude of the attenuation. As a result, the backlighting effect is increased with decreasing the detector coverages area, causing measurement errors of the attenuation coefficient from a few to over 10%. However, an algorithm for a first order correction of detector backlighting based on a simple theoretical model was developed as shown in chapter seven section 2. According to this model, a backlighting factor was introduced that provides a measure for the strength of the backlighting effect depending on the detector coverage by the sample projection and the remaining full beam section. Therefore, a straightforward procedure was applied to correct the attenuation coefficients depending on the backlighting factor.

List of references

- [1] P. Boillat, J. Biesdorf, P. Oberholzer, A. Kaestner, T.J. Schmidt, Evaluation of Neutron Imaging for Measuring Phosphoric Acid Distribution in High Temperature PEFCs, *Journal of The Electrochemical Society*, 161 (2014) F192-F198.
- [2] A. Schröder, K. Wippermann, J. Mergel, W. Lehnert, D. Stolten, T. Sanders, T. Baumhöfer, D.U. Sauer, I. Manke, N. Kardjilov, A. Hilger, J. Schloesser, J. Banhart, C. Hartnig, Combined local current distribution measurements and high resolution neutron radiography of operating Direct Methanol Fuel Cells, *Electrochemistry Communications*, 11 (2009) 1606-1609.
- [3] A. Schröder, K. Wippermann, W. Lehnert, D. Stolten, T. Sanders, T. Baumhöfer, N. Kardjilov, A. Hilger, J. Banhart, I. Manke, The influence of gas diffusion layer wettability on direct methanol fuel cell performance: A combined local current distribution and high resolution neutron radiography study, *Journal of Power Sources*, 195 (2010) 4765-4771.
- [4] W. Maier, T. Arlt, K. Wippermann, C. Wannek, I. Manke, W. Lehnert, D. Stolten, Correlation of Synchrotron X-ray Radiography and Electrochemical Impedance Spectroscopy for the Investigation of HT-PEFCs, *Journal of The Electrochemical Society*, 159 (2012) F398-F404.
- [5] J.P. Owejan, J.J. Gagliardo, S.J. Harris, H. Wang, D.S. Hussey, D.L. Jacobson, Direct measurement of lithium transport in graphite electrodes using neutrons, *Electrochimica Acta*, 66 (2012) 94-99.
- [6] A. Senyshyn, M.J. Muehlbauer, O. Dolotko, M. Hofmann, T. Pirling, H. Ehrenberg, Spatially resolved in operando neutron scattering studies on Li-ion batteries, *Journal of Power Sources*, 245 (2014) 678-683.
- [7] C. Totzke, I. Manke, A. Hilger, G. Choinka, N. Kardjilov, T. Arlt, H. Markotter, A. Schroder, K. Wippermann, D. Stolten, C. Hartnig, P. Kruger, R. Kuhn, J. Banhart, Large area high resolution neutron imaging detector for fuel cell research, *Journal of Power Sources*, 196 (2011) 4631-4637.
- [8] M.A. Hickner, N.P. Siegel, K.S. Chen, D.S. Hussey, D.L. Jacobson, M. Arif, In Situ High-Resolution Neutron Radiography of Cross-Sectional Liquid Water Profiles in Proton Exchange Membrane Fuel Cells, *Journal of The Electrochemical Society*, 155 (2008) B427-B434.
- [9] R. Kuhn, J. Scholta, P. Krueger, C. Hartnig, W. Lehnert, T. Arlt, I. Manke, Measuring device for synchrotron X-ray imaging and first results of high temperature polymer electrolyte membrane fuel cells, *Journal of Power Sources*, 196 (2011) 5231-5239.
- [10] N. Kardjilov, A. Hilger, I. Manke, M. Strobl, W. Treimer, J. Banhart, Industrial applications at the new cold neutron radiography and tomography facility of the HMI, *Nuclear Instruments and*

Methods in Physics Research Section A: Accelerators, Spectrometers, Detectors and Associated Equipment, 542 (2005) 16-21.

[11] D. Linden, T.B. Reddy, Handbook Of Batteries, in: L. D. (Ed.) Handbook Of Batteries, McGraw-Hill, New York,, 2002.

[12] R. Woracek, Energy selective neutron imaging for the characterization of polycrystalline materials, (2015).

[13] R. Woracek, D. Penumadu, N. Kardjilov, A. Hilger, M. Boin, J. Banhart, I. Manke, 3D Mapping of Crystallographic Phase Distribution using Energy-Selective Neutron Tomography, Advanced Materials, 26 (2014) 4069-4073.

[14] A.E. Craft, B.A. Hilton, G.C. Papaioannou, Characterization of a Neutron Beam Following Reconfiguration of the Neutron Radiography Reactor (NRAD) Core and Addition of New Fuel Elements, Nuclear Engineering and Technology, 48 (2016) 200-210.

[15] J. Banhart, Advanced tomographic methods in materials research and engineering, Oxford University Press2008.

[16] A.S. Tremsin, N. Kardjilov, M. Dawson, M. Strobl, I. Manke, J.B. McPhate, J.V. Vallerga, O.H.W. Siegmund, W.B. Feller, Scatter rejection in quantitative thermal and cold neutron imaging, Nuclear Instruments and Methods in Physics Research, Section A: Accelerators, Spectrometers, Detectors and Associated Equipment, 651 (2011) 145-148.

[17] R. Hassanein, E. Lehmann, P. Vontobel, Methods of scattering corrections for quantitative neutron radiography, Nuclear Instruments and Methods in Physics Research, Section A: Accelerators, Spectrometers, Detectors and Associated Equipment, 542 (2005) 353-360.

[18] S. Peetermans, R. van Langh, E. Lehmann, A. Pappot, Quantification of the material composition of historical copper alloys by means of neutron transmission measurements, Journal of Analytical Atomic Spectrometry, 27 (2012) 1674-1674.

[19] M. Raventos, R.P. Harti, E. Lehmann, C. Grünzweig, A Method for Neutron Scattering Quantification and Correction Applied to Neutron Imaging, Physics Procedia, 88 (2017) 275-281.

[20] W. Kockelmann, G. Frei, E.H. Lehmann, P. Vontobel, J.R. Santisteban, Energy-selective neutron transmission imaging at a pulsed source, Nuclear Instruments & Methods in Physics Research Section a-Accelerators Spectrometers Detectors and Associated Equipment, 578 (2007) 421-434.

- [21] V. Wagner, Z. Kouril, P. Lukas, P. Mikula, J. Saroun, P. Strunz, M. Vrana, Residual strain/stress analysis by means of energy-dispersive neutron transmission diffraction (EDNTD), 1997, pp. 168-171.
- [22] J.R. Santisteban, L. Edwards, M.E. Fitzpatrick, A. Steuwer, P.J. Withers, M.R. Daymond, M.W. Johnson, N. Rhodes, E.M. Schooneveld, Strain imaging by Bragg edge neutron transmission, Nucl Instrum Meth A, 481 (2002) 765-768.
- [23] J.R. Santisteban, L. Edwards, V. Stelmukh, Characterization of textured materials by TOF transmission, Physica B: Condensed Matter, 385-386 I (2006) 636-638.
- [24] J.R. Santisteban, M.A. Vicente-Alvarez, P. Vizcaino, A.D. Banchik, S.C. Vogel, A.S. Tremsin, J.V. Vallergera, J.B. McPhate, E. Lehmann, W. Kockelmann, Texture imaging of zirconium based components by total neutron cross-section experiments, Journal of Nuclear Materials, (2011).
- [25] K. Oikawa, Y.H. Su, Y. Tomota, T. Kawasaki, T. Shinohara, T. Kai, K. Hiroi, S.Y. Zhang, J.D. Parker, H. Sato, Y. Kiyonagi, A Comparative Study of the Crystallite Size and the Dislocation Density of Bent Steel Plates using Bragg-edge Transmission Imaging, TOF Neutron Diffraction and EBSD, Physics Procedia, 88 (2017) 34-41.
- [26] M. Boin, R.C. Wimpory, A. Hilger, N. Kardjilov, S.Y. Zhang, M. Strobl, Monte Carlo simulations for the analysis of texture and strain measured with Bragg edge neutron transmission, Journal of Physics: Conference Series, 340 (2012) 012022.
- [27] M. Strobl, C. Grünzweig, A. Hilger, I. Manke, N. Kardjilov, C. David, F. Pfeiffer, Neutron Dark-Field Tomography, Physical Review Letters, 101 (2008) 123902.
- [28] C. Grunzweig, C. David, O. Bunk, M. Dierolf, G. Frei, G. Kuhne, R. Schafer, S. Pofahl, H.M.R. Ronnow, F. Pfeiffer, Bulk magnetic domain structures visualized by neutron dark-field imaging, Applied Physics Letters, 93 (2008) 112504.
- [29] M. Strobl, General solution for quantitative dark-field contrast imaging with grating interferometers, Sci. Rep., 4 (2014).
- [30] J. Banhart, A. Borbely, K. Dzieciol, F. Garcia-Moreno, I. Manke, N. Kardjilov, A.R. Kaysser-Pyzalla, M. Strobl, W. Treimer, X-ray and neutron imaging - Complementary techniques for materials science and engineering, International Journal of Materials Research, 101 (2010) 1069-1079.
- [31] C. Grünzweig, C. David, O. Bunk, M. Dierolf, G. Frei, G. Kuhne, J. Kohlbrecher, R. Schafer, P. Lejcek, H.M.R. Ronnow, F. Pfeiffer, Neutron decoherence imaging for visualizing bulk magnetic domain structures, Physical Review Letters, 101 (2008).

- [32] N. Kardjilov, I. Manke, A. Hilger, S. Williams, M. Strobl, R. Woracek, M. Boin, E. Lehmann, D. Penumadu, J. Banhart, Neutron Bragg-edge mapping of weld seams, *International Journal of Materials Research*, 103 (2012) 151-154.
- [33] P. Trtik, J. Hovind, C. Grünzweig, A. Bollhalder, V. Thominet, C. David, A. Kaestner, E.H. Lehmann, Improving the spatial resolution of neutron imaging at Paul Scherrer Institut–The Neutron Microscope Project, *Physics Procedia*, 69 (2015) 169-176.
- [34] S.H. Williams, A. Hilger, N. Kardjilov, I. Manke, M. Strobl, P.A. Douissard, T. Martin, H. Rieseemeier, J. Banhart, Detection system for microimaging with neutrons, *Journal of Instrumentation*, 7 (2012) P02014.
- [35] E.H. Lehmann, G. Frei, G. Kuhne, P. Boillat, The micro-setup for neutron imaging: A major step forward to improve the spatial resolution, *Nuclear Instruments & Methods in Physics Research Section a-Accelerators Spectrometers Detectors and Associated Equipment*, 576 (2007) 389-396.
- [36] M.G. Makowska, M. Strobl, E.M. Lauridsen, S. Kabra, W. Kockelmann, A. Tremsin, H.L. Frandsen, L. Theil Kuhn, In situ time-of-flight neutron imaging of NiO–YSZ anode support reduction under influence of stress, *Journal of Applied Crystallography*, 49 (2016).
- [37] M.G. Makowska, M. Strobl, E.M. Lauridsen, H.L. Frandsen, A. Tremsin, T. Shinohara, L.T. Kuhn, Phase transition mapping by means of neutron imaging in SOFC anode supports during reduction under applied stress, *ECS Transactions*, 68 (2015) 1103-1114.
- [38] J. Santisteban, M. Vicente-Alvarez, P. Vizcaino, A. Banchik, S. Vogel, A. Tremsin, J. Vallergera, J. McPhate, E. Lehmann, W. Kockelmann, Texture imaging of zirconium based components by total neutron cross-section experiments, *Journal of Nuclear Materials*, 425 (2012) 218-227.
- [39] M. Dawson, I. Manke, N. Kardjilov, A. Hilger, M. Strobl, J. Banhart, Imaging with polarized neutrons, *New Journal of Physics*, 11 (2009) 043013.
- [40] I. Manke, C. Hartnig, M. Grunerbel, J. Kaczerowski, W. Lehnert, N. Kardjilov, A. Hilger, J. Banhart, W. Treimer, M. Strobl, Quasi--in situ neutron tomography on polymer electrolyte membrane fuel cell stacks, *Applied Physics Letters*, 90 (2007) 184101.
- [41] S.J. Lee, S.G. Kim, G.G. Park, C.S. Kim, Quantitative visualization of temporal water evolution in an operating polymer electrolyte fuel cell, *International Journal of Hydrogen Energy*, 35 (2010) 10457-10463.

- [42] I. Manke, N. Kardjilov, A. Hilger, M. Strobl, M. Dawson, J. Banhart, R. Schafer, G. Behr, C. Grunzweig, C. David, M. Hentschel, A. Kupsch, A. Lange, Three-dimensional imaging of magnetic domains, *Nature Communications*, 1 (2010).
- [43] M. Strobl, W. Treimer, P. Walter, S. Keil, I. Manke, Magnetic field induced differential neutron phase contrast imaging, *Applied Physics Letters*, 91 (2007) 254104.
- [44] L. Gondek, N.B. Selvaraj, J. Czub, H. Figiel, D. Chapelle, N. Kardjilov, A. Hilger, I. Manke, Imaging of an operating LaNi_{4.8}Al_{0.2}-based hydrogen storage container, *International Journal of Hydrogen Energy*, 36 (2011) 9751-9757.
- [45] I. Manke, N. Kardjilov, M. Strobl, A. Hilger, J. Banhart, Investigation of the skin effect in the bulk of electrical conductors with spin-polarized neutron radiography, *Journal of Applied Physics*, 104 (2008) 076109.
- [46] A. Hilger, I. Manke, N. Kardjilov, M. Osenberg, H. Markötter, J. Banhart, Tensorial neutron tomography of three-dimensional magnetic vector fields in bulk materials, *Nature Communications*, 9 (2018) 4023.
- [47] I. Manke, H. Markotter, C. Totzke, N. Kardjilov, R. Grothausmann, M. Dawson, C. Hartnig, S. Haas, D. Thomas, A. Hoell, C. Genzel, J. Banhart, Investigation of Energy-Relevant Materials with Synchrotron X-Rays and Neutrons, *Adv. Eng. Mater.*, 13 (2011) 712-729.
- [48] H. Markotter, I. Manke, R. Kuhn, T. Arlt, N. Kardjilov, M.P. Hentschel, A. Kupsch, A. Lange, C. Hartnig, J. Scholta, J. Banhart, Neutron tomographic investigations of water distributions in polymer electrolyte membrane fuel cell stacks, *Journal of Power Sources*, 219 (2012) 120-125.
- [49] F. Pfeiffer, T. Weitkamp, O. Bunk, C. David, Phase retrieval and differential phase-contrast imaging with low-brilliance x-ray sources, *Nature Physics*, 2 (2006) 258.
- [50] C. David, J. Bruder, T. Rohbeck, C. Grunzweig, C. Kottler, A. Diaz, O. Bunk, F. Pfeiffer, Fabrication of diffraction gratings for hard X-ray phase contrast imaging, *Microelectronic Engineering*, 84 (2007) 1172-1177.
- [51] S.W. Lee, K.Y. Kim, O.Y. Kwon, N. Kardjilov, M. Dawson, A. Hilger, I. Manke, Observation of Magnetic Domains in Insulation-Coated Electrical Steels by Neutron Dark-Field Imaging, *Applied Physics Express* 3(2010) 106602.
- [52] A. Hilger, N. Kardjilov, T. Kandemir, I. Manke, J. Banhart, D. Penumadu, A. Manescu, M. Strobl, Revealing microstructural inhomogeneities with dark-field neutron imaging, *Journal of Applied Physics*, 107 (2010) 036101.

- [53] M. Strobl, B. Betz, R.P. Harti, A. Hilger, N. Kardjilov, I. Manke, C. Gruenzweig, Wavelength-dispersive dark-field contrast: micrometre structure resolution in neutron imaging with gratings, *J Appl Crystallogr*, 49 (2016) 569-573.
- [54] E. Dabah, B. Pfretzschner, T. Schaupp, N. Kardjilov, I. Manke, M. Boin, R. Woracek, A. Griesche, Time-resolved Bragg-edge neutron radiography for observing martensitic phase transformation from austenitized super martensitic steel, *Journal of Materials Science*, (2016) 1-7.
- [55] R. Woracek, D. Penumadu, N. Kardjilov, A. Hilger, M. Strobl, R.C. Wimpory, I. Manke, J. Banhart, Neutron Bragg-edge-imaging for strain mapping under in situ tensile loading, *Journal of Applied Physics*, 109 (2011) 093506.
- [56] K. Iwase, H. Sato, S. Harjo, T. Kamiyama, T. Ito, S. Takata, K. Aizawa, Y. Kiyonagi, In situ lattice strain mapping during tensile loading using the neutron transmission and diffraction methods, *Journal of Applied Crystallography*, 45 (2012) 113-118.
- [57] K. Nielsen, K. Lefmann, Monte Carlo simulations of neutron-scattering instruments using McStas, *Physica B: Condensed Matter*, 283 (2000) 426-432.
- [58] M. Boin, Nxs: A program library for neutron cross section calculations, *Journal of Applied Crystallography*, 45 (2012) 603-607.
- [59] N. Kardjilov, A. Hilger, I. Manke, R. Woracek, J. Banhart, CONRAD-2: the new neutron imaging instrument at the Helmholtz-Zentrum Berlin, *J Appl Crystallogr*, 49 (2016) 195-202.
- [60] M. Strobl, M. Bulat, K. Habicht, The wavelength frame multiplication chopper system for the ESS test beamline at the BER II reactor - A concept study of a fundamental ESS instrument principle, *Nuclear Instruments and Methods in Physics Research, Section A: Accelerators, Spectrometers, Detectors and Associated Equipment*, 705 (2013) 74-84.
- [61] N. Kardjilov, S.W. Lee, E. Lehmann, I.C. Lim, C.M. Sim, P. Vontobel, Improving the image contrast and resolution in the phase-contrast neutron radiography, *Nuclear Instruments and Methods in Physics Research, Section A: Accelerators, Spectrometers, Detectors and Associated Equipment*, 542 (2005) 100-105.
- [62] E. Dabah, B. Pfretzschner, T. Schaupp, N. Kardjilov, I. Manke, M. Boin, R. Woracek, A. Griesche, Time-resolved Bragg-edge neutron radiography for observing martensitic phase transformation from austenitized super martensitic steel, *Journal of Materials Science*, 52 (2017) 3490-3496.
- [63] N. Kardjilov, M. Dawson, A. Hilger, I. Manke, M. Strobl, D. Penumadu, K.H. Kim, F. Garcia-Moreno, J. Banhart A highly adaptive detector system for high resolution neutron imaging,

Nuclear Instruments and Methods in Physics Research Section A: Accelerators, Spectrometers, Detectors and Associated Equipment, 651 (2011) 95-99.

[64] C.A. Schneider, W.S. Rasband, K.W. Eliceiri, NIH Image to ImageJ: 25 years of image analysis, *Nature Methods*, 9 (2012) 671-675.

[65] M. Strobl, M. Bulat, K. Habicht, The wavelength frame multiplication chopper system for the ESS test beamline at the BER II reactor—A concept study of a fundamental ESS instrument principle, *Nuclear Instruments and Methods in Physics Research Section A: Accelerators, Spectrometers, Detectors and Associated Equipment*, 705 (2013) 74-84.

[66] R. Woracek, T. Hofmann, M. Bulat, M. Sales, K. Habicht, K. Andersen, M. Strobl, The test beamline of the European Spallation Source- Instrumentation development and wavelength frame multiplication, *Nuclear Instruments and Methods in Physics Research, Section A: Accelerators, Spectrometers, Detectors and Associated Equipment*, 839 (2016) 102-116.

[67] H. Sato, Deriving Quantitative Crystallographic Information from the Wavelength-Resolved Neutron Transmission Analysis Performed in Imaging Mode, *J. Imaging Journal of Imaging*, 4 (2018) 7.

[68] R. Woracek, D. Penumadu, N. Kardjilov, A. Hilger, M. Strobl, R.C. Wimpory, I. Manke, J. Banhart, Neutron Bragg-edge-imaging for strain mapping under in situ tensile loading, *Journal of Applied Physics*, 109 (2011) 1-5.

[69] M. Strobl, R. Woracek, N. Kardjilov, A. Hilger, R. Wimpory, A. Tremsin, T. Wilpert, C. Schulz, I. Manke, D. Penumadu, Time-of-flight neutron imaging for spatially resolved strain investigations based on Bragg edge transmission at a reactor source, *Nuclear Instruments and Methods in Physics Research, Section A: Accelerators, Spectrometers, Detectors and Associated Equipment*, 680 (2012) 27-34.

[70] R. Woracek, T. Hofmann, M. Bulat, M. Sales, K. Habicht, K. Andersen, M. Strobl, The test beamline of the European Spallation Source – Instrumentation development and wavelength frame multiplication, *Nuclear Instruments and Methods in Physics Research Section A: Accelerators, Spectrometers, Detectors and Associated Equipment*, 839 (2016) 102-116.

[71] A.S. Tremsin, J.B. McPhate, J.V. Vallerga, O.H.W. Siegmund, W. Kockelmann, A. Paradowska, S.Y. Zhang, J. Kelleher, A. Steuer, W.B. Feller, High-Resolution Strain Mapping Through Time-of-Flight Neutron Transmission Diffraction, *Materials Science Forum*, 772 (2013) 9-13.

[72] O. Arnold, J.C. Bilheux, J.M. Borreguero, A. Buts, S.I. Campbell, L. Chapon, M. Doucet, N. Draper, R. Ferraz Leal, M.A. Gigg, V.E. Lynch, A. Markvardsen, D.J. Mikkelsen, R.L. Mikkelsen, R. Miller, K. Palmen, P. Parker, G. Passos, T.G. Perring, P.F. Peterson, S. Ren, M.A. Reuter, A.T. Savici, J.W. Taylor, R.J. Taylor, R. Tolchenov, W. Zhou, J. Zikovsky, Mantid—Data analysis and

visualization package for neutron scattering and μ SR experiments, Nuclear Instruments and Methods in Physics Research Section A: Accelerators, Spectrometers, Detectors and Associated Equipment, 764 (2014) 156-166.

[73] K.L. G. Zsigmond, S. Manoshin, H. N. Bordallo,, J.P. J. D. M. Champion, J. M. Carpenter, and F. Mezei,, A survey of simulations of complex neutronic systems by VITESS, Nuclear Instruments and Methods in Physics Research A 529, (2004) 218-222

[74] K. Lefmann, K. Nielsen, McStas, a general software package for neutron ray-tracing simulations, Neutron News, 10 (1999) 20-23.

[75] M. Boin, Developments towards the tomographic imaging of local crystallographic structures, PhD Thesis, Open University 2010.

[76] P. Willendrup, E. Farhi, E. Knudsen, U. Filges, K. Lefmann, Component manual for the neutron ray-tracing Package McStas, version 2.1, DTU, 2018.

[77] J.T. Yates Jr, Experimental Innovations in Surface Science a Guide to Practical Laboratory Methods and Instruments, (2015).

[78] F.J. Owens, C.P. Poole, The physics and chemistry of nanosolids, (2008).

[79] C.C. Yang, M.X. Xiao, W. Li, Q. Jiang, Size effects on Debye temperature, Einstein temperature, and volume thermal expansion coefficient of nanocrystals, SSC Solid State Communications, 139 (2006) 148-152.

[80] R.J.B. Balaguru, B.G. Jeyaprakash, Lattice Vibrations, Phonons, Specific Heat Capacity, Thermal Conductivity., NPTEL – Electrical & Electronics Engineering – Semiconductor Nanodevices, 2015.

[81] D.B. Sirdeshmukh, L. Sirdeshmukh, K.G. Subhadra, Micro- and macro-properties of solids : thermal, mechanical and dielectric properties ; with ... 153 tables, Springer, Berlin; Heidelberg, 2006.

[82] G.A. Alers, Use of Sound Velocity Measurements in Determining the Debye Temperature of Solids, Physical Acoustics, 3 (1965) 1-42.

[83] F.H. Herbstein, Methods of measuring Debye temperatures and comparison of results for some cubic crystals, Advances in Physics, 10 (1961) 313-355.

- [84] G. Ghosh, G.B. Olson, The isotropic shear modulus of multicomponent Fe-base solid solutions, *Acta Materialia*, 50 (2002) 2655-2675.
- [85] H. Terasaki, H. Yamagishi, Experimental Determination of Elastic Modulus during Martensitic Transformation of Low Transformation Temperature Steel, *Changes*, 51 (2011) 1566-1568.
- [86] J. Miettinen, S. Louhenkilpi, Calculation of thermophysical properties of carbon and low alloyed steels for modeling of solidification processes, 1994, pp. 909-916.
- [87] S. Vogel, A Rietveld-Approach for the Analysis of Neutron Time-of-Flight Transmission Data, *Mathematisch-Naturwissenschaftliche Fakultät, PhD Thesis, Uni Kiel, Kiel*, 2000, pp. 174.
- [88] J.R.Granada, Total scattering cross section of solids for cold and epithermal neutrons, (1984).
- [89] H. Schopper, Y.A. Alexandrov, W.I. Furman, A.V. Ignatyuk, M.V. Kazarnovsky, V.Y. Konovalov, N.V. Kornilov, L.B. Pikelner, V.I. Plyaskin, Y.P. Popov, H. Rauch, W. Waschowski, Y.S. Zamyatnin, L. Abagaian, *Low Energy Neutrons and Their Interaction with Nuclei and Matter: Low Energy Neutron Physics*, (2000).
- [90] B.T.M. Willis, C.J. Carlile, *Experimental Neutron Scattering*, (2017).
- [91] R.E. Dinnebier, S.J.L. Billinge, A. Le Bail, I. Madsen, L.M.D. Cranswick, J.K. Cockcroft, P. Norby, A.D. Zuev, A. Fitch, J. Rodriguez-Carvajal, C. Giacobozzo, R.B. Von Dreele, P. Scardi, N.C. Popa, R. Allmann, *Powder Diffraction Theory and Practice*, (2008).
- [92] K. Binder, Total Coherent Cross Sections for the Scattering of Neutrons from Crystals, *Physica Status Solidi (B)*, 41 (1970) 767-779.
- [93] C.G. Windsor, *Pulsed neutron scattering*, Taylor & Francis, London, 1981.
- [94] A. Steuwer, P.J. Withers, J.R. Santisteban, L. Edwards, Using pulsed neutron transmission for crystalline phase imaging and analysis, *Journal of Applied Physics*, 97 (2005) 074903.
- [95] N. Kardjilov, A. Hilger, I. Manke, CONRAD-2: Cold Neutron Tomography and Radiography at BER II (V7), *Journal of large-scale research facilities*, 2 (2016) A98.
- [96] N. Kardjilov, A. Hilger, I. Manke, M. Strobl, M. Dawson, S. Williams, J. Banhart, Neutron tomography instrument CONRAD at HZB, *Nuclear Instruments and Methods in Physics Research Section A: Accelerators, Spectrometers, Detectors and Associated Equipment*, 651 (2011) 47-52.
- [97] M.G. Makowska, L. Theil Kuhn, L.N. Cleemann, E.M. Lauridsen, H.Z. Bilheux, J.J. Molaison, L.J. Santodonato, A.S. Tremsin, M. Grosse, M. Morgano, S. Kabra, M. Strobl, *Flexible*

sample environment for high resolution neutron imaging at high temperatures in controlled atmosphere, *Review of Scientific Instruments* *Review of Scientific Instruments*, 86 (2015) 125109.

[98] M.D. Abràmoff, P.J. Magalhães, S.J. Ram, Image processing with imageJ, *Biophotonics International*, 11 (2004) 36-41.

[99] F. Christiena, M.T.F. Telling, K.S. Knightb, A comparison of dilatometry and in-situ neutron diffraction in tracking bulk phase transformations in a martensitic stainless steel, *Materials characterization*, 82 (2013) 50-57.

[100] H.H. Mantsch, D.J. Moffatt, H.L. Casal, Fourier transform methods for spectral resolution enhancement, *Journal of Molecular Structure* *Journal of Molecular Structure*, 173 (1988) 285-298.

[101] J.K. Kauppinen, D.J. Moffatt, H.H. Mantsch, D.G. Cameron, Fourier Self-Deconvolution: A Method for Resolving Intrinsically Overlapped Bands, *Applied Spectroscopy*, 35 (1981) 271-276.

[102] P.R. Griffiths, G.L. Pariente, Introduction to spectral deconvolution, *TRAC* Trends in Analytical Chemistry, 5 (1986) 209-215.

[103] J.K. Kauppinen, D.J. Moffatt, H.H. Mantsch, D.G. Cameron, Fourier transforms in the computation of self-deconvoluted and first-order derivative spectra of overlapped band contours, *Anal. Chem. Analytical Chemistry*, 53 (1981) 1454-1457.

[104] National Institute of Standards and Technology, Neutron activation and scattering calculator, 2018.

[105] N. Hachouf, F. Kharfi, A. Boucenna, Characterization and MCNP simulation of neutron energy spectrum shift after transmission through strong absorbing materials and its impact on tomography reconstructed image, *Applied Radiation and Isotopes*, 70 (2012) 2355-2361.

[106] N. Hachouf, F. Kharfi, M. Hachouf, A. Boucenna, New analytical approach for neutron beam-hardening correction, *Applied Radiation and Isotopes*, 107 (2016) 353-358.

[107] A. Lange, M.P. Hentschel, A. Kupsch, B.R. Mueller, Numerical correction of X-ray detector backlighting, *International Journal of Materials Research*, 103 (2012) 174-178.

[108] T. Arlt, M. Klages, M. Messerschmidt, J. Scholta, I. Manke, Influence of artificially aged gas diffusion layers on the water management of polymer electrolyte membrane fuel cells analyzed with in-operando synchrotron imaging, *Energy*, 118 (2017) 502-511.

- [109] C. Hartnig, I. Manke, J. Schloesser, P. Krüger, R. Kuhn, H. Riesemeier, K. Wippermann, J. Banhart, High resolution synchrotron X-ray investigation of carbon dioxide evolution in operating direct methanol fuel cells, *Electrochemistry Communications*, 11 (2009) 1559-1562.
- [110] J. Hinebaugh, J. Lee, A. Bazylak, Visualizing Liquid Water Evolution in a PEM Fuel Cell Using Synchrotron X-ray Radiography, *Journal of The Electrochemical Society*, 159 (2012) F826-F830.
- [111] T. Arlt, W. Maier, C. Totzke, C. Wannek, H. Markotter, F. Wieder, J. Banhart, W. Lehnert, I. Manke, Synchrotron X-ray radioscopic in situ study of high-temperature polymer electrolyte fuel cells - Effect of operation conditions on structure of membrane, *Journal of Power Sources*, 246 (2014) 290-298.
- [112] D. Schroeder, C.L. Bender, M. Osenberg, A. Hilger, I. Manke, J. Janek, Visualizing Current-Dependent Morphology and Distribution of Discharge Products in Sodium-Oxygen Battery Cathodes, *Scientific Reports*, 6 (2016).
- [113] F. Sun, H. Markoetter, K. Dong, I. Manke, A. Hilger, N. Kardjilov, J. Banhart, Investigation of failure mechanisms in silicon based half cells during the first cycle by micro X-ray tomography and radiography, *Journal of Power Sources*, 321 (2016) 174-184.
- [114] F. Sun, H. Markoetter, I. Manke, A. Hilger, N. Kardjilov, J. Banhart, Three-Dimensional Visualization of Gas Evolution and Channel Formation inside a Lithium-Ion Battery, *Acs Applied Materials & Interfaces*, 8 (2016) 7156-7164.
- [115] M. Ebner, F. Marone, M. Stampanoni, V. Wood, Visualization and Quantification of Electrochemical and Mechanical Degradation in Li Ion Batteries, *Science*, 342 (2013) 716-720.
- [116] F. Sun, L. Zielke, H. Markoetter, A. Hilger, D. Zhou, R. Moroni, R. Zengerle, S. Thiele, J. Banhart, I. Manke, Morphological Evolution of Electrochemically Plated/Stripped Lithium Microstructures Investigated by Synchrotron X-ray Phase Contrast Tomography, *Acs Nano*, 10 (2016) 7990-7997.
- [117] F. Sun, R. Moroni, K. Dong, H. Markeotter, D. Zhou, A. Hilger, L. Zielke, R. Zengerle, S. Thiele, J. Banhart, I. Manke, Study of the Mechanisms of Internal Short Circuit in a Li/Li Cell by Synchrotron X-ray Phase Contrast Tomography, *Acs Energy Letters*, 2 (2017) 94-104.
- [118] M. Ebner, F. Geldmacher, F. Marone, M. Stampanoni, V. Wood, X-Ray Tomography of Porous, Transition Metal Oxide Based Lithium Ion Battery Electrodes, *Advanced Energy Materials*, 3 (2013) 845-850.

- [119] M. Salzer, A. Spetl, O. Stenzel, J.H. Smatt, M. Linden, I. Manke, V. Schmidt, A two-stage approach to the segmentation of FIB-SEM images of highly porous materials, *Materials Characterization*, 69 (2012) 115-126.
- [120] S. Zils, M. Timpel, T. Arlt, A. Wolz, I. Manke, C. Roth, 3D Visualisation of PEMFC Electrode Structures Using FIB Nanotomography, *Fuel Cells*, 10 (2010) 966-972.
- [121] L. Holzer, F. Indutnyi, P.H. Gasser, B. Munch, M. Wegmann, Three-dimensional analysis of porous BaTiO₃ ceramics using FIB nanotomography, *Journal of Microscopy-Oxford*, 216 (2004) 84-95.
- [122] B.J. Inkson, M. Mulvihill, G. Mobus, 3D determination of grain shape in a FeAl-based nanocomposite by 3D FIB tomography, *Scripta Materialia*, 45 (2001) 753-758.
- [123] A. Kupsch, M.P. Hentschel, A. Lange, B.R. Mueller, How to correct X-ray detector backlighting, *Materials Testing*, 55 (2013) 577-581.
- [124] A. Lange, A. Kupsch, M. Hentschel, B. Müller, Straightforward Correction of X-Ray Detector Backlighting, 18th World Conference on Nondestructive Testing, Durban, South Africa, 2012.
- [125] A. Lange, M.P. Hentschel, A. Kupsch, B.R. Muller, Numerical correction of X-ray detector backlighting, *INTERNATIONAL JOURNAL OF MATERIALS RESEARCH*, 103 (2012) 174-178.
- [126] B.R. Müller, A. Lange, M.P. Hentschel, A. Kupsch, A comfortable procedure for correcting X-ray detector backlight, *Journal of Physics: Conference Series*, 425 (2013).

Acknowledgements

I would like to acknowledge all the people who have contributed to my dissertation

- Prof. Dr John Banhart, for giving me an opportunity to pursue my PhD at the Technische Universität Berlin and Helmholtz-Zentrum Berlin.
- Dr.Ingo Manke, for providing me a supports, guidance on how to work scientifically and his effort through the process of researching and writing this thesis.
- Dr Nikolay Kardjilov, Dr Robin Woracek, Dr Henning Markötter, Dr André Hilger and Dr Tobias Arlt for helping me in experiments and discussions during my PhD period.
- Dr Andreas Kupsch, Prof. Manfred Hentschel and Axel Lange (Bundesanstalt für Materialforschung und -prüfung (BAM)) for their valuable ideas.
- All colleagues and friends how helped during my PhD period.
- Mutah University for offering me financial support.

Finally, I must express my gratitude to my parents, my wife (Jenan), my daughters (Joury and Hala), my brothers and sisters for providing me endless love and continuous encouragement throughout my years of study.